Silicon Carbide Material Properties Selection for Mechanical Seal Faces

Undergraduate Honors Thesis for Will Hoskins

Will Hoskins, Jose March-Rico, James Brackett, Nick Combs, and Josh Tharpe

Advisors: Dr. Veerle Keppens, Dr. Claudia Rawn, and John Salasin (GTA)

Corporate Advisors: Chris Rehmann and Rutvij Borte, AESSEAL Inc.

MSE 489 – Capstone Senior Design

University of Tennessee, Knoxville – Materials Science and Engineering

Submitted on: 5 May 2017

TABLE OF CONTENTS

1 ABSTRACT

AESSEAL Inc. was interested in gauging and comparing the characteristics of sintered, reaction-bonded, and graphite-loaded SiC as mechanical seal face materials. Mechanical seals prevent leakage of fluids in pumps, agitators, and other applications where a rotating shaft passes from a fluid environment to the atmosphere. Durable seal face materials must exhibit suitable thermal, mechanical, and chemical properties to minimize frictional heat generation, wear, and corrosion. AESSEAL set forth the objectives of quantifying the properties and supplier quality for each type of SiC material to assess their individual strengths and weaknesses for mechanical seal applications. AESSEAL provided nine sets of SiC mechanical seals: two sintered SiC (SSiC), two reaction-bonded SiC (RBSiC), and five graphite-loaded SiC (GLSiC). A full assessment of the seal sets is provided with the identification of secondary phases, a quantification of the volume fraction of each phase, and an analysis of the impact of secondary phases on the seals' properties and performance. Graphite and free silicon secondary phases were identified by density (Archimedes method), X-ray diffraction, and ceramographic investigation. The volume fraction of identified phases was determined by ImageJ automated image analysis software; in particular, the size and distribution of graphite nodules in the GLSiC samples were examined to compare supplier quality. An investigation into the material properties was conducted through microhardness measurements, resonant ultrasound spectroscopy (RUS), and compression testing to quantify the impact of secondary phases. This report aims to provide a detailed explanation of the theory and background necessary to understand the implications of acquired results.

2 BACKGROUND

Widespread use of mechanical seals in pumps, agitators, and mixers has come to fruition in the past few decades as their performance has surpassed that of traditional packing. Mechanical seals are employed in applications where a rotating shaft passes from one environment into another. The primary responsibility of the seal is to prevent the service liquid from escaping to the environment. The intricacy of this seemingly simple task escalates when the service liquid has abrasive particles, corrosive chemicals, or is at extreme temperatures. The mechanical seal must be highly reliable and efficient, operating with minimal lubricant and frictional resistance. Materials Selection and materials processing decision are crucial when choosing and designing the optimum seal. To make informed decisions, it is imperative to understand the manufacturing and processing of silicon carbide (SiC) and how these procedures affect the resulting microstructure. Therefore, an exhaustive explanation of the manufacturing and processing procedure for sintered, reaction-bonded, and graphite-loaded SiC is provided. An explanation of lubrication mechanisms in mechanical seals is also described and linked to the factors that affect tribological performance; in particular, characteristics of controlled surface features in seal face materials are detailed to postulate the tribological role of graphite particles in SiC.

2.1 AESSEAL INC.

Established in 1979, AESSEAL Inc. specializes in the design, manufacturing, and refurbishment of mechanical seals. Available products include mechanical seals (such as component, compressor, and cartridge seals), seal support systems, bearing protection, and traditional gland packing. AESSEAL Inc. provides mechanical seals for the oil and gas, power generation, chemical, bio/ethanol, mining and minerals, building services, sugar refining, pulp and paper, food and beverage, water and waste water, automotive, metal processing, corn milling, and marine industries [1]. This senior design project was conducted in cooperation with the Rockford, TN AESSEAL facility. The Rockford facility is responsible for the assembly, refurbishment, and supply of mechanical seals; the end-product mechanical seal faces are not manufactured on-site. Facility capabilities include lapping, seal face flatness evaluation by monochromatic helium light band readings, and Computer Numerical Controlled (CNC) machining for custom component fabrication. The AESSEAL Rockford facility has generously offered support and guidance of this senior design project and provided samples for analysis.

2.2 MECHANICAL SEALS

In pumps, mixers, agitators, and reactors, a shaft passes through two environments that cannot mix. Whether it be a shaft exiting a lubricant-filled pump housing, an agitator shaft passing into a drilling mud tank, or an impeller shaft travelling between an electric motor and the impeller, it is critical that the passageway be sealed. An example of a centrifugal pump is shown in Figure 1 [2]. A fundamental question that is often overlooked, or considered with a subpar thoroughness is what does the engineer choose for preventing the process fluid from escaping the pump housing? When a pump or other machine requiring a seal around a rotating shaft is designed or selected, the following list of pump and service environment characteristics should be considered for the given application:

1. Pressure at the seal
2. Temperature at the seal
3. Fluid being sealed (corrosion potential, viscosity, specific heat, presence of solids or contaminants, etc.)
4. Speed of shaft rotation
5. Rotation displacements (axial and radial)
6. Allowable leakage rate
7. Required reliability/service time
8. Environmental regulations regarding the release of the process fluid
9. Allowable friction
10. Required energy efficiency
11. Cost

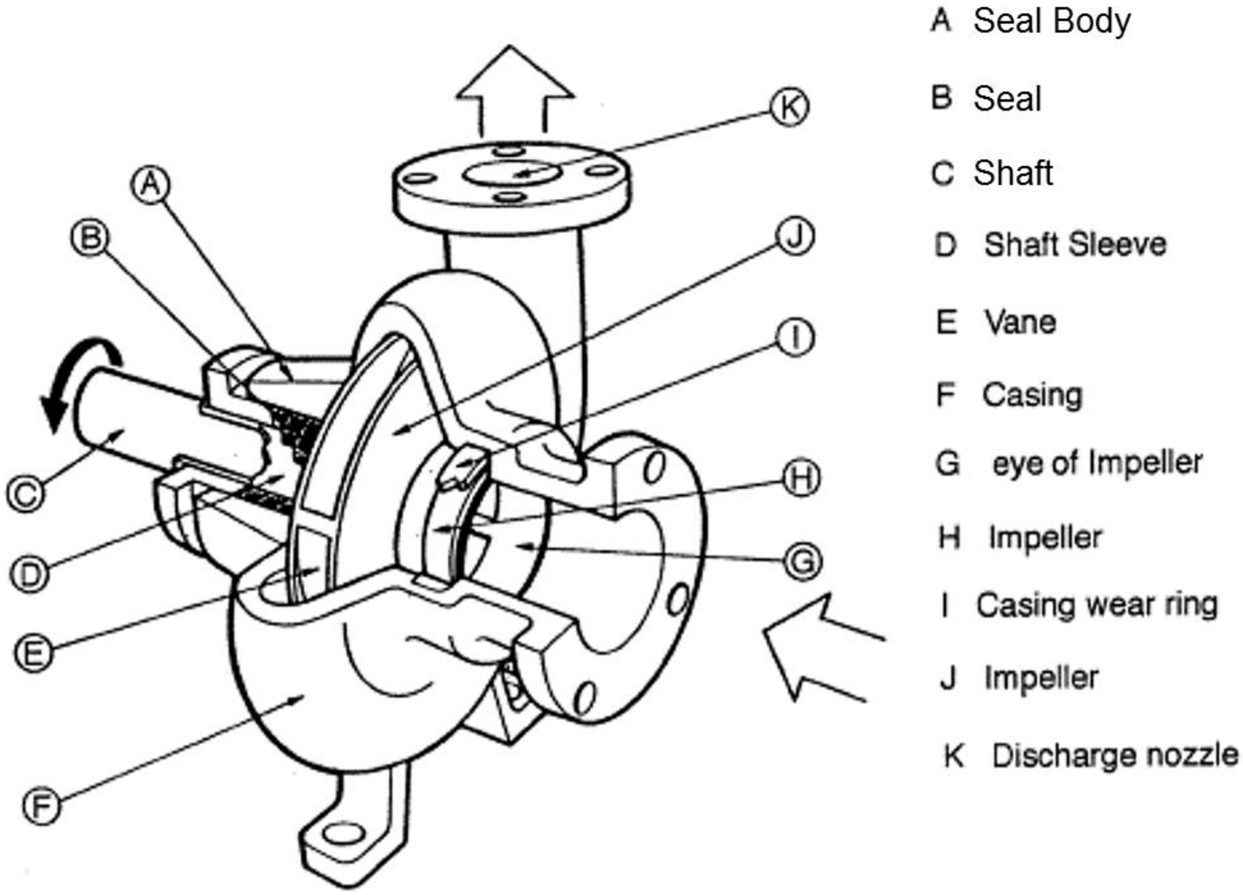

Figure 1: Schematic of a centrifugal pump illustrating that it is necessary to have a seal at the location where the impeller passes through the seal casing [2].

When trying to determine the optimum sealing option, it is crucial to consider all of the previously listed factors. This is especially important taken in the context that pumps are the second most common machine in industry, with an estimated 600 million industrial pumps in operation around the world [3]. Further, sealing options should receive utmost consideration since the majority of premature failures in industrial pumps are associated with shaft sealing [4].

2.2.1 Shaft Sealing Options

Historically, the dominant means of sealing a shaft was with the use of packing inside a stuffing box around the shaft. A packed box shaft seal consists of numerous rings of soft, compressible packing in a cylindrical recess (generally known as a "stuffing box") around the shaft sleeve [5]. An example of this is the packing of wagon wheels. Grease in the hubs of these wheels was contained with a piece of rope that was tightly packed inside the wheel hub. Contemporary packed stuffing boxes still see widespread use in industrial settings, with the packing being compressed by an adjustable gland that produces a close radial clearing with the shaft to minimize leakage. Gland packing materials are primarily polymeric (such as polytetrafluoroethylene (PTFE)). However, stuffing boxes suffer from several limitations stemming from leakage, friction, and degradation in harsh environments.

For extreme industrial applications in which high pressures, fast rotational speeds, high temperatures, and corrosive environments are encountered, mechanical seals are an important choice. Mechanical seals have been used with increasing popularity for the last 40 years [4]. Mechanical seals are more expensive, but this increased expense is offset by greater sealing capability, lower leakage, increased environmental tolerance, and self-compensation for wear [6]. The possibility of improved utilization in extreme environments at a higher cost has placed a great technological importance on mechanical seals. Thus, significant research has been conducted to improve their performance and longevity as the limiting design factor for applications in which a seal around a rotating shaft is required.

2.2.2 Design of Mechanical Seals

The superiority of mechanical seals is derived from the orientation of their sealing elements. When sealing by packing, the seals act on the circumference of the shaft. Intimate contact with the shaft results in friction between the shaft and sealing material, mandating that the seal compensate with the radial motion of the shaft. Therefore, these seals must be designed to accommodate both shaft dimensions and radial position. However, with mechanical seals, the sealing force acts along the shaft axial direction. The sealing face is normal to the axial direction and has a higher tolerance for axial motion of the shaft and does not have to conform precisely to the shaft dimensions [6].

A mechanical seal is composed of two faces: a stationary face and a rotating face. The stationary face is fixed to the housing and sealed with an O-ring to prevent fluid from escaping between the housing and mechanical seal. Similarly, the rotating face is attached to the shaft and sealed by an O-ring to form rotating contact between the seal faces. The seal faces are polished to a fine finish and have a high degree of flatness to ensure intimate contact around the entire circumference of the seal. This minimizes friction and seal damage and maximizes the effect of the thin, lubricating film that forms between the seal faces. The seal assembly is attached to the pump housing by the gland. An example of a single, parallel-spring seal is shown in Figure 2. Mechanical seals can be divided into two classes based on seal arrangement: single seal installations and multiple seal installations [7].

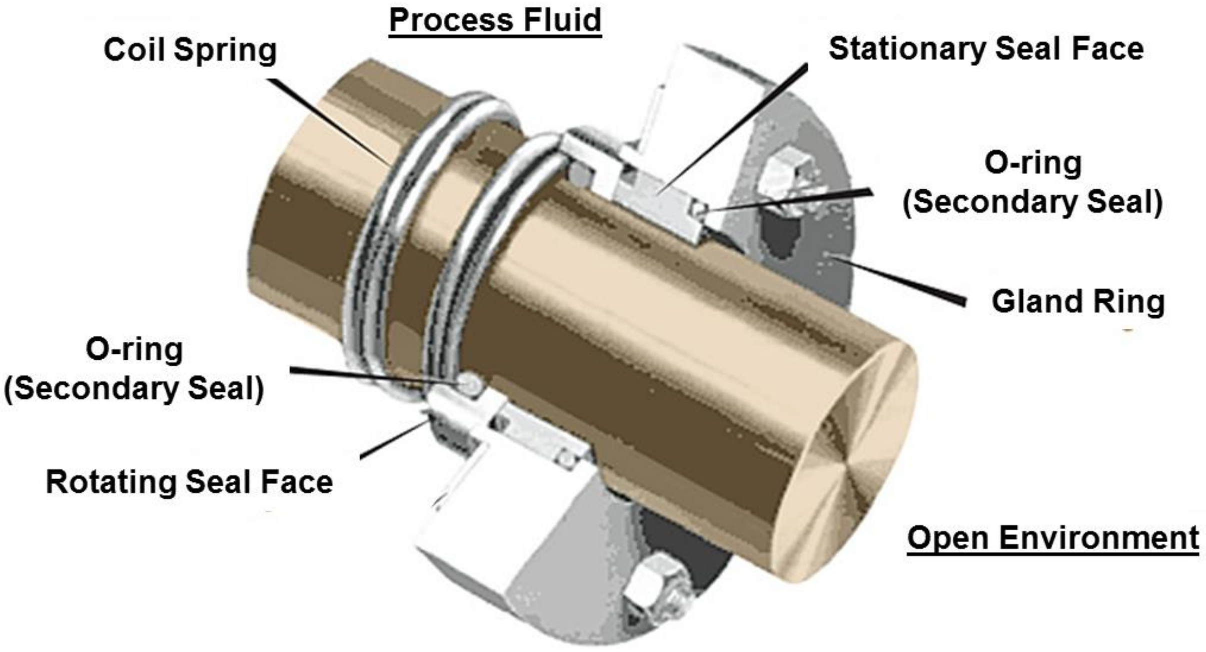

Figure 2: Example configuration of a simple parallel spring mechanical seal [8]. The gland ring attaches the stationary seal components to the pump casing.

As the simplest seal arrangement with the least number of parts, single seals are the most widely employed. In the case of a parallel spring seal, the spring provides the force between the two faces that seal the process fluid from the environment. While not all single seals follow this design, it is common to incorporate a spring to provide the sealing force between seal faces. Normally a single seal arrangement is cooled and lubricated by the liquid being sealed. This mechanism of lubrication results in a slow loss of process fluid when the seal performs properly (~1-10 gallons/year). Single seals are effective in low pressure environments where the process fluid is “clean” (free of abrasives capable of damaging seal faces) and has low viscosity to allow flow between the seal faces. An example of a suitable lubricating fluid for single seals is clean water; conversely, crude oil, sewage, acids, and viscous liquid polymers are examples of unsuitable lubricating fluids.

In harsher applications where the process fluid is not a good lubricating fluid, multiple seals are often used. Of the multiple seals class, double seals are the most common. The double seal configuration consists of two seals back-to-back, as illustrated in Figure 3. These seals form an isolated environment known as a buffer zone. A buffer fluid (a neutral liquid such as water) is pressurized in the buffer zone to a pressure higher than the process fluid. This configuration results in a slow net leak of neutral fluid to the process environment, but in return offers a neutral, effective lubricant, improved corrosion resistance, and a buffered area for plant safety. While the secondary system responsible for providing and recycling the neutral fluid is costly, the improved seal lifetime and safety often mitigates this cost.

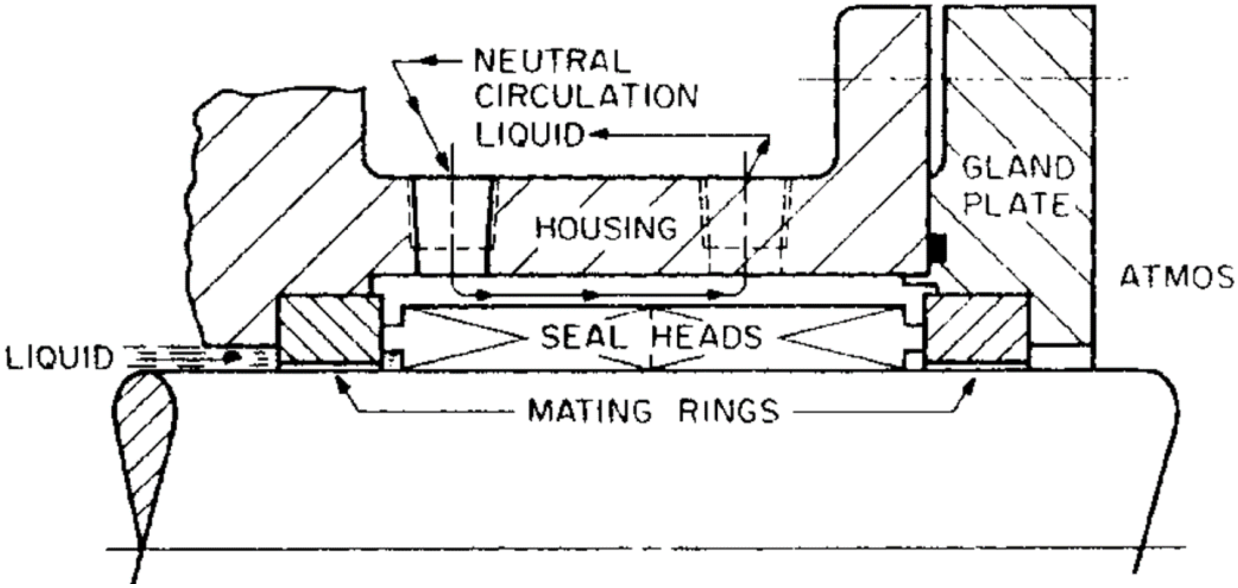

Figure 3: Schematic of a double seal configuration where a neutral liquid is circulated through the buffer zone [7].

As previously mentioned, mechanical seal failure is the most prevalent mode of pump failure. Wearing of the seal face occurs over a long period of normal operation. Extensive wear may eventually lead to seal failure due to seals normally wearing in an uneven manner. This uneven wear results from the stress state of the seal or the presence of debris or abrasive contaminants. Eventually, the flatness and coherent seal face contact width around the seal circumference is not sufficient to prevent leaking. Another type of failure results from brittle fracture initiated by a defect in the seal or by stresses on the seal. However, the most common form of failure is from dry-running the seal. Mechanical seals are engineered to operate with a thin fluid film between the seal faces. If this thin fluid film is disrupted, the seal faces make contact with each other, produce extensive heat, and fail over a matter of seconds, as illustrated in Figure 4. Typically, this occurs when the process stream is cut off from the pump for which it acts as the lubricating liquid. Often failure by dry running may be avoided by implementing a secondary buffer liquid system to act as primary lubrication for seal faces.

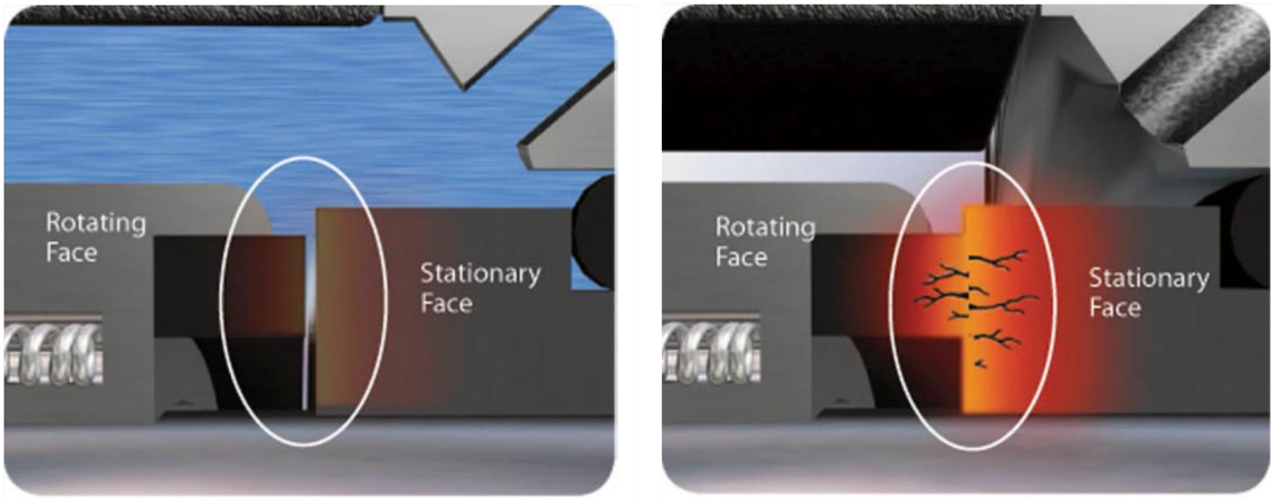

Figure 4: Left: Illustration of properly lubricated mechanical seal faces; Right: Dry-running of mechanical seal faces results in overheating and failure [3].

2.2.3 Materials Selection and Mechanical Design

The design for mechanical seals imposes strict property limitations for the selection of seal face materials. The material must exhibit excellent hardness to prolong component lifetime and increase the reliability of equipment. Harder materials wear more slowly and do not wear unevenly in the presence of abrasive particles in the fluid. However, harder materials often cause greater frictional heat at the seal interface. Thus, it is imperative that a durable seal face material possesses a suitable thermal conductivity to avoid insulation of frictional heat and minimize thermal gradients across the seal face. High fracture toughness is necessary to avoid brittle fracture in the presence of defects or unintentional forces, such as improper user handling. Possibly the greatest consideration for seal face lifetime, however, is chemical compatibility with the contact fluid. The selected seal face material must resist corrosion to prevent premature wear and failure. This is particularly true for mechanical seals that consist of multiple phases (e.g. cobalt-bound tungsten carbide (WC) or reaction-bonded SiC) where one phase might be individually susceptible to a range of fluids.

Initially, seal face materials consisted of metals such as hardened steels, copper, and bronze [9]; materials science advancements have since offered superior seal face material alternatives. Modern seal face materials include mechanical carbon grades (such as resin-impregnated and antimony-impregnated carbon), alumina (Al_2O_3), WC (commonly cobalt-bound or nickel-bound WC), and SiC (either sintered or reaction-bonded). Figures 5-7 were generated using Granta Design’s CES Materials Selector software to compare the desired material properties of these common seal face materials [10]. These graphs show that SiC offers superior hardness and thermal conductivity.

Furthermore, SiC is chemically resistant to most fluids and is not as susceptible to thermal shock as Al_2O_3. While WC does offer excellent fracture toughness, SiC exhibits good toughness and strength while offering a relatively low cost. These properties are the predominant factors for SiC's widespread use in the mechanical seal industry as a hard face material.

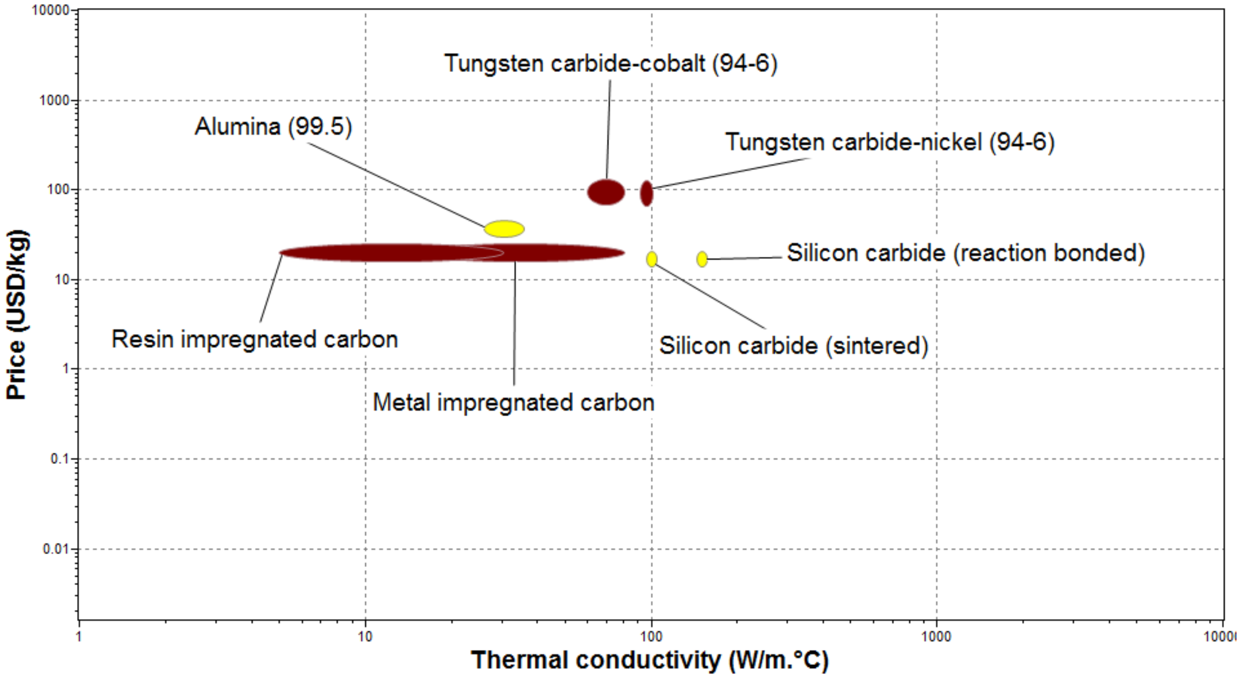

Figure 5: Thermal conductivity vs price for common seal face materials [10].

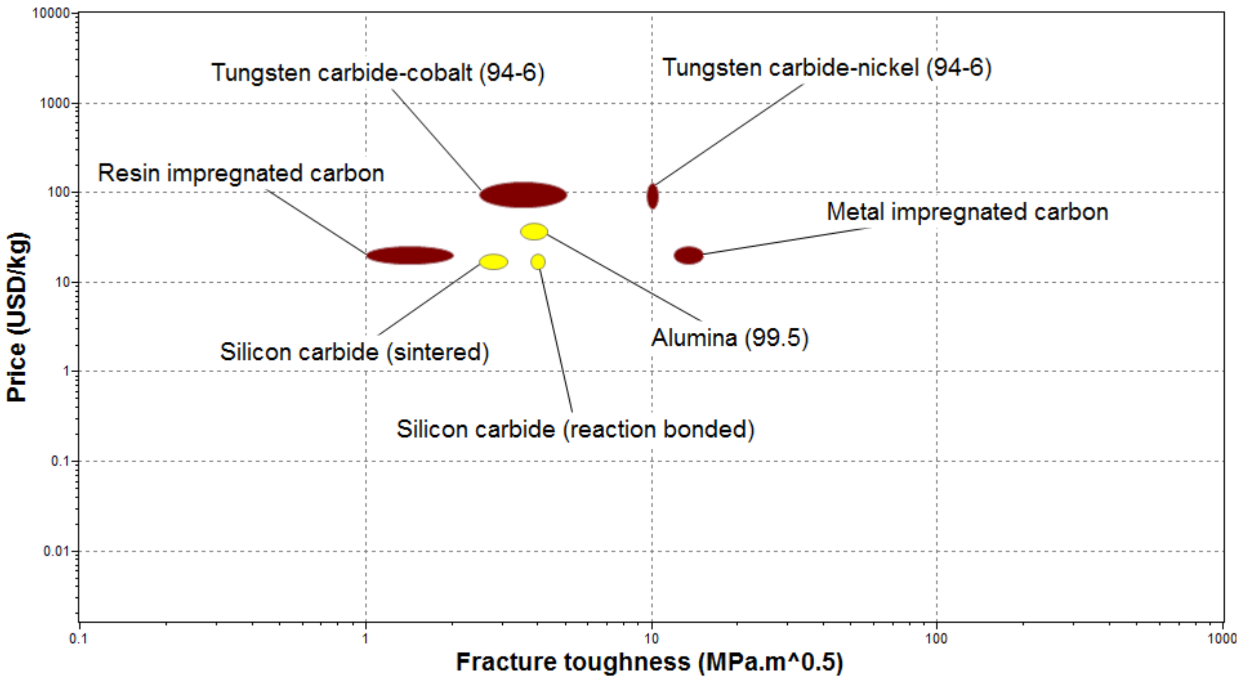

Figure 6: Fracture toughness vs price for common seal face materials [10].

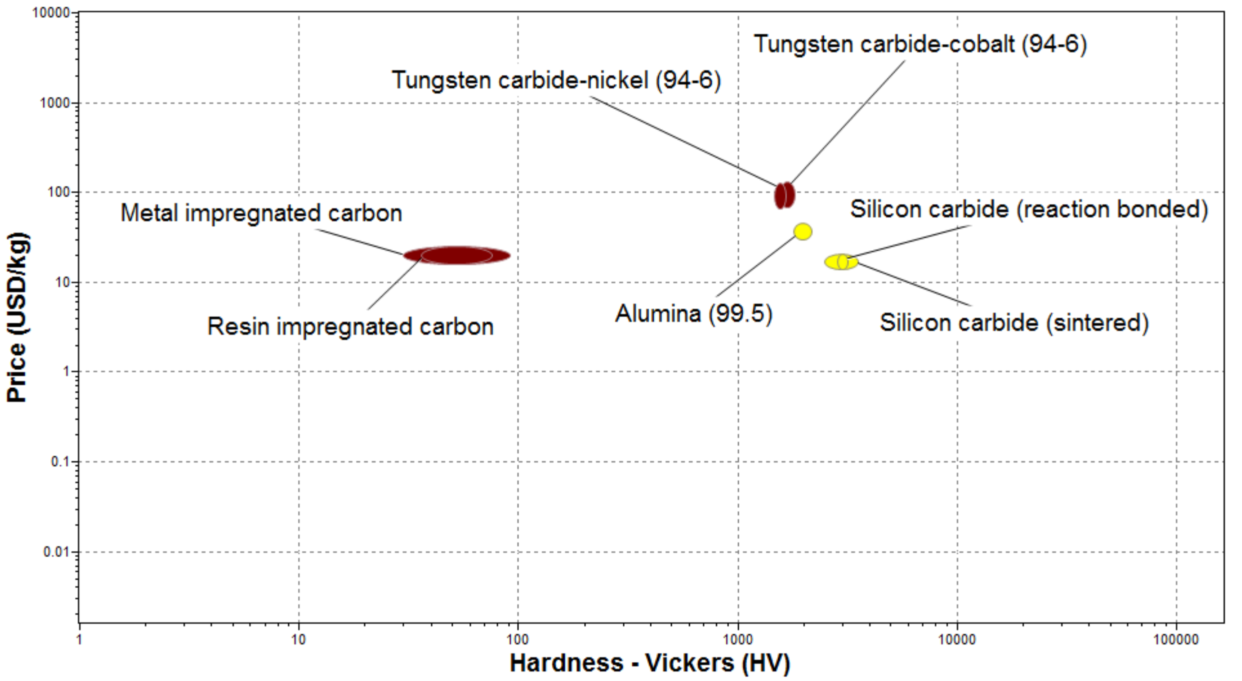

Figure 7: Hardness vs price for common seal face materials [10].

2.3 SILICON CARBIDE

SiC is among the hardest known materials, making it an excellent candidate for applications where abrasion resistance is desired. The Si-C phase diagram is shown in Figure 8 and shows SiC as an invariant compound with a fixed composition, but the compound does exist in many forms, or polytypes. There are over 200 known hexagonal and rhombohedral polytypes of SiC collectively referred to as α-SiC. These types are distinct from one another by the unique stacking sequence of Si and C layers.

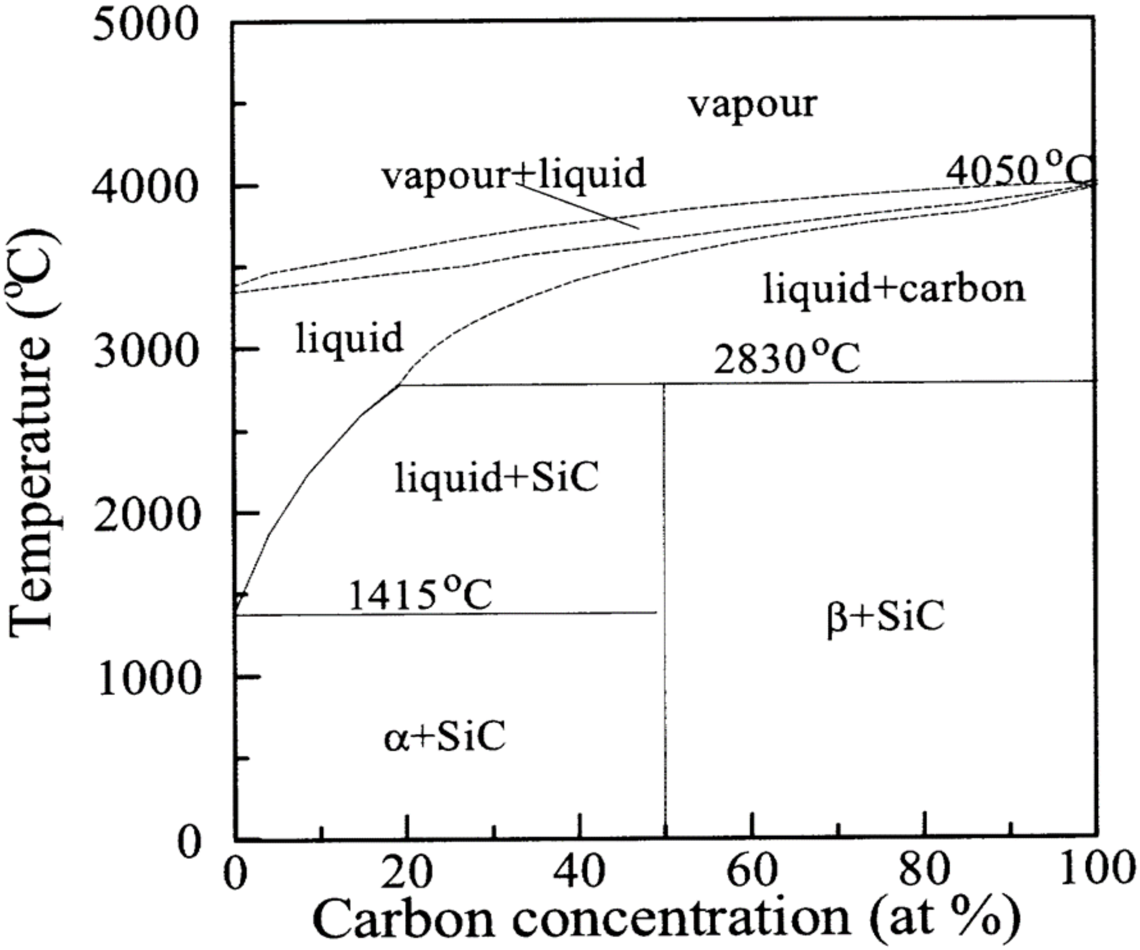

Figure 8: Silicon-carbide phase diagram [16]. SiC exists as an invariant composition at 50 at% Si-50 at% C.

The cubic polytype of SiC is referred to as β-SiC and possesses the zinc blende structure. Both α- and β-SiC grains may be present in a polycrystalline sample, depending on how it was fabricated. There are two main processes by which SiC components for applications are fabricated: sintering and reaction-bonding. Both processes begin with high purity SiC powder manufactured by the Acheson process. The manufacturing of high purity SiC powder begins with the combination of silica (SiO_2) sand with C (usually coke) in a graphite furnace. The mixture is heated to temperatures between 1600 and 2500 °C, resulting in a porous block of SiC that is subsequently ground into a uniform powder. The purity of this SiC powder is generally in excess of 98% [11].

Sintering of SiC requires the use of sintering aids, as minimal sintering is observed in compacts of pure SiC powder [11]. Pressureless solid-state sintering can be achieved at high temperatures around 2100 ^{o}C with the addition of B and C. Liquid-phase sintering can be achieved at lower temperatures (1800-2000 ^{o}C) with the aid of metal oxides such as Al_2O_3 and Y_2O_3 [12]. Liquid-phase sintered SiC tends to have higher strength and fracture toughness than solid-state sintered SiC [12]. Reaction-bonded SiC (RBSiC) is produced by infiltrating a compact of SiC and carbon with liquid Si. SiC powder, graphite, and a polymeric binder are first compacted together before being heated in air to remove the binder, resulting a porous structure. The compact is subsequently infiltrated with liquid Si, which travels through the pores via capillary action. The liquid Si reacts with the free carbon in the compact to form new SiC [13]. The newly formed SiC will both grow epitaxially on the existing SiC grains as well as nucleate and form new grains. Free Si will exist in the residual pore space not filled by new SiC; the free Si phase offers increased thermal conductivity and fracture toughness with the consequence of lowered chemical resistance. Any fluids that attack silicon will effectively corrode reaction-bonded SiC.

Recently, a new form of SiC composite known as Graphite-Loaded SiC (GLSiC) has received attention for mechanical seal applications. This composite contains free graphite within a SiC matrix, which helps to improve the lubricity of the seal face. The matrix is typically formed from sintered SiC [14]. The presence of the free graphite reduces the mechanical strength of the composite but improves the tribological behavior [14].

2.3.1 Manufacturing of Silicon Carbide Powder

Each of the manufacturing techniques for structural SiC begins with SiC in the powder form. This powder is formed into a dense green compact then undergoes a high temperature process to form the final SiC component, typically using the methods discussed in *Sections 2.3.2* and *2.3.3*. It has been shown that both the starting SiC particle size, distribution, and phase are important factors in the resulting mechanical properties of the structural SiC component [12].

The most widespread process for the production of SiC powder is the Acheson Process. This process has its origins in the late 19th century when Edward Acheson fabricated bulk SiC by reacting silica (SiO_2) with carbon at high temperatures [15]. A century later, almost all world-wide large-scale SiC synthesis efforts follow the original concept developed by Acheson. Modern Acheson furnaces are as long as 15 m and reach temperatures in excess of 1500 °C (sometimes as high as 2500 °C), and as much as 150 tons of SiO_2 and 100 tons of carbon are added to a furnace to produce over 100 tons of SiC per batch [15]. Most commonly, petroleum coke (the final residue from crude oil) is used as the carbon source. The formation of SiC proceeds primarily via the following set of sequential reactions (Equations 1-4):

$$C\ (s) + SiO_2\ (s) \rightarrow SiO\ (g) + CO(g) \tag{1}$$

$$SiO_2\ (s) + CO(g) \rightarrow SiO\ (s) + CO_2\ (g) \tag{2}$$

$$C(s) + CO_2\ (g) \rightarrow 2CO(g) \tag{3}$$

$$2C\ (s) + SiO\ (s) \rightarrow SiC\ (s) + CO\ (g) \tag{4}$$

The SiC produced using this method is subsequently separated by a variety of processes depending upon quality. Large chunks of SiC removed from the furnace are not homogenous; these chunks undergo a series of manual separation stages. The result of the separation of large chunks is a mixture containing 90 to 92% SiC [16]. Further separation occurs leading to high quality SiC with >97% SiC. The most common impurities are unreacted silicon, unreacted carbon, and iron (most common impurity in SiO_2). After the crushing, screening, and magnetic separation, the final product is obtained. This process can be tuned to produce either α-SiC or β-SiC depending on reaction temperature. At temperatures between 1500 and 1800 ^oC, primarily β-SiC is produced, while at temperatures between 2100 and 2500 ^oC primarily produces α-SiC is [11]. Fabrication of parts from metastable β-SiC results in the formation of coarse, elongated grains during final structural component formation at temperatures in excess of 1950 ^oC [12]. However, the production of β-SiC by the Acheson process is less efficient than the production of α-SiC. Final powder sizes are as small as 1-2 μm in diameter and generally there is not a high degree of uniformity in terms of particle size.

The majority of SiC for structural applications is produced by the Acheson process, however, a number of other processes are employed for the production of niche grades of SiC powder. Using these other manufacturing methods, it is possible to produce SiC powder with a high degree of uniformity down to sizes as small as 0.2 μm in diameter [17]. The source of SiC powder for the components received from AESSEAL is unknown, however, our microstructural investigation indicates that the starting materials were likely synthesized by the Acheson process.

2.3.2 Sintered Silicon Carbide

Traditionally, the majority of structural SiC components have been manufactured from green compacts that are subsequently fired at high temperatures in an inert atmosphere to allow sintering. However, the sintering of SiC has faced three main obstacles:

1. The strong, highly covalent bonds of SiC impede the formation and movement of point/planar defects crucial to sintering.
2. The formation of SiO_2 is thermodynamically favorable and occurs swiftly in conditions with a significant oxygen partial pressure.
3. The temperature required to sinter SiC without sintering aids is high (>2300 ^{o}C).

These obstacles must be combated through the development of sintering aids that lower the sintering temperature, modify the SiC particle surface characteristics (removal of SiO_2 layer), and allow for densities approaching theoretical density.

Pressureless sintering is the most routine sintering procedure employed for the fabrication of sintered mechanical seals. In pressureless sintering, SiC powder is formed into a green compact with help from a forming aid (generally an organic binder) by either isostatic pressing, slip casting, extrusion, or injection molding. Additionally, the incorporation of a sintering aid prior to forming the green compact is critical to the densification of pressureless sintered parts. The most effective and widely implemented sintering aids are carbon, boron, and oxides such as alumina (Al_2O_3), yttria (Y_2O_3), and zirconia (Zr_2O) [11]. Carbon serves to remove SiO_2 from the surface of the SiC powder, facilitating the formation of point defects and enhancing surface diffusion. Boron prevents surface diffusion induced grain growth, promoting sintering. The effects of oxide sintering aids is still a topic of investigation and have yet to be entirely determined [11].

With the help of sintering aids, sintering begins at 1400 °C. When α-SiC is used as a raw powder, a sintering temperature between 2000 and 2300 °C is required; however, because of the α to β phase transition, sintering is performed at a temperature below 2100 °C when β-SiC is the starting phase, in order to avoid abnormal grain growth [11]. In addition to the influence of sintering aids, temperature, and the phase of the starting powder (α versus β), the starting particle size also impacts sintering characteristics. A smaller starting powder size (<1 μm, preferably), improves both sintering characteristics and mechanical properties.

2.3.3 Reaction-Bonded Silicon Carbide

Reaction forming of SiC is an alternative route for the fabrications of structural SiC components that has seen widespread use since its development in the 1950s [18]. Reaction-bonded silicon carbide (RBSiC) is attractive and economical for a couple of reasons:

1. It offers the capability for the production of near-net shape components.
2. The processing temperatures are greatly reduced in comparison to those of traditional sintering.

RBSiC is fabricated by a route involving the capillary infiltration of a compact of SiC particles (generally 5-10 um in diameter), a polymeric binder, and a source of carbon. The carbon source can either be raw carbon or can be introduced by the pyrolysis of the polymeric binding resin that to form the green compact [17]. The green compact for a RBSiC component is formed in the same manner as a green compact for sintering: isostatic pressing, slip casting, extrusion, or injection molding.

After the green compact is formed, the porous preform is infiltrated by liquid silicon at temperatures above the melting point of silicon [17]. Capillary pressure provides the driving force for infiltration due to the wetting of SiC by liquid silicon. The process for the fabrication of RBSiC is illustrated in Figure 9. Simultaneous to the infiltration of the porous preform, the reaction between liquid silicon and carbon in the preform results in additional SiC. The newly formed SiC crystallizes on the original SiC grains, bonding them together.

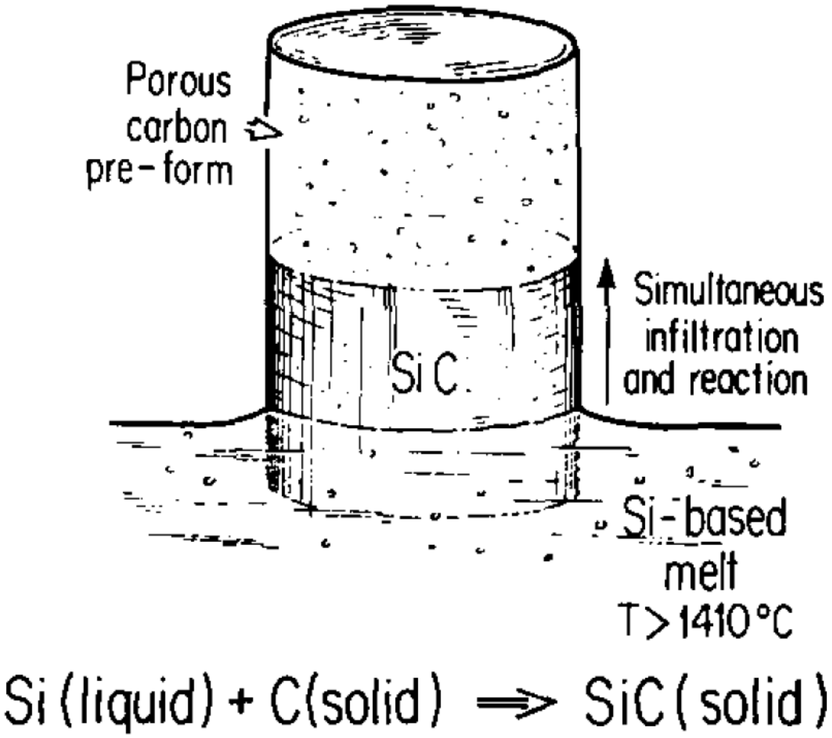

Figure 9: Schematic showing the infiltration of the porous silicon and carbon preform in the reaction-bonding process for the fabrication of SiC components [17]. The reaction between liquid silicon and carbon to form new SiC is provided.

The resulting microstructure consists of a mixture of SiC and free, unreacted silicon. Free silicon is observed in amounts of 5 to 25 vol%, with the optimum composition being approximately 10 vol% silicon and 90 vol% SiC [17]. A consequence of the interconnected network of free silicon around SiC particles is the generation of tremendous thermal stresses due to the mismatch between the thermal expansion of silicon and SiC ($CTE_{SiC} = 4.5x10^{-6}$ $°C^{-1}$ and $CTE_{Si} = 2.5x10^{-6}$ $°C^{-1}$) [10]. These thermal stresses may result in micro- or even macro-cracking when cooling rates are not well controlled; it is impossible to avoid these thermal stresses altogether. In comparison to SSiC, other material performance characteristics are also affected by the presence of free silicon, including the mechanical properties, electrical properties, corrosion resistance, and high temperature performance.

2.3.4 Graphite-Loaded Silicon Carbide

GLSiC has recently garnered significant interest for its potential to provide tribological improvement over traditional SSiC. Unlike SSiC and RBSiC, however, the manufacturing, properties, and microstructural characteristics of GLSiC are not well documented in literature. Information is currently only available in the form of patents and marketing material for mechanical seal suppliers. A 1994 patent by Talbert *et al.* touts “a high degree of lubricity as a result of large graphite inclusions in the body” [19]. The patent describes graphite inclusions averaging 100 μm formed by spray drying a slurry containing graphite particles, a carrier fluid, and a binder followed by blending the graphite agglomerates and SiC into a raw batch and sintering the green body at a temperature ranging from 2050 to 2200 ^{o}C. A 2002 patent by Wilkins E. G. provides insight into the tribological improvements of GLSiC compared to “plain” SiC [20]. Wilkins states that the graphite particles reduce frictional drag on a mating surface through intrinsic lubricating properties or hydrodynamic effects. In particular, the inclusions act as fluid reservoirs and provide hydrodynamic lift to force a slight separation of the contacting seal faces and reduce wear. To better understand these mechanisms, one must consider the lubrication regimes in mechanical seals and the concepts of hydrostatic and hydrodynamic pressures.

2.4 TRIBOLOGICAL CONSIDERATIONS FOR MECHANICAL SEALS

Mechanical seals are critical components in equipment such as pumps, agitators, and mixers that rely on rotating shafts passing from one environment to another. Often, the shaft will pass from a process fluid of interest (such as medicine, oil, or water) to the environment (atmosphere). Two mechanical seals are incorporated into the system to prevent leakage of process fluid: a stationary mechanical seal and a spring-loaded mechanical seal that rotates with the shaft. An axial closing force is applied onto the rotating seal in order to maintain tight contact between the two seal faces and prevent leakage of fluid. The lifetime of mechanical seals is directly related to their tribological performance in service. This tribological performance, however, is a strong function of the rotational speed of the shaft, the viscosity of the fluid, and the closing force on the seals. The operating lubrication mode for the seal contact will be dependent upon these service parameters and describes the magnitude of friction and wear that the seal faces sustain. Understanding the tribological behavior of seals (and methods for improving this behavior) is critical to improving component longevity.

2.4.1 Lubrication of Mechanical Seals

Vital to the longevity of the seal faces is the thin lubricating film that develops between the rotating faces that minimizes face-to-face contact, leading to a reduction of frictional torque and wear. This lubricating film develops as a result of hydrostatic and hydrodynamic pressure [21]. Hydrostatic pressure arises from the radial pressure differential that exists across the seal face (with pressurized fluid driven to leak towards atmospheric pressure); hydrodynamic pressure acts against the axial closing force and is generated by the sliding motion between the seal faces.

The thickness of the lubricating film will depend on the magnitude of the hydrostatic and hydrodynamic pressure acting against the closing force on the seals. There are three regimes of lubrication classified by the relative difference of the lubricating film thickness, *h*, and the surface roughness of the seal face, *R*: boundary lubrication (h < R), mixed lubrication ($h \sim R$), and hydrodynamic lubrication ($h > R$) [21]. These lubrication regimes are schematically represented in Figure 10. Boundary lubrication consists of nearly dry contact between the seal faces with high friction and wear but low process fluid leakage; mixed lubrication allows shearing forces to be shared between the fluid film and asperity contact between faces (causing moderate friction, wear, and leakage); hydrodynamic lubrication is established when a full fluid film has formed and no contact occurs between faces, resulting in minimal friction and wear at the cost of excessive leakage. For mechanical seals, the application determines how to balance seal face longevity and process fluid leakage.

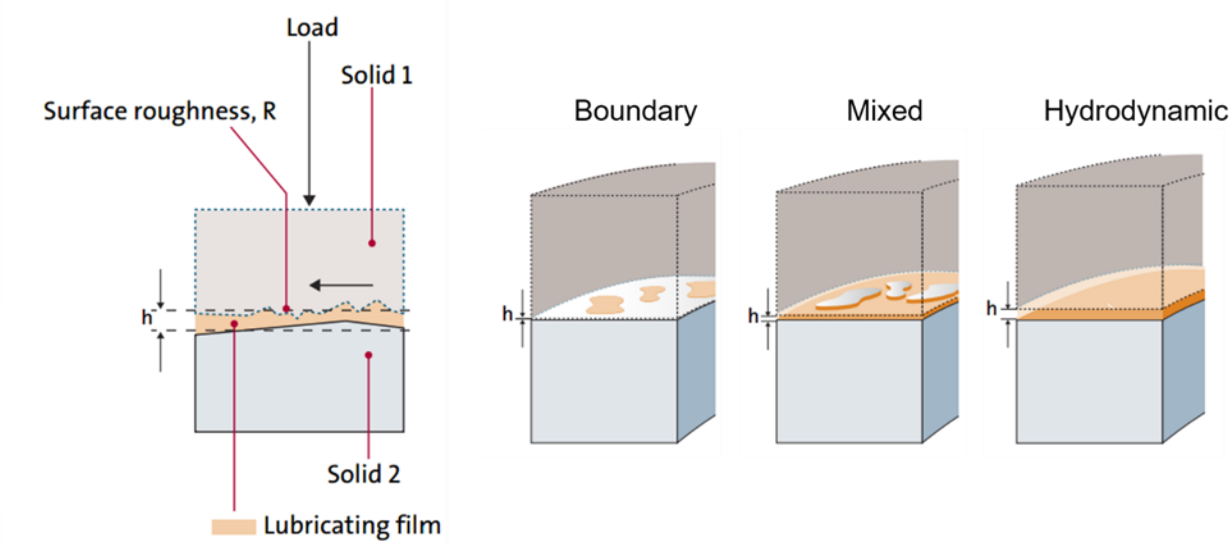

Figure 10: Lubrication regimes for two contacting mechanical seal faces under a closing load [21].

The operating lubrication regime for a specific application is a function of numerous parameters pertaining to the shaft, mechanical seal, spring, processing fluid, fluid pressure, and rotational seal velocity [21]. Mathematical model development for the prediction of regime boundaries has been a popular research effort for several decades. However, due to the complexity of these models' dependence on operating parameters, further discussion is outside of the scope of this report. Instead, the dependence on fluid viscosity (η), seal face rotational velocity (v), seal width (r), and seal closing force (F_N) will be greatly simplified and predicted by a general "lubrication parameter", G:

$$G = \eta v \Delta r / F_N \tag{5}$$

The friction coefficient at the seal contact interface acts as a function of G, as seen in the Stribeck curve shown in Figure 11; the operating lubrication regimes are labeled based on the friction coefficient behavior.

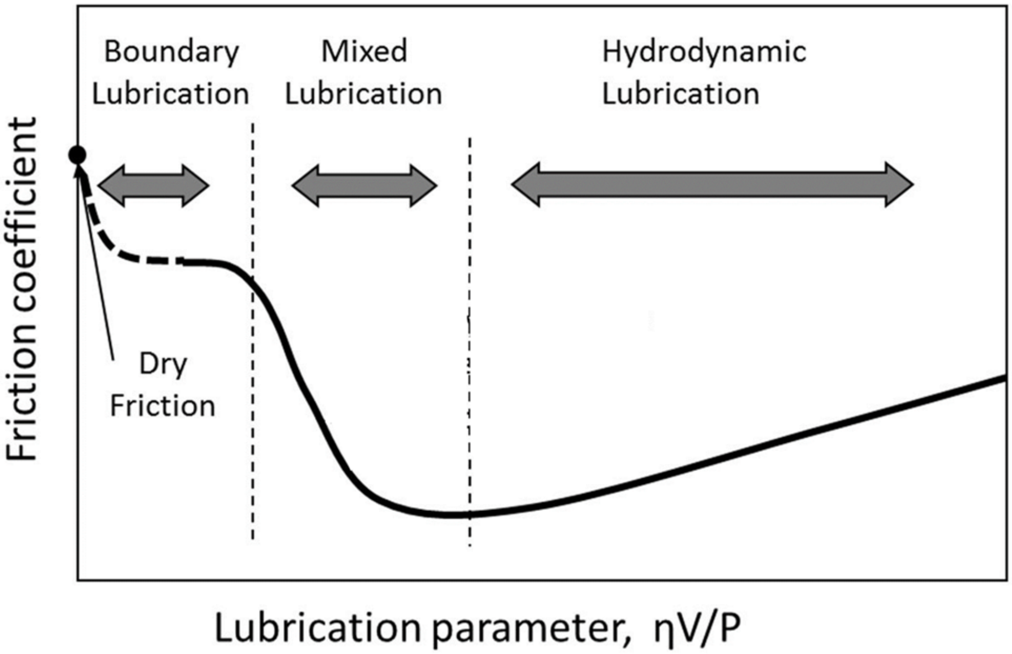

Figure 11: Stribeck curve demonstrating the friction coefficient dependence on operating parameters [22].

Friction is highest for boundary lubrication (dry contact) and experiences a minimum at the interface of mixed and hydrodynamic lubrication (Figure 11). This minimum value for friction is ideal for the application of mechanical seals [21]. If the seal begins to operate any further into the hydrodynamic regime, however, process fluid leakage increases exponentially. To avoid strong hydrodynamic pressures acting between the two faces, mechanical seals are rigorously lapped to obtain the minimum surface roughness possible. Perfectly parallel and flat faces will produce no hydrodynamic pressure, while any tilting or local change in seal face clearance will compress the fluid layer. It should be noted, however, that a complete lack of hydrodynamic pressure to counteract the seal closing force will induce boundary lubrication conditions; a compromise must be met for ideal mechanical seal performance. This compromise can be reached by engineering deterministic surface asperities (such as grooves or pores) into the mechanical seal faces to provide local, controlled hydrodynamic contributions.

2.4.2 Controlled Surface Features of Seal Faces

The primary contributor to mechanical seal performance is the selection of a seal face material that offers appropriate thermal conductivity, hardness, fracture toughness, and chemical compatibility for a particular application. A curious engineer, however, must consider what more can be done to improve the performance beyond the initial materials selection; in particular, how can seal face features be altered or deterministically controlled to improve lifetime and performance? In tribology, this is known as texturing [23]. There are three primary functions intended to be induced by texturing:

1. Trap debris that would otherwise abrade the surfaces
2. Serve as reservoirs or channels to supply lubricant to the contact interface

3. Alter the hydrodynamic pressure distribution to promote stiffness in the lubricating film

The first and second functions are predominantly beneficial in the boundary and mixed lubrication regimes; the third function is utilized to establish and maintain a complete lubricating film layer. Few, if any, research efforts have been conducted to study the trapping of debris in micropores (function 1). Instead, early advances in tribological texturing focused primarily on the trapping of lubricant in micropores (function 2) [24]. The proposed mechanism for lubrication is termed µ-pool lubrication: trapped, pressurized lubricant in micro-pores escapes and forms a localized micro-hydrodynamic lubricant film to prevent local lubricant starvation. The ability of lubricant to escape and form a micro-film will depend on the fluid viscosity, seal sliding velocity, and micropore orientation with the sliding direction. Pettersson *et al*. obtained experimental wear data on diamond-like carbon (DLC) coated silicon wafers with grooves (20 µm wide, 5 µm deep) etched into the surface [25]. It was found that the friction coefficient and wear were significantly reduced when the lubricant-filled grooves were oriented perpendicular to the sliding direction; this allowed for the lubricant to escape the grooves and permeate across the surface between grooves.

While lubrication trapping is an effective method of extending seal face lifetime in boundary or mixed lubrication regimes, most modern efforts are focused on the third function of texturing: to alter the hydrodynamic pressure distribution to promote hydrodynamic lubrication. This research was catalyzed by novel techniques such as laser-surface etching allowing control of micro-asperity geometry, size, orientation, and distribution [23]. The possible parameters that can be altered when considering controlled surface features on seal faces are represented in Figure 12. For micro-pores that are induced to develop hydrodynamic lift at the contact interface, the primary parameters of interest are pore size (diameter in the sliding direction), pore depth (relative to the pore diameter), pore geometry (spherical, triangular, cylindrical, etc.), and the area ratio of pores on the surface. Several studies have cited reductions on the order of 40 to 60% in frictional torque and interface temperature when these parameters are optimized [23].

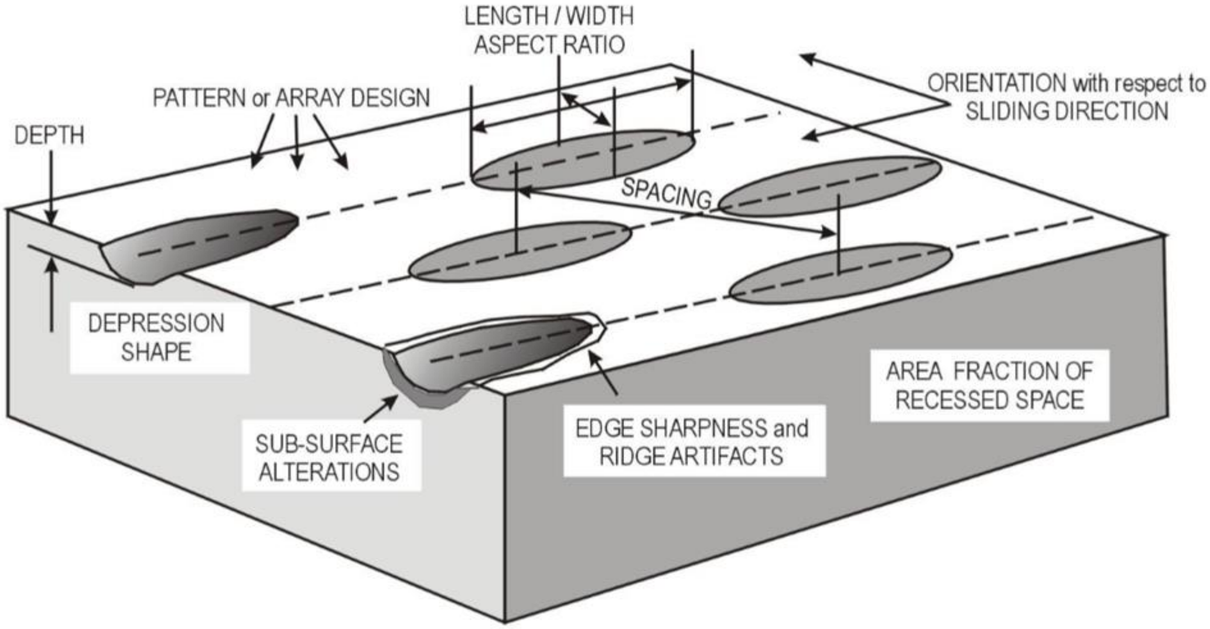

Figure 12: An illustration of possible controlled surface feature parameters in mechanical face seals [23].

There is, however, large inconsistency in the methods and results amongst research efforts in this field. This is partially due to the dependence of hydrodynamic pressure on fluid viscosity, rotational speed, and seal closing force; thus, there is no perfect solution to optimize the previously stated parameters unless a seal is designed for a particular application. There are a few rules of thumb and mechanisms that are consistent among successful results. In general, a pore depth to pore diameter ratio of approximately 0.05 – 0.3 (shallow) and a pore area density of approximately 20% is desired for maximum reduction of friction [26]. The accepted mechanism for friction reduction is a downward shift of the Stribeck curve (Figure 13) to facilitate seal operation at the boundary of mixed and hydrodynamic regimes (where a complete lubricating film is established but is not

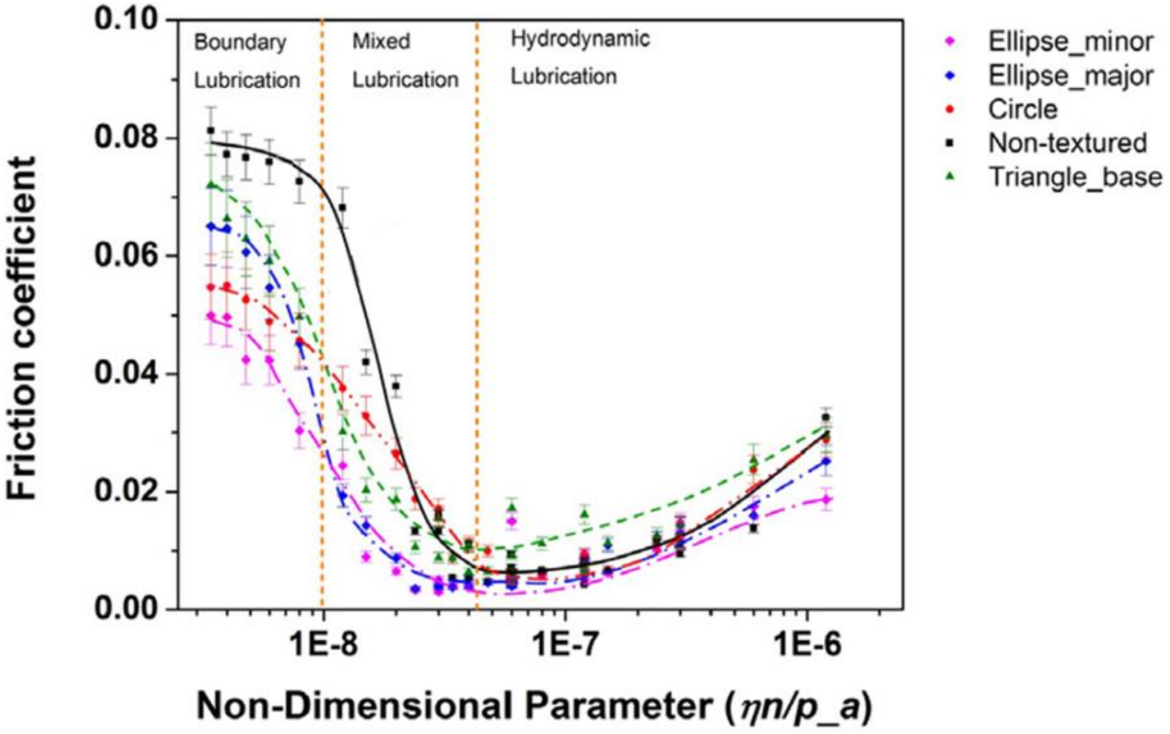

Figure 13: Deterministic surface pores produce a shift in the Stribeck curve to lower friction coefficients for different pore geometries. Note that the curve for an untextured seal is black [27].

large enough to cause excessive leakage). This phenomenon is clear for different pore geometries in Figure [27]. As for pore size, successful wear data has been produced for diameters ranging from 5 to 200 μm (shown in Figure 14); it is unclear what particular effect this has on seal performance, but the size often appears to be secondary in consideration behind depth-to-diameter ratio and surface area density.

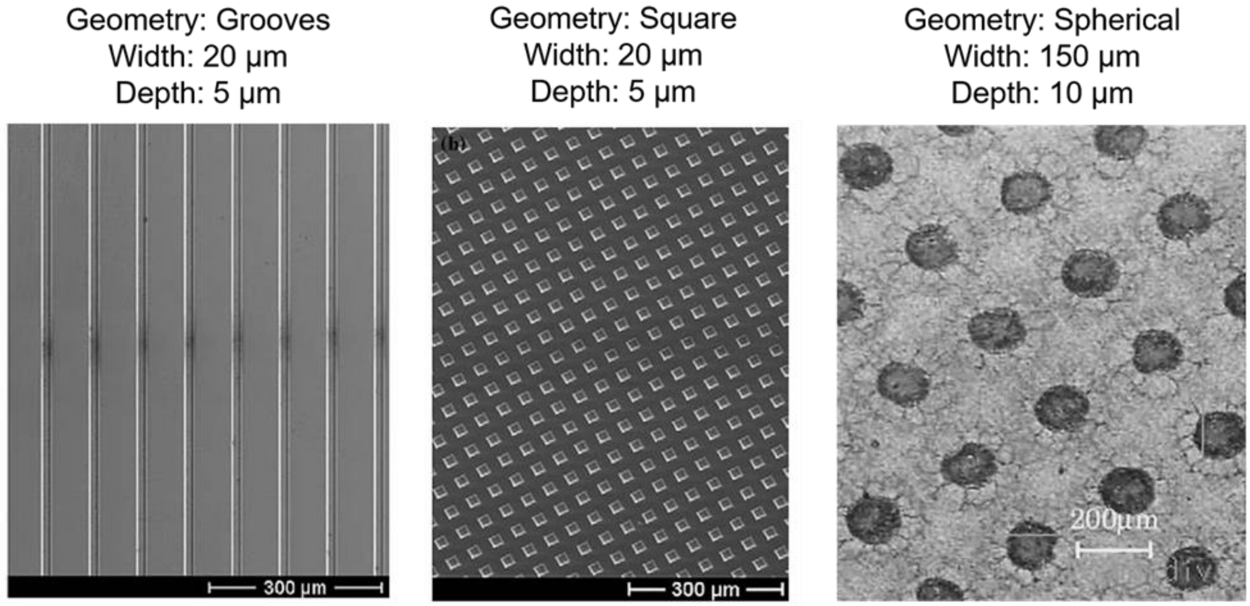

Figure 14: Surface pores processed by laser-etching are compared to demonstrate the variety of pore size, area density, depth, and geometry [25, 28].

2.4.3 Role of Graphite in Silicon Carbide Mechanical Seals

The performance of SiC as a seal face material is well documented; the performance of GLSiC for mechanical seal applications, conversely, has not been the focus of any significant publications. Insight into the explicit role of graphite particles is currently only available in GLSiC patents and marketing material from seal suppliers. The first patents for GLSiC propose benefits from the hydrodynamic effects and fluid reservoir behavior of graphite inclusions [19, 20]. Mechanical seal suppliers such as Morgan Advanced Materials and MicroGrain General Seals tout the unique topography of their

GLSiC seal faces that contribute tribological benefits throughout the entire seal lifetime [29, 30]. Huebner briefly states that the role of graphite particles is not to provide self-lubricating graphite into the sliding interface; rather, the soft graphite phase in a hard SiC matrix is pulled out upon lapping of the mechanical seal face [31]. This will result in distributed depressions on the seal face that act as controlled micro-asperities as discussed previously. Graphite's role as a second abradable phase in SiC is again mentioned to form "pockets" for lubricant storage by the Fluid Sealing Association [32]. Thus, it is postulated that the role of graphite is an indirect means to control surface features on SiC mechanical seal faces to improve tribological behavior.

The previously discussed methods of imparting surface features (such as laser surface etching) are advanced techniques that allow exact control on the shape, depth, geometry, and distribution of micro-asperities. However, such techniques will only impart features onto the surface of seal face materials; the bulk remains unaltered. Once the surface layer of these seals has worn down to the point that the surface features are indistinguishable, there will be no further improvement to the tribological behavior. Graphite nodules dispersed in SiC, conversely, will be present at both the surface and in the bulk. This implies that wearing down the surface will not remove surface features; instead, features will develop as previously buried particles become exposed and form new micro-pores. Thus, the natural phase of re-lapping a mechanical seal for refurbishment will re-instate controlled surface features without a secondary process such as laser etching (illustrated in Figure 15). The size and shape of newly formed pores is dependent on the characteristics of the previously existing graphite particles. Figure 15 shows one case of a lapped surface containing a variety of pore types (such as irregular, shallow, and deep pores). It can also be seen that pore diameter and depth is a function of graphite particle orientation with respect to the lapping surface. Thus, in direct contrast to the previously discussed methods of producing controlled surface features, one should expect a stochastic distribution of pore shapes, sizes, and area fractions based on the current depth of wear in the SiC mechanical seal. Beyond pore characteristics, two potential issues are highlighted in Figure 15: (1) remaining graphite particles at the surface and (2) SiC abrasive particles introduced due to edge breakdown of irregularly shaped pores. Despite these potential issues of GLSiC, Figure 15 illustrates the benefits of micro-pores on the surface that act as pits to trap abrasive particles and lubricant.

For graphite particle dispersion to act as a successful method of imparting surface features, various characteristics will need to be evaluated. What is the size, shape, and distribution of these particles in the matrix? Is the lapping procedure successful in pulling out the graphite phase? Is the dispersion of graphite particles in the matrix detrimental to the mechanical or thermal properties of the seal? It is expected that a statistical variance will exist for many of these parameters since this method is an indirect means to imparting surface features. The state of these parameters will depend on both the quality and method of manufacturing and will likely vary between suppliers. This report aims to determine the potential of GLSiC as an improvement to the performance and longevity of mechanical seals.

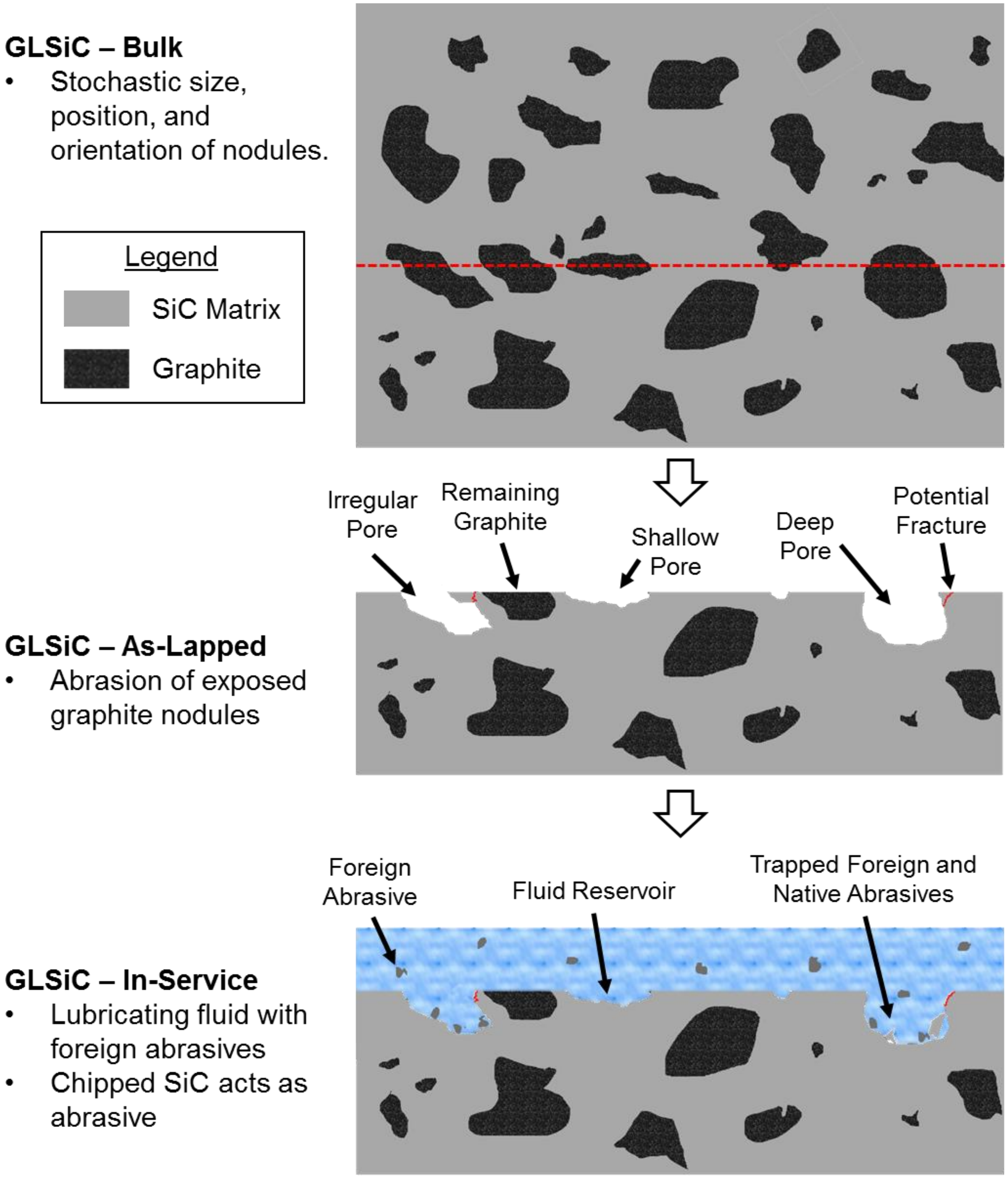

Figure 15: Abradable graphite phase is pulled out upon lapping of mechanical seal. Remaining depressions act as controlled surface features to trap debris, act as fluid reservoirs, and generate hydrodynamic lift.

3 PROJECT DESCRIPTION

AESSEAL's top priority is to provide seals of the highest quality to its customers. As such, performing a detailed quality assessment of seal suppliers was necessary to determine if their products uphold AESSEAL's standards. To this aim, end-product mechanical seals were delivered for an extensive materials characterization examination. Initially, four sample sets of unknown SiC type were provided with the designations of A, J, S, and D. The primary task at this stage of the project was the identification of SiC type by the detection of secondary silicon and graphite phases for the classification of RBSiC and GLSiC, respectively. The presence of secondary phases was broadly determined by density measurements, qualitatively identified by X-ray diffraction, and quantified by microstructural characterization. Following phase identification and quantification, the impact of secondary phases on the mechanical properties of each seal set was to be determined in order to assess their individual strengths and weaknesses in mechanical seal applications.

A key concern when selecting suppliers in international markets (where standards are less strict than stateside) is the quality and consistency of end-product seals. For this reason, AESSEAL provided three new sets of seals (FS, FR, and FG) from a separate supplier to compare to the characteristics of the SSiC, RBSiC, and GLSiC from current suppliers. The classification of SiC type was provided to expedite the analysis of these seal sets. Finally, seal specimens (MSG and MRBG) from Morgan Advanced Materials, a highly reputable stateside supplier, were provided to offer a baseline comparison for the quality of international suppliers of GLSiC. All seal specimen designations are provided in Table 1 with their SiC classification and supplier names. Despite the chronological order in which the seal specimens were analyzed, this report provides a comprehensive review of all nine seal sets for effective comparison.

Table 1**:** Sample Designation, supplier information, and sample type for each of the samples received from AESSEAL.

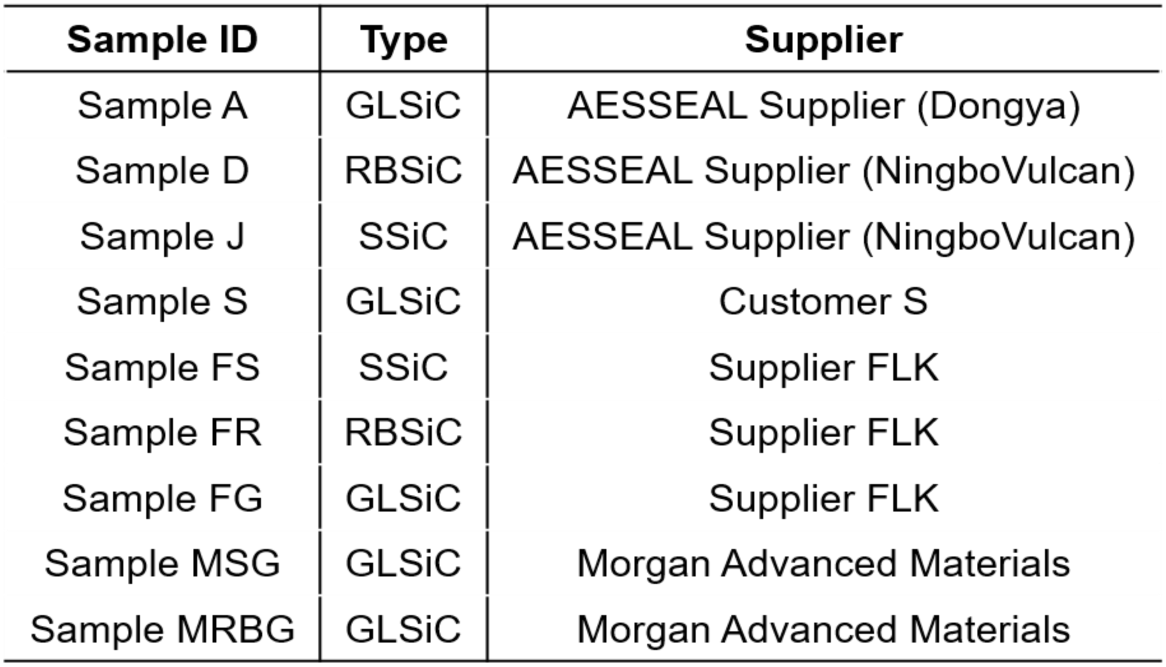

Sample ID	Type	Supplier
Sample A	GLSiC	AESSEAL Supplier (Dongya)
Sample D	RBSiC	AESSEAL Supplier (NingboVulcan)
Sample J	SSiC	AESSEAL Supplier (NingboVulcan)
Sample S	GLSiC	Customer S
Sample FS	SSiC	Supplier FLK
Sample FR	RBSiC	Supplier FLK
Sample FG	GLSiC	Supplier FLK
Sample MSG	GLSiC	Morgan Advanced Materials
Sample MRBG	GLSiC	Morgan Advanced Materials

4 EXPERIMENTAL

Project goals have been specifically described in the *Project Description* section. In this section, the experimental approaches and methodologies employed to assess mechanical seal quality, performance, and design are listed and explained. The sample designations, SiC type, and supplier have been provided in Table 1; further, an addendum was included as *Appendix A*, illustrating the provided SiC seals and their designations. Throughout the remainder of this report, the samples will be referred to by their AESSEAL-prescribed designations. The following methods have been employed in the identification, structural characterization, and microstructural characterization of the SiC seal face materials: optical light microscopy (OLM) and scanning electron microscopy (SEM) on the as-lapped and ceramographic surfaces, quantitative microstructural analysis, phase identification by X-ray diffraction (XRD), density determination by the water pycnometry, calculation of moduli by resonant ultrasound spectroscopy (RUS), microhardness, and compression testing. As shown in *Appendix A*, sample geometries created practical limitations in regard to what testing could be performed. Meticulous explanation is given regarding sample extraction orientation, orientation of the analyzed surface, and surface finish. Samples utilized for analysis in each of the following sections were extracted by sectioning with a 5” metal-bonded diamond wafering blade on an Allied TechCut 5 Saw.

4.1 CERAMOGRAPHIC EXAMINATION

Prior to ceramographic examination, cross-sectional samples were mounted in a two-part thermosetting epoxy and subsequently ground and polished using sequentially finer grits of diamond abrasives until a fine surface finish was achieved. Samples were analyzed using OLM and SEM. The evaluation of ceramography samples is valuable for two primary reasons:

1. Ceramography samples provide a view of the cross-section of the mechanical seal, rather than just the surface. This allows an investigation of microstructural homogeneity throughout the bulk.
2. In ceramographic sample preparation, a series of controlled polishing steps on a small samples are employed. It is desirable to minimize polishing time in order to mitigate the pulling-out of phases that are soft in comparison to the surrounding matrix, which would include free silicon, graphite, and non-SiC inclusions. However, lapping is carried out for a time greater than 1 h with the intention of maximizing flatness. This can result in the extraction of softer phases, especially graphite. Therefore, ceramographic samples offer a valuable comparison to the as-lapped surface, allowing an evaluation of AESSEAL's lapping procedure.

To supplement qualitative ceramographic evaluation, the phases present and the surface features of ceramography samples were analyzed using both automated and manual techniques with the aid of the ImageJ Automated Image Analysis Software [34]. Phase fractions and particle size distributions have wide-reaching impact on the physical, mechanical, and chemical properties as well as seal performance. For the RBSiC sample, the phase fraction of free silicon and the approximate SiC particle size were determined from OLM and SEM micrographs. For samples containing graphite, the size and area/volume fractions were determined. Further, for the sample having the highest graphite-content, a comparison between the graphite characteristics and distribution of both the as-lapped mechanical seal surface and the cross-sectional samples was conducted in order to understand the effect of AESSEAL's lapping procedure on surface characteristics and to hypothesize the resulting design/service characteristics.

4.2 X-RAY DIFFRACTION

X-ray diffraction (XRD) is a used for investigating the phases present in a material. In a crystalline material, the spacing between crystallographic planes of the structure are unique to that particular structure and composition. One can indirectly measure the interplanar spacing using a probe with the appropriate wavelength (angstroms Å): X-rays. Their wavelengths, on the scale of angstroms, allow X-rays to diffract off of the crystallographic planes with a particular spacing d_{hkl} and produce a reflected beam of high intensity. The angle at which this phenomenon occurs satisfies Bragg's Law, shown in Equation 6 [35]:

$$n\lambda = 2d_{hkl} \sin\theta \tag{6}$$

where λ is the incident wavelength, n is the order of reflection, and θ is the angle of incidence. By measuring the intensity of a reflected beam as a function of incidence angle, the various ararngements of the crystallographic planes may be elucidated. Measurements are carried out using an instrument such as the one described by the schematic in Figure 16.

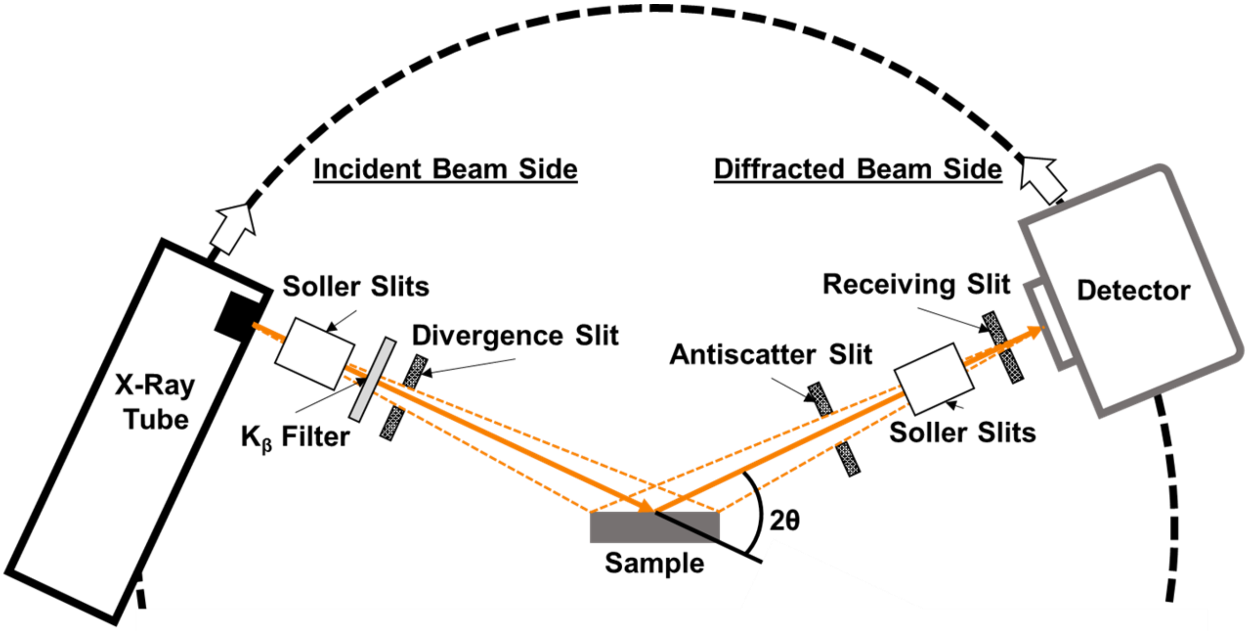

Figure 16: Schematic illustrating a laboratory X-ray diffractometer. XRD samples are sectioned into thin slices; X-rays were incident on a saw cut face.

X-ray diffraction data for this investigation were collected on polycrystalline SiC samples cut from the seals. It is assumed that there are a sufficient number of favorably oriented grains in the polycrystalline samples that diffraction from all planes will be observed. Data were collected on a PANalytical Empyrean X-ray Diffractometer in conventional Bragg-Brentano geometry using a θ-θ configuration. Data were collected over a range of 25-100° 2θ with a step size of 0.01° 2θ using Cu-Kα radiation (λ ~= 1.54056 Å) and a PIXcel detector. Data were analyzed using GSAS-II [36] and MATLAB®.

4.3 DENSITY DETERMINATION

The density of samples from each supplier was determined and compared with the published theoretical densities of SiC, silicon, and graphite. Water pycnometry, utilizing the Archimedes method and a balance accurate to the fourth decimal place, was used to measure the density of three samples from each of the nine sets of seals, and each measurement was replicated five times. The Archimedes Method compares the mass of the sample in air to its mass in water; this determination considers the buoyant force's effect, which allows for a density calculation using Equation 7. In Equation 7, ρ is density and *m* is mass.

$$\rho_{SiC} = \frac{m_0}{m_0 - m_{water}} \cdot \rho_{water} \tag{7}$$

Each seal's average density has been compared to literature. There is a distinct difference between the densities of SSiC, RBSiC, and GLSiC due to the presence of secondary phases (free silicon in the reaction-bonded samples, and graphite in the graphite-loaded samples). Density determination provides information about the presence of a significant volume fraction of a second phase. Following the previously discussed procedure, it would be possible for AESSEAL Inc. to determine the density of seal and have an idea of the fraction of secondary phases (either free silicon or graphite) present in their SiC mechanical seals.

4.4 RESONANT ULTRASOUND SPECTROSCOPY

Resonant ultrasound spectroscopy (RUS) is a technique which probes the vibrational eigenmodes of a sample of well-defined shape to determine its elastic moduli [37]. These eigenmodes determine the resonant frequencies (eigenfrequencies) of a sample; this means that if the sample were mechanically excited at the resonant frequency, a standing mechanical wave will cause the sample to vibrate vigorously (i.e. its deformation will be pronounced). The frequency at which these vibrational modes will occur is a function of the mass, shape, dimensions, and elastic constants of the sample.

Therefore, if the sample's shape, size, and mass are known, and the resonant frequencies are measured experimentally, then the elastic constants can be resolved via iterative fitting to a model. Using an "educated guess" of the elastic moduli as input values in addition to the sample dimensions and mass, the model computes theoretical eigenfrequencies and then adjusts the input moduli values until a suitable match between the computed and measured frequencies is obtained.

A typical RUS setup is shown in Figure 17. The sample is usually a parallelepiped with dimensions of 1-8 mm. It is held lightly between two piezoelectric transducers that each contact the sample at one point. One of the transducers (the driving transducer)

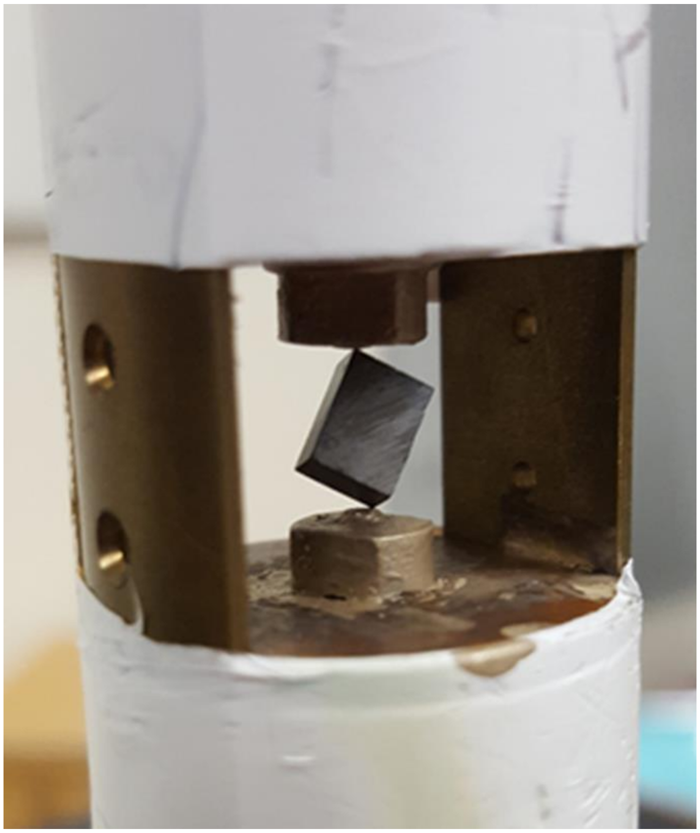

Figure 17: SiC sample in the RUS experimental apparatus. The sample is corner-mounted between a driving transducer (top) and receiving transducer (bottom).

excites the sample by sweeping through a range of ultrasonic frequencies. The other transducer (receiving transducer) is used to measure the response of the sample to these mechanical excitations. When the driving transducer excites the sample at one of its resonant frequencies, a large response will be detected by the receiving transducer, which appears as a spike in voltage. An example of this is shown in Figure 18.

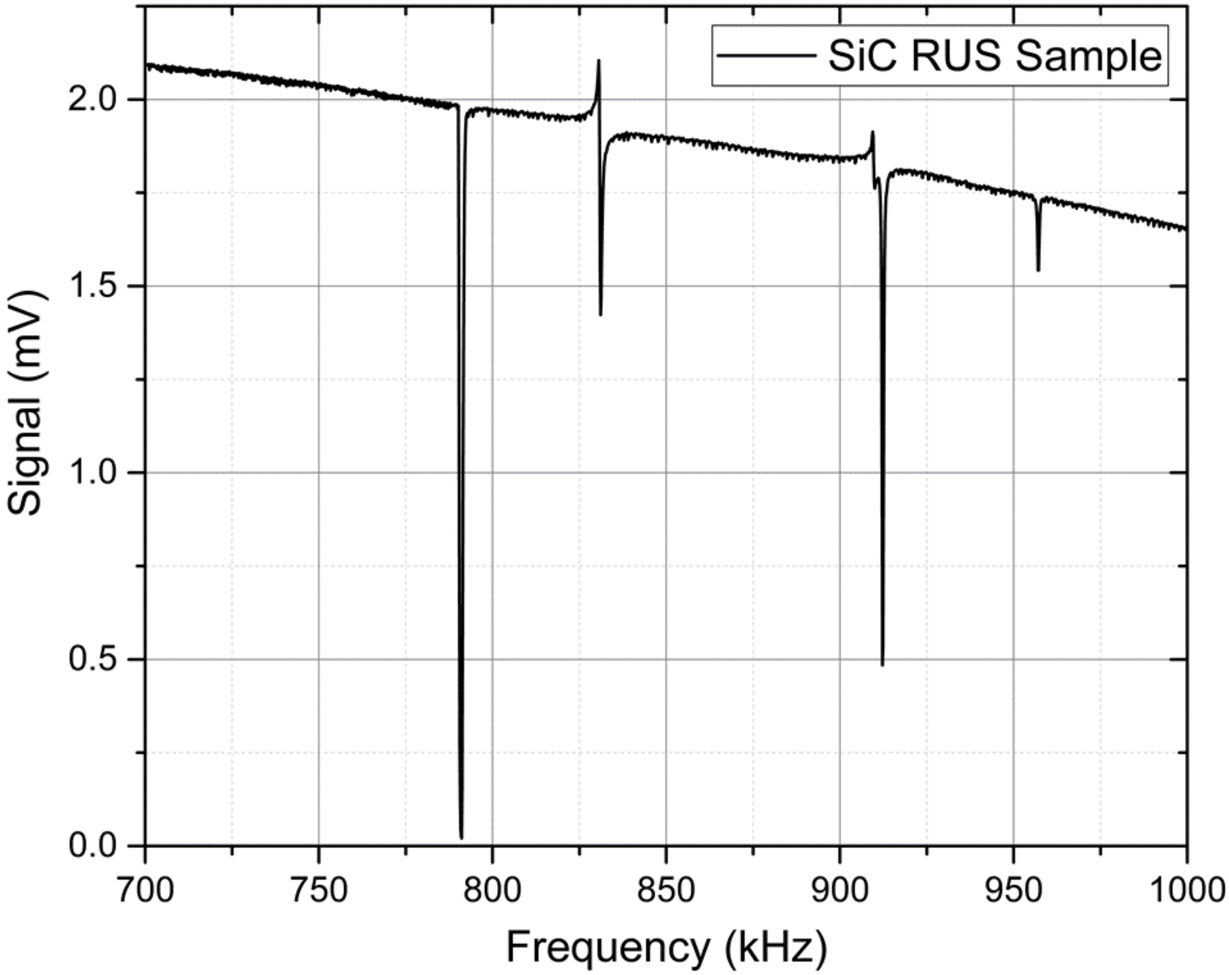

Figure 18: Example RUS data set for a representative SiC sample. A range of frequencies are swept and sample response is measured. The frequencies at which the peaks appear, along with sample dimensions and mass, are used to calculate the moduli.

4.5 MICROHARDNESS

Vickers microhardness was employed to evaluate the resistance to wear, protection from abrasives, and deformation characteristics of each of the nine sets of mechanical seals. Vicker's microhardness involves an automated instrument making an indentation with a four-sided diamond pyramidal indenter under the application of a specified load. The Vickers microhardness number, which is a measure of a material's ability to resist deformation is determined from the size of the indentation. Indentation size is manually measured using an optical microscope. Twenty-five microhardness indentations using 1000 gram-force were made on the as-polished ceramographic sample for each of the nine sets of mechanical seals. The indentations were made and measured in accordance with ASTM C1327 [38]. Instances of chipping to accommodate deformation induced by the hardness indentation were observed, specifically for samples formed by reaction-bonding; in these instances, the Vickers microhardness was not measured due to difficulties measuring indentation size and inhomogeneity in deformation accommodation.

4.6 COMPRESSION TESTING

The plan for compression testing called for cylindrical samples approximately 3 mm in diameter and 4.5 mm in length in order to preserve a comparable length to diameter ratio of 1.5 for each set of SiC mechanical seals. Samples meeting these criteria were extracted from the provided intact silicon carbide seal samples. Due to the high hardness of SiC, a hole saw bit impregnated with diamond was used to cut cylindrical samples of the appropriate diameter. These samples were then further processed to the corresponding length based on the diameter by cutting any excess material from the end of the sample.

Compression testing was conducted using a MTS 810 Universal Testing Machine. The testing apparatus was setup as seen in Figure 19. Two steel platens (50 mm diameter) were used as points of contact to the hydraulic grips to better distribute load during testing. Tungsten carbide platens were placed between the sample and the steel platens to act as a buffer for load distribution between the harder silicon carbide and the softer steel. Compression testing was conducted at a crosshead displacement rate of 0.0033 mm/min, which resulted in tests that lasted approximately 10 minutes. A review of literature suggested that this was an appropriate strain rate for compression testing, as SiC does not exhibit significant strain rate sensitivity [39].

These samples were not fabricated to an ASTM Standard for compression testing due to the limitations in sample size. Further, difficulties in sample fabrication were widespread: the cylindrical walls fabricated using the holesaw were often imperfect, the SiC mechanical seals destroyed numerous diamond holesaw bits, and a diamond wafering saw was needed to section the loading faces to obtain the necessary length to diameter ratios. Therefore, the extent of compression testing was highly limited by sample fabrication capabilities as will be discussed further in the *Results and Discussion* section.

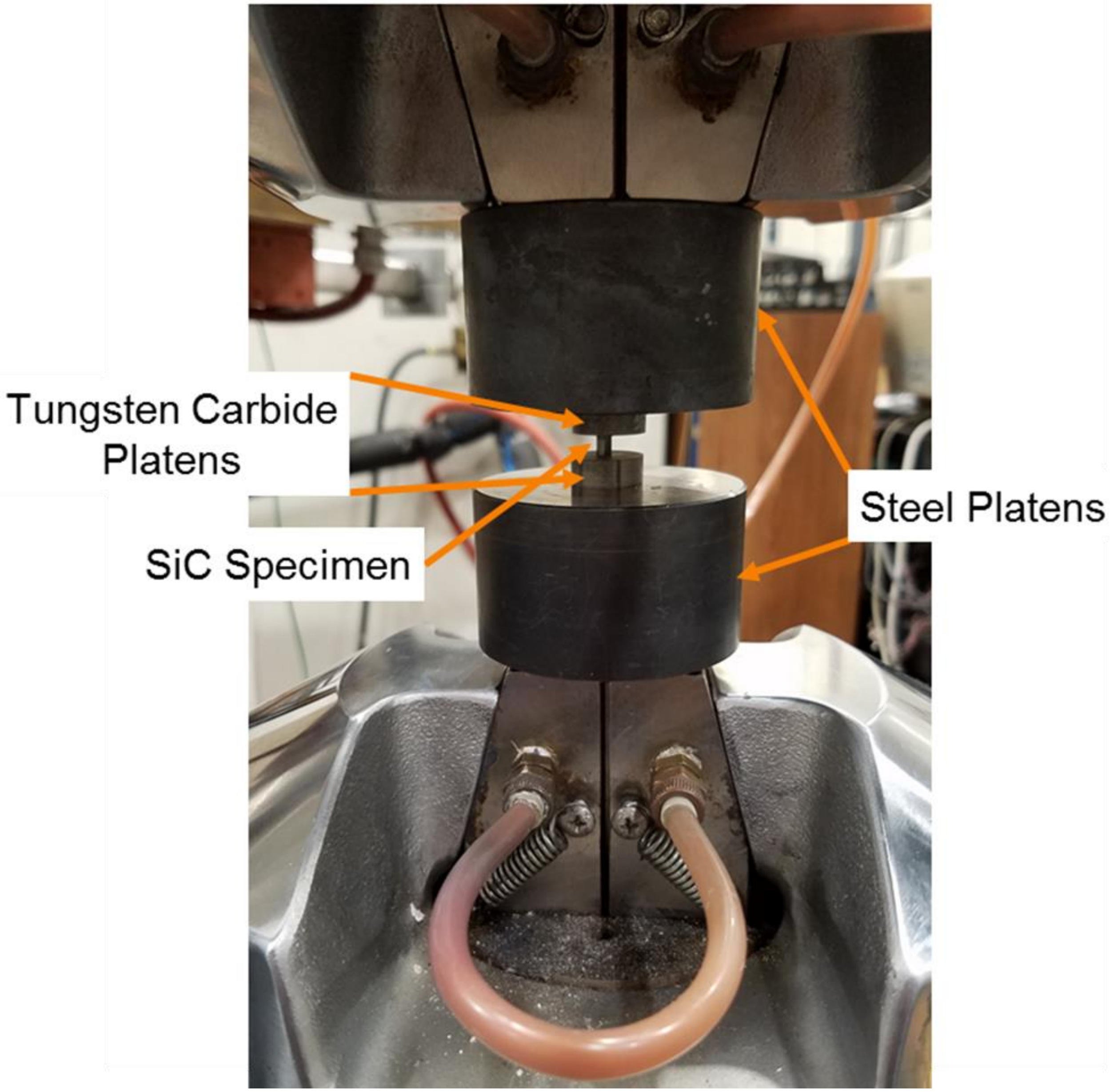

Figure 19: Compressing testing configuration for the cylindrical SiC samples tested in the MTS Universal Materials Testing System.

5 RESULTS AND DISCUSSION

An exhaustive analysis of each of the nine sets of SiC mechanical seals received from AESSEAL is presented in a three-phase approach:

Section 5.1 - Microstructural Evaluation: Ceramographic Examination and XRD

Section 5.2 - Physical Property Evaluation: Density Determination and RUS

Section 5.3 - Mechanical Property Evaluation: Microhardness and Compression

Each section of analysis is constructive; the gap between microstructure and properties to expected seal performance is bridged. Further, pertinent discussion is provided to aid AESSEAL in making key design decisions when seal quality or materials design are in question, but an extensive evaluation of microstructure and properties is not possible.

5.1 MICROSTRUCTURAL EVALUATION

Critical to understanding the performance of the provided SiC mechanical seals, which is dictated by their physical, chemical, and mechanical properties, is gaining a microstructural understanding. The microstructural knowledge can be directly linked to seal performance through the influence of the constituents that are present and their distribution. This knowledge leads to a logical evaluation of the quality of each set of mechanical seals provided by AESSEAL Inc. The following sections provide the results of ceramographic examination and XRD. The results and related discussion are divided into sections for each type of mechanical seal (SSiC, RBSiC, and GLSiC). Following pertinent discussion, conclusions will be proposed based on the results of microstructural analysis; further, the design implications are expounded upon when possible.

5.1.1 Sintered Silicon Carbide Samples

SSiC samples accounted for two of the nine sets of mechanical seals provided by AESSEAL. Sample sets J and FS were the only SSiC samples provided by AESSEAL. SSiC mechanical seals are formed by pressureless sintering of a SiC compact at temperatures between 2100 and 2300 ^{o}C, forming a component near theoretical density. SSiC is expected to consist of α-SiC with a minimal fraction of secondary constituents.

Ceramographic samples were prepared from cross-sectional samples extracted from Samples J and FS. After ceramographic preparation, the samples were analyzed using scanning electron microscopy. SEM micrographs from Sample J and Sample FS are shown in Figures 20 and 21, respectively. The microstructural features observed in the two SSiC sample were consistent. The prominent microstructural characteristic observed in the as-polished ceramographic sample was the presence of graphite in the form of small, primarily intact nodules ranging from several hundred nanometers to several microns in diameter. The graphite nodules were present at a volume fraction of approximately 6% in both Sample J and FS as measured by quantitative phase analysis employing the ImageJ Automated Image Analysis Software [34]. The degree of pull-out resulting from ceramographic preparation procedure was minimal. There was no observed porosity remaining from incomplete sintering. The graphite morphology observed is the typical flake-like morphology of graphite widely reported in literature. The graphite appears dark in the SEM due to its high electrical conductivity and low Z (atomic number).

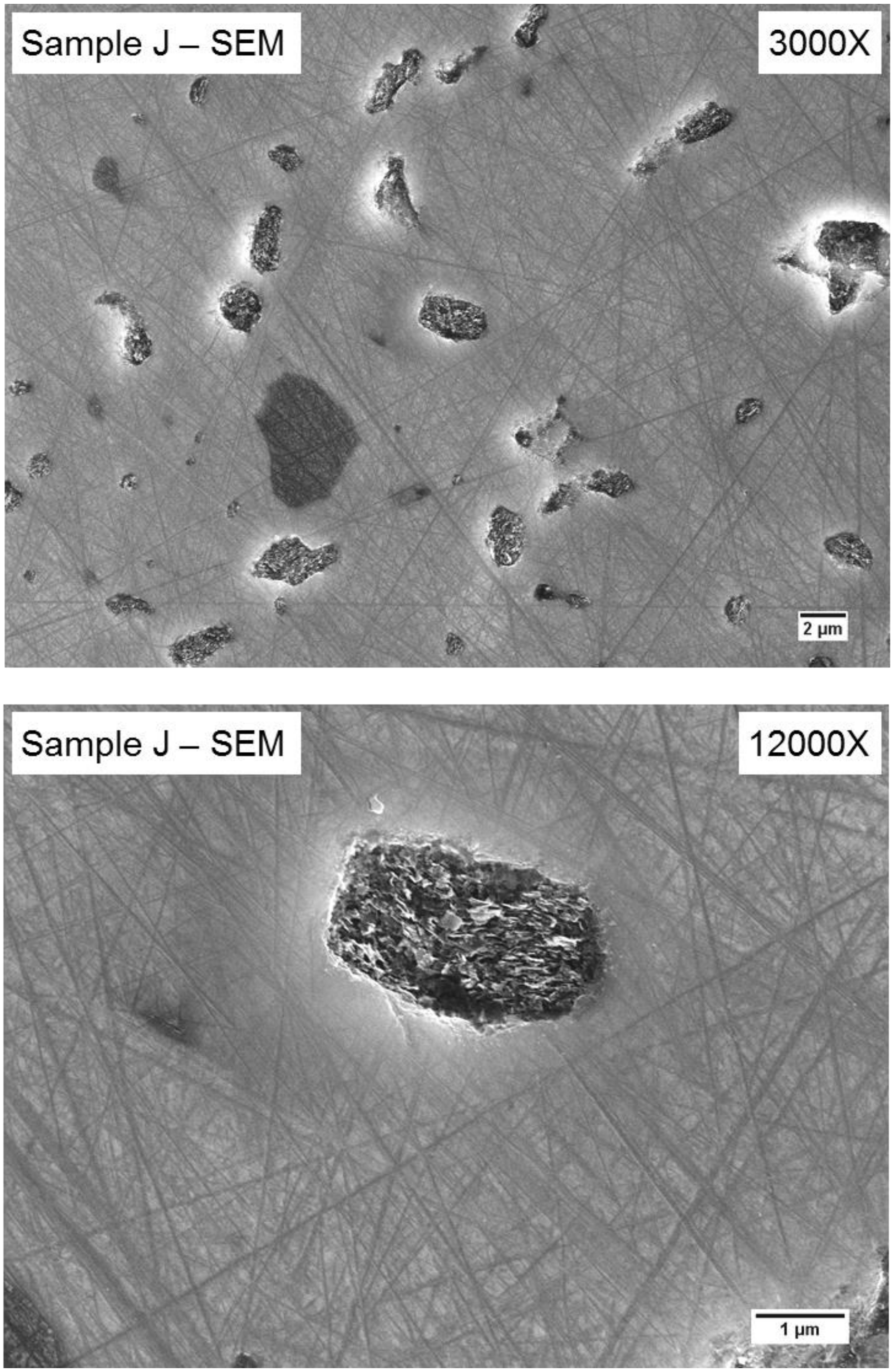

Figure 20: SEM micrographs at 3000X (top) and 12000X (bottom) illustrating the microstructural features of the Sample J ceramography specimen in the as-polished condition. Small graphite nodules (100 nm – 5 µm diameter) are uniformly distributed in the SiC matrix at a volume fraction of approximately 6%.

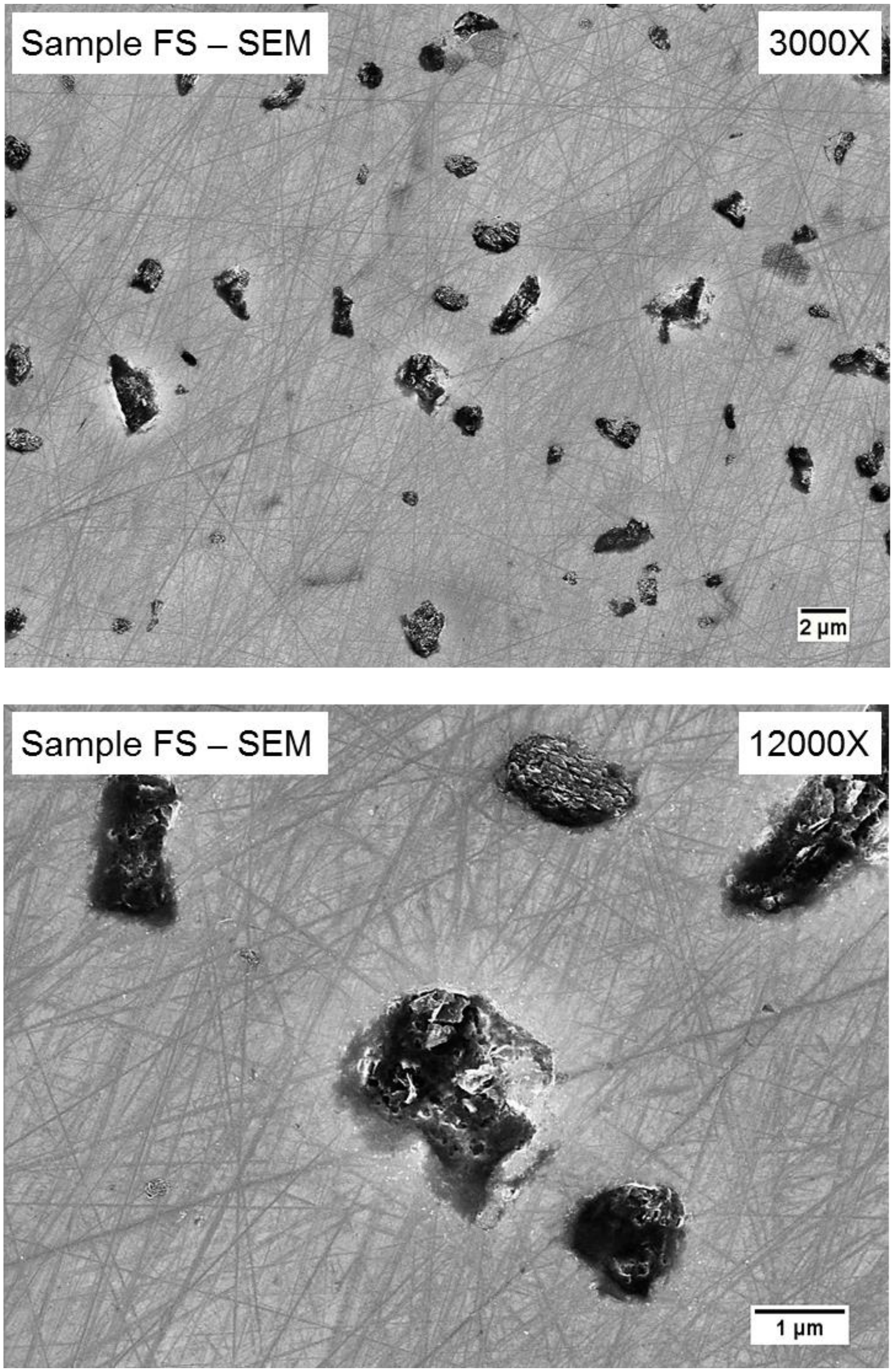

Figure 21: SEM micrographs at 3000X (top) and 12000X (bottom) illustrating the microstructural features of the Sample FS ceramography specimen in the as-polished condition. Small graphite nodules with an average size of 0.9 µm are uniformly distributed in the SiC matrix at a volume fraction of approximately 6%.

The observation of graphite in the SSiC was not expected, but is not unreasonable, as it can be attributed to one or two obvious sources of excess carbon:

1. The Acheson Process involves mixing SiO_2 with coke (carbon source); this does not result in the total conversion of the mixture to SiC. Further, unreacted carbon is the most common impurity in SiC. Depending on the starting grade of SiC that was crushed into the SiC powder used in the pressureless sintering process by which this component was fabricated, it is entirely plausible that the graphite nodules are residual coke particles.
2. Excess carbon may have also been introduced as either carbon black or as a carbon rich binder to act as a sintering aid during the pressureless sintering process. Carbon is the most common sintering aid added during pressureless sintering of SiC. To further investigate this avenue, SiC powder was received from Penn United Technologies Ltd. and was analyzed using SEM and XRD. The results of this analysis are provided in *Appendix B*. The presence of a carbon-rich binder was confirmed.

It is stressed that the small graphite nodules (several hundred nanometers to several microns in diameter) introduced during the manufacturing process are not intentionally added to influence the tribological properties of the mechanical seal. Therefore, it is advantageous to provide a distinct term to refer to these small nodules. For the remainder of this report, these nodules will be referred to as *native graphite*, which we define as graphite nodules introduced during SiC powder manufacturing or sintering that have a diameter on the order of 1 μm in diameter.

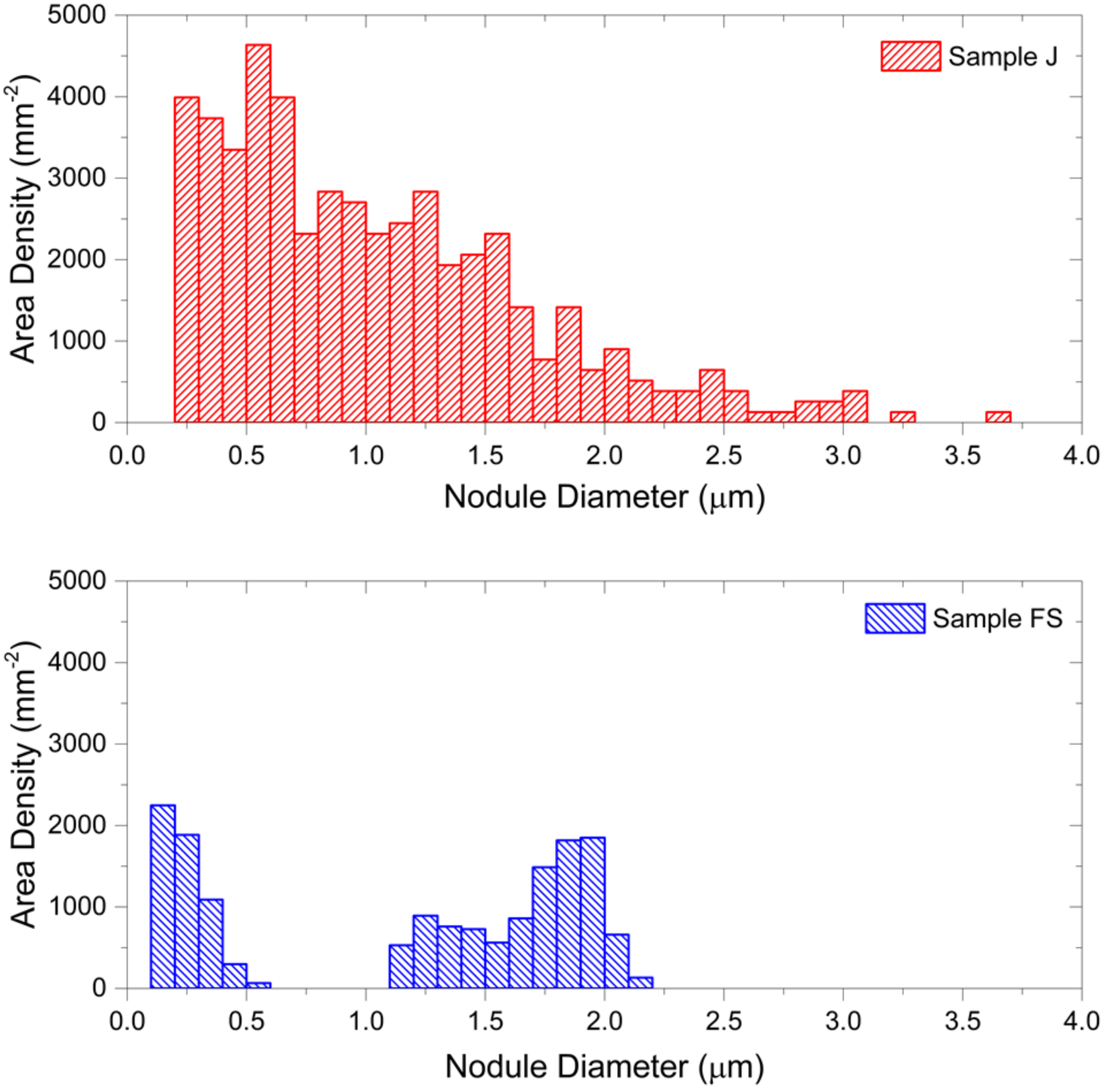

Figure 22: Plots of the density of native graphite nodules versus the nodule for the SSiC Samples J and FS. The volume fractions of native nodules, diameters, and their average sizes are provided in the plots.

Figure 22 presents the results of quantitative phase analysis completed using ImageJ Automated Image Analysis Software [34]. The average size of native graphite nodule sizes for Samples J and and FS were 1.0 μm and 0.9 μm, respectively. Similar native graphite distributions were observed in Samples J and FS. Since more than 1000 native nodules were analyzed for each sample, the data presented is statistically certain. An area of more than 10000 μm^2 was analyzed utilizing SEM images obtained with a quadrant backscatter detector (QBSD), providing enhanced Z (atomic number) contrast.

To further characterize the sintered samples, XRD was completed on samples extracted from Samples J and FS. The resulting XRD patterns are shown in Figure 23. A calculated pattern fitted to the experimental data with GSAS Crystallography Data Analysis Software is also plotted [36]. In order to fit the experimental data with a calculated XRD pattern, crystallographic information files (CIF file) that provide the crystallographic details necessary to calculate a theoretical pattern were imported into GSAS-II. For Samples J and FS, the CIF file utilized as a starting point for the calculated pattern was for the 6H-SiC polytype [40], which is the most common polytype of SiC. Further, minimal variation exists between the XRD patterns for the different polytypes of α-SiC, as the stacking order is the only difference between the polytypes; therefore, the relative peak intensities and interplanar spacing are minimally affected. The CIF files being employed are for powder diffraction, which provides random crystallographic orientation. However, the XRD of this investigation was performed on bulk samples. If the grain size is small enough and the material is isotropic, the error induced in the comparison of XRD data to powder XRD data is minimal. Thus, the fit of the experimental data for Samples J and FS to the 6H-SiC polytype is accurate. The planes to which each intensity peak corresponds are indicated in Figure 23.

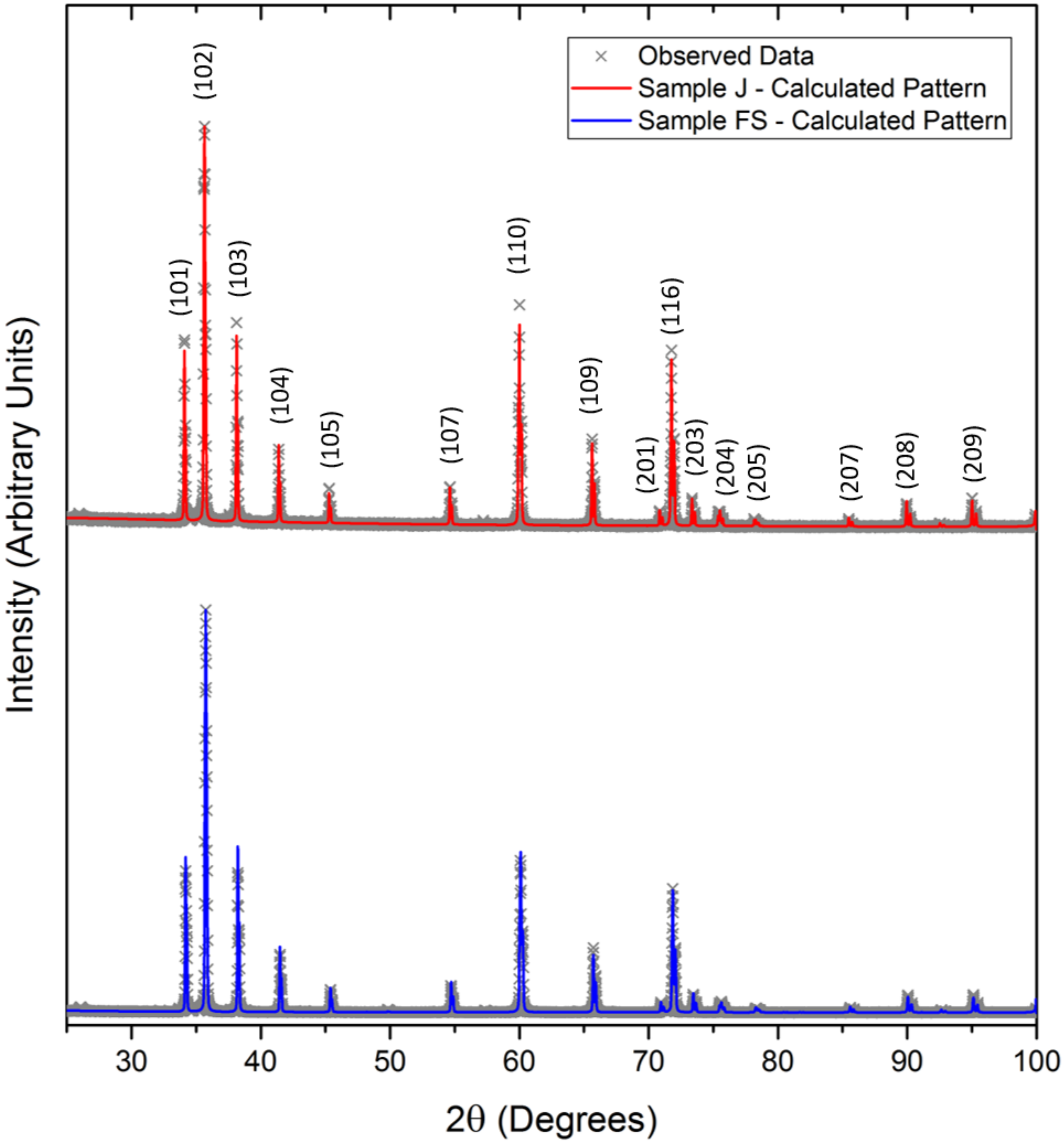

Figure 23: Experimental XRD data overlaid with Rietveld-refined fitted patterns for the SSiC samples. The planes corresponding to each major peak are labeled.

The only feature unaccounted for in the XRD patterns in Figure 23 is the low intensity doublet at $2\theta \cong 26$. This low intensity feature corresponds to the location of the highest intensity peak for graphite [41]. It is not, however, possible to complete quantitative analysis to precisely determine he fraction of graphite in the samples from XRD due to several key issues: the peak has a low intensity as a result of the low volume fraction of graphite, the graphite nodules have been observed to be small via ceramographic examination, graphite can be highly amorphous causing wide peaks, and carbon has a low mass absorption coefficient for X-rays resulting in peak displacement and broadening [41]. Based on the results presented in Figure 23, XRD confirms that the bulk of the SSiC samples is α-SiC and that the secondary constituent observed in the ceramographic examination is graphite.

5.1.2 Reaction-Bonded Silicon Carbide Samples

Two RBSiC samples were provided by AESSEAL for analysis. Cross-sectional ceramographic specimens from Samples D and FR were extracted, mounted, prepared, and analyzed using optical light and scanning electron microscopy. Figures 24 and 25 provide OLM and SEM micrographs for Samples D and FR, respectively. In the OLM micrographs, the bright phase is free silicon while the gray phase is SiC. Free silicon is lighter in bright field optical microscopy due to its higher reflectivity. In the SEM images, the darker gray constituent is free silicon, while the lighter gray constituent is SiC (confirmed by EDS). The difference in contrast between the two phases in SEM micrographs is due to the difference in electrical properties between the phases.

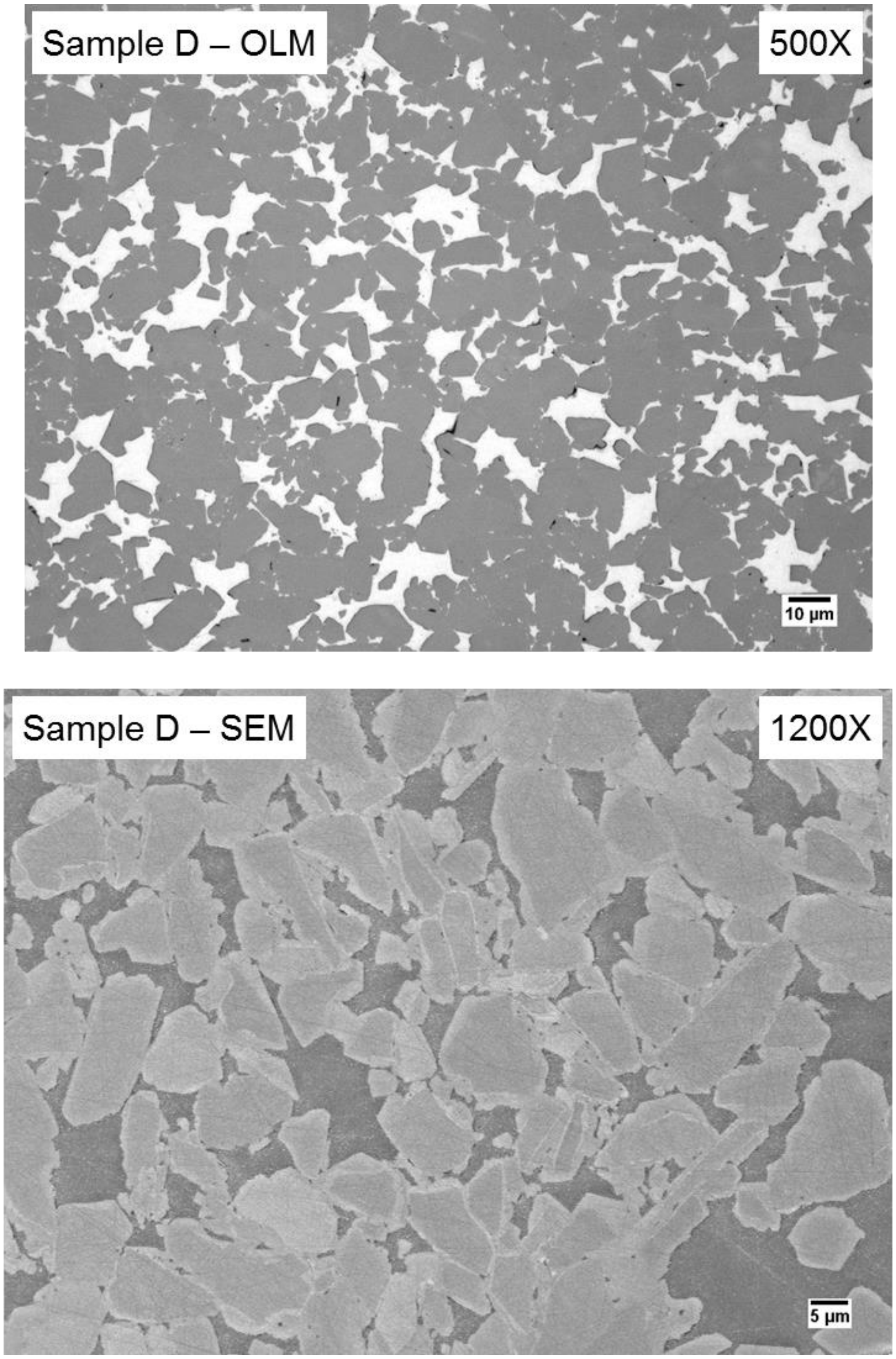

Figure 24: Optical micrograph at 500X (top) and SEM micrograph (bottom) of the as-polished Sample D ceramographic specimen. In the optical micrograph, free silicon is the reflective phase. In the SEM micrograph, SiC that formed during the reaction-bonding process outlines the SiC particles. Free silicon is present in a volume fraction of 18%.

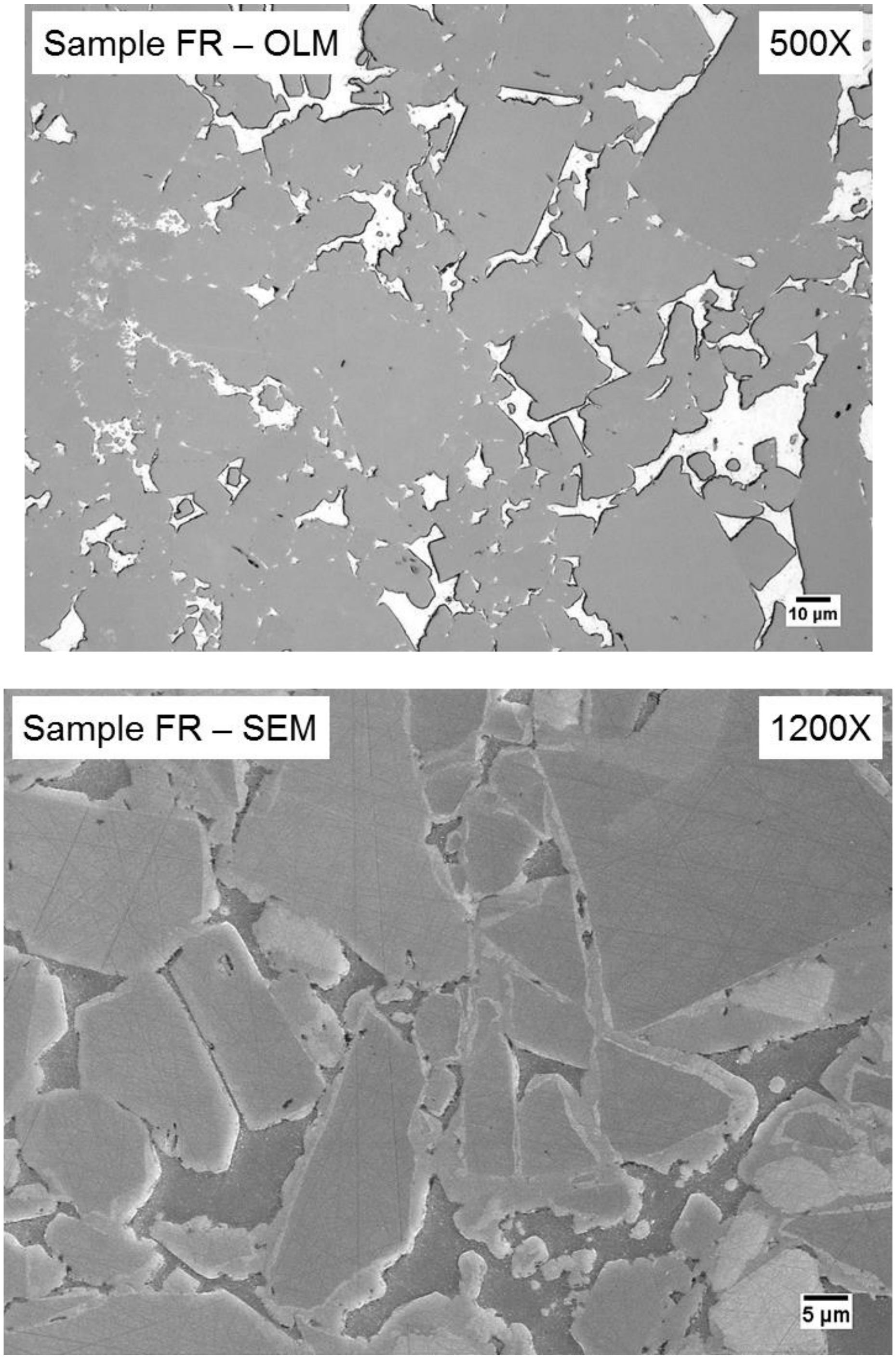

Figure 25: Optical micrographs at 500X (top) and SEM micrograph (bottom) of the as-polished Sample FR ceramographic specimen. In the optical micrograph, free silicon is the reflective phase. In the SEM micrograph, SiC that formed during the reaction-bonding process outlines the SiC particles. The free silicon volume fraction was found to be 12%.

The microstructure observed in Samples D and FR is typical of RBSiC: SiC particles surrounded by free silicon that infiltrated the porous SiC compact as a liquid. In the SEM micrographs in Figures 24 and 25, evidence of the formation of new SiC during the thermal exposure of the reaction-bonding process (T>1410 ^{o}C) is present; careful examination of the SEM micrograph reveals the presence of a brighter region surrounding SiC grains. This brighter region around the periphery of SiC grains is likely SiC that formed by the reaction of molten silicon with free carbon (carbon black or carbon from pyrolysis of the binder). This newly formed SiC served to both eliminate free carbon from the component and provide further strengthening by bonding separate SiC grains together, forming a connected network in the composite material.

A comparison of the micrographs of Sample D (Figure 24) to those of Sample FR (Figure 25), reveals obvious differences in SiC grain size and free silicon content. The SiC grain size, and thus the starting SiC particles, is larger for Sample FR than Sample D. The SiC grain size ranges from 5 to 25 μm in diameter for Sample D, while it ranges from 10 to 75 μm for Sample FR. While the difference in grain size may have an effect on the physical and mechanical properties of the RBSiC seal, the disparity in free silicon fraction will have a more profound effect on these properties (and thus seal performance). In Sample D, the fraction of free silicon was determined to be 18 vol%; however, 12% free silicon was observed in Sample FR. Optimum mechanical and physical properties are obtained with a lower amount of free silicon due to the inferior properties of silicon in comparison to SiC, specifically hardness, strength, elastic moduli, and thermal expansivity. Therefore, it is hypothesized that Sample FR has superior properties in comparison to Sample D.

To further investigate the microstructural characteristics of the RBSiC samples, XRD was conducted on specimens extracted from Samples D and FR. The XRD data and calculated pattern fitted with GSAS-II are presented in Figure 26. The XRD data was fitted using powder diffraction CIF files for the 6H polytype of α-SiC and pure silicon [40, 42]. The experimental data were accurately fitted by these polytypes, confirming the presence of α-SiC and free silicon. Furthermore, quantitative compositional information was obtained from refinement of the calculated pattern using GSAS-II. Based on the relative intensities of the SiC and silicon peaks for each of the XRD patterns an estimate of the compositions of Samples D and FR was obtained. The relative intensities of the SiC and silicon peaks qualitatively matched the compositions reported by ceramographic examination (more silicon, greater intensity silicon peaks); however, it is hypothesized that a high degree of preferred orientation existed because XRD was performed on bulk samples. Thus, error in fitting the silicon peaks was observed.

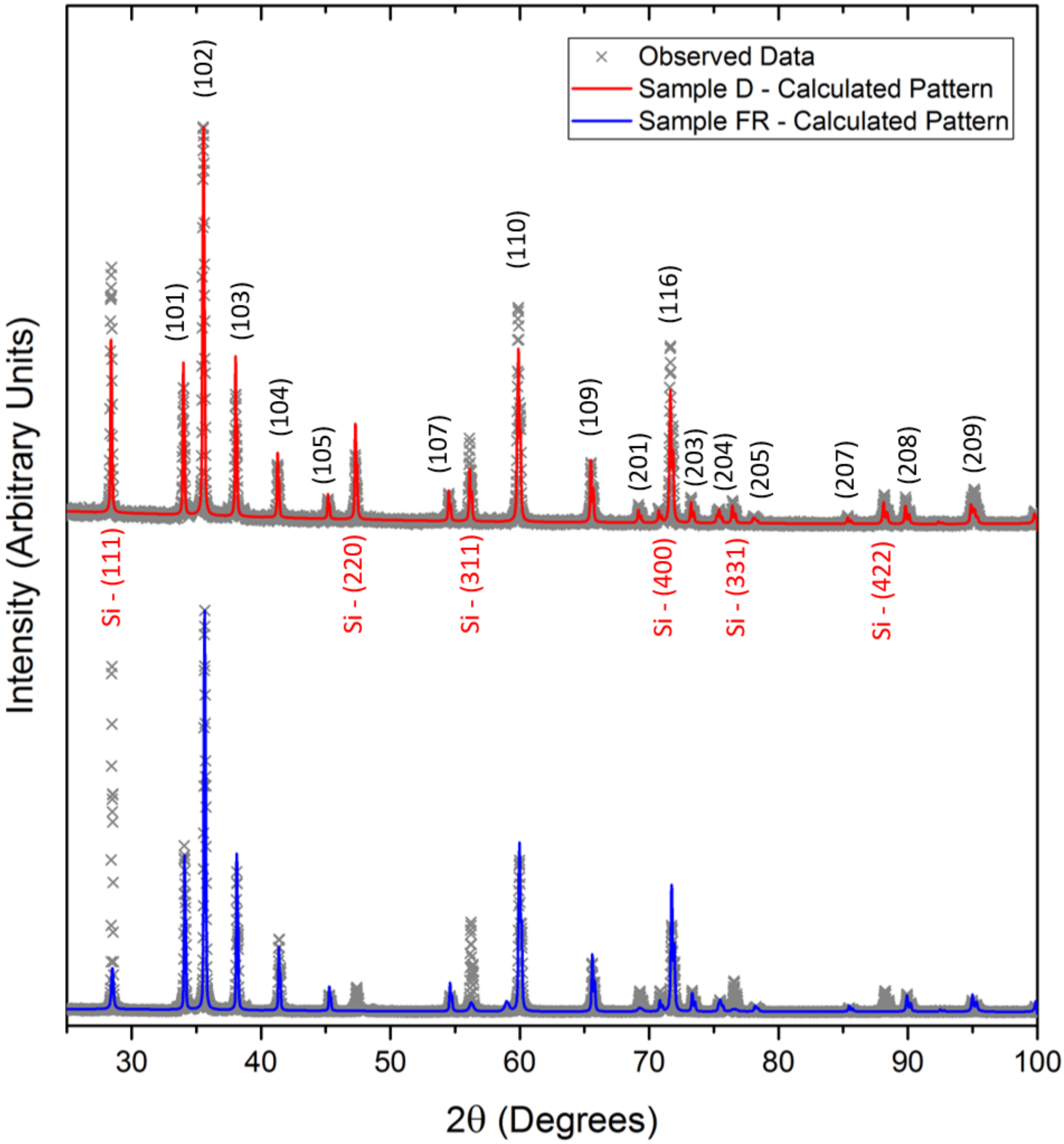

Figure 26: Experimental XRD data overlaid with Rietveld-refined fitted patterns for the RBSiC samples. The planes corresponding to each major peak are labeled (SiC: black labels; silicon: red labels).

5.1.3 Graphite-Loaded Silicon Carbide Samples

Five sets of GLSiC samples were received from AESSEAL. Their primary interest is the fraction and distribution of graphite in the SiC seal face materials, so cross-sectional ceramographic samples were prepared for Samples A, S, FG, MSG, and MRBG. Samples were analyzed using OLM and SEM. In this section, ceramographic examination results for the four GLSiC Samples that were formed by sintering (Samples A, S, FG, and MSG) are discussed first. Sample MRBG, which was formed by reaction-bonding, is discussed independently. Quantitative analysis of graphite nodules distributions is presented for all samples collectively. Finally, XRD analysis is provided for all GLSiC samples.

In the sintered GLSiC samples, graphite nodules on the order of 100 μm in a fraction of up to 20 vol% are expected based on available patents that have been discussed previously [19-20]. Therefore, properly graphite-loaded samples are presumed to have a comparable distribution of graphite nodules if the graphite-loading is to influence tribological behavior. Low magnification micrographs of Sample A are shown in Figure 27. These micrographs illustrate large graphite nodules observed in Sample A. Agglomerations of these nodules are highly isolated, and the size of the nodules is much smaller than expected. The larger nodules are present at a volume fraction of only 0.06% and only average 17 μm in diameter. Therefore, it is concluded that Sample A is not properly graphite-loaded and, thus, will have similar tribological properties to that of a SSiC seal. Also present in Sample A are native graphite nodules with an average size of 1.0 μm in a volume fraction of 7%, as shown in Figure 28.

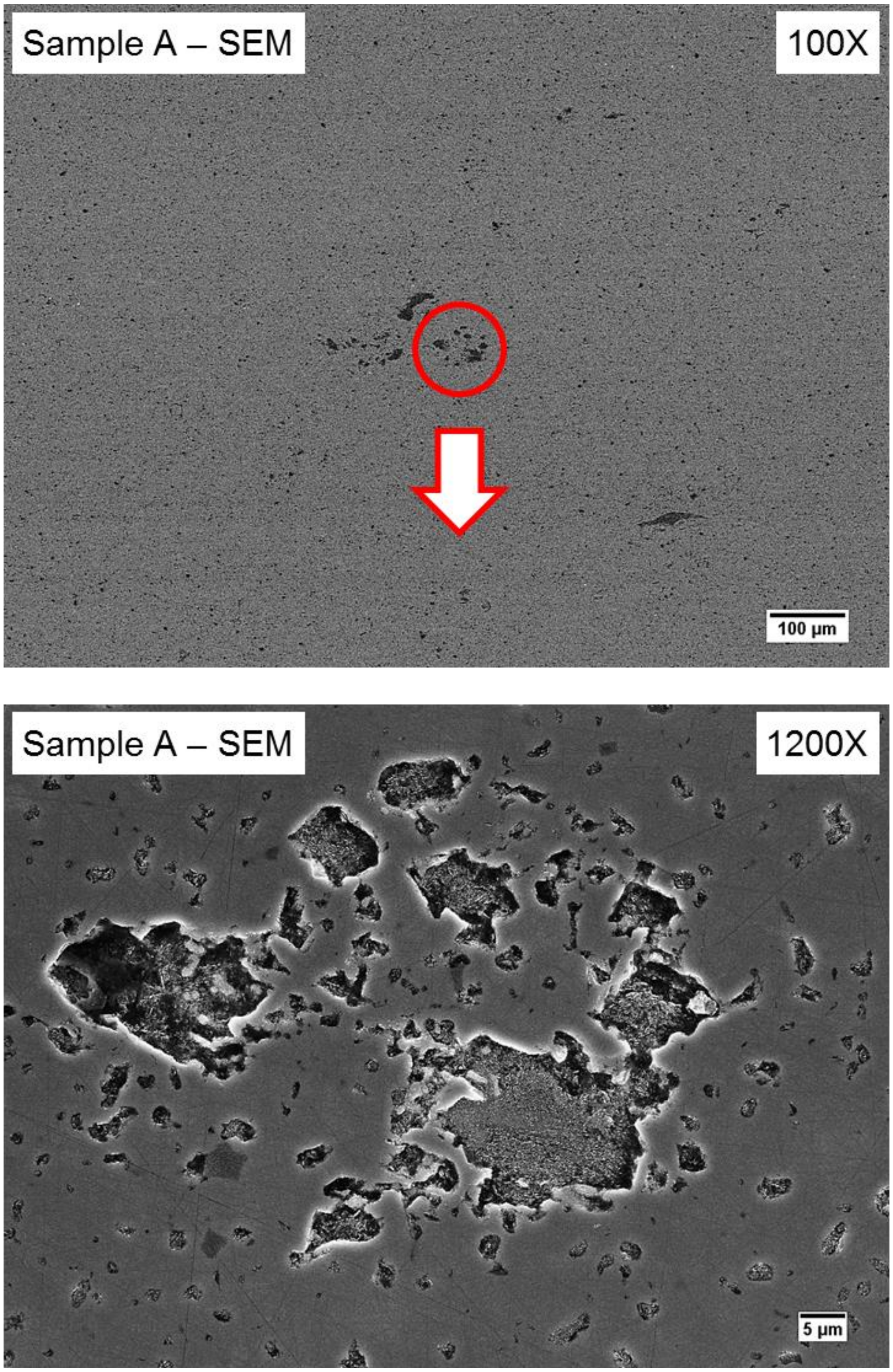

Figure 27: SEM micrographs at 100X (top) and 1200X (bottom) illustrating the controlled nodules observed in Sample A. The nodules are observed in a volume fraction of only 0.06% and are observed in localized clusters. Average nodule diameter is calculated to be 17 μm.

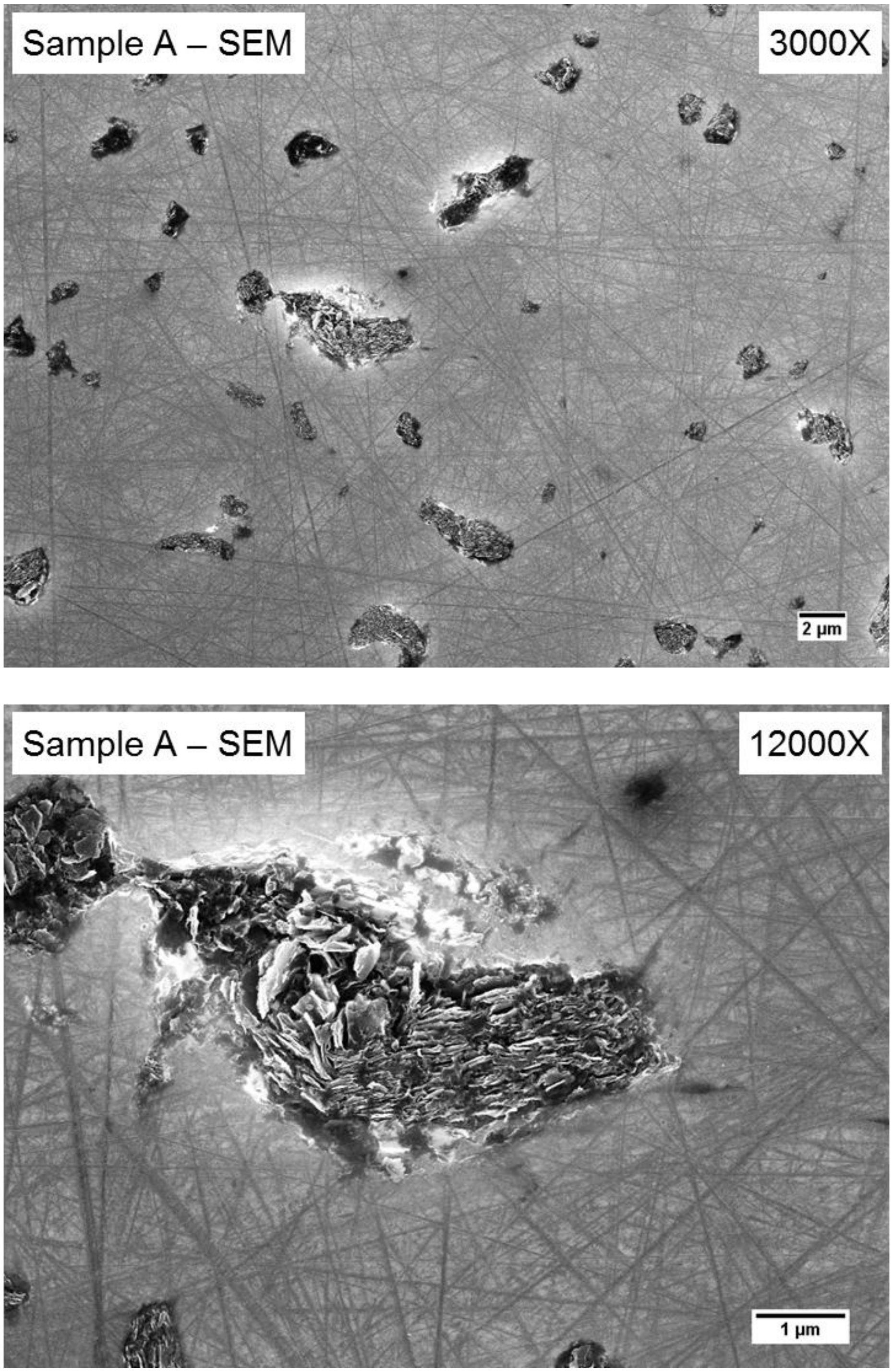

Figure 28: SEM micrographs at 3000X (top) and 12000X (bottom) illustrating surface characteristics of Ceramographic Sample A in the as-polished condition. Small graphite nodules (100 nm – 5 µm, average diameter of 1 µm) are uniformly distributed in the SiC matrix. Graphite is present in a volume fraction of 7%.

Sample S bore the characteristic graphite distribution expected in a properly graphite-loaded SiC seal, as shown by the OLM and SEM micrographs presented in Figure 29-30. The sample contains 9 vol% of large graphite nodules which have an average size of 57 µm. These nodules are intentionally introduced during the manufacturing process to influence tribological properties (after they are pulled out during the lapping process). To distinguish these nodules from native graphite, they will be termed *controlled graphite*. Interestingly, we observed that the controlled graphite nodule geometry is not spherical (in general) as one might assume for a microstructural feature that underwent a long-term, high temperature thermal exposure. Instead, the geometry of controlled graphite nodules ranges from triangular to cubic to pyramidal to elongated to disc-shaped to even nearly spherical. This results from (i) the shape of the starting carbon agglomerate, (ii) the morphology the carbon agglomerate achieves in the green compact, and (iii) how the SiC matrix densifies around the carbon agglomerate. Figure 31 illustrates the microstructural features around the periphery of the large, intact nodules on the as-lapped surface. A “reaction zone” on the order of tens of microns in thickness was observed. In this reaction zone, there were three distinct regions (from left to right in Figure 31):

1. SiC platelets protruding into the large graphite nodules
2. SiC particles and coarse graphite at the outer edge of the graphite nodule
3. SiC matrix adjacent to the nodule rich in graphite

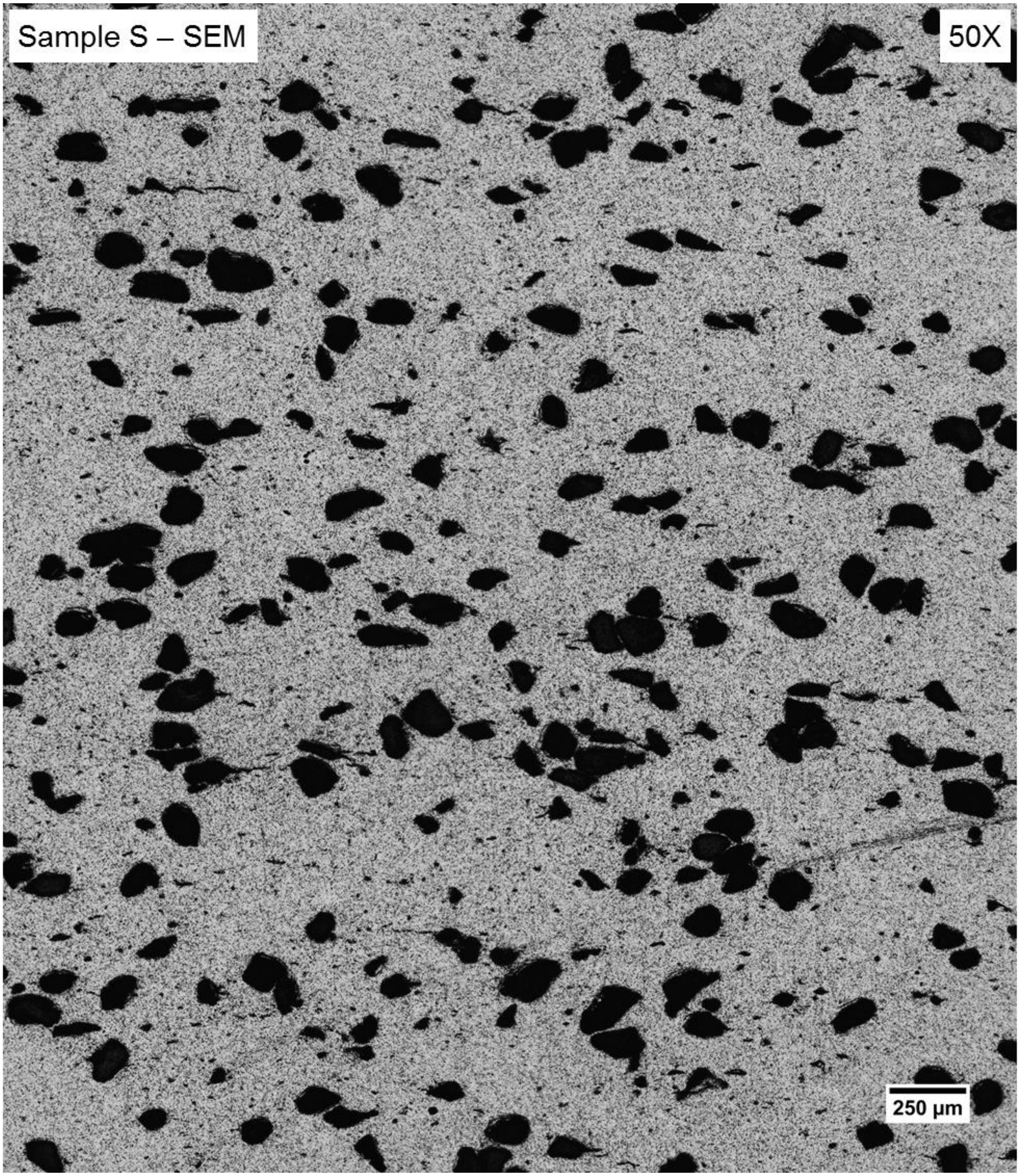

Figure 29: Optical micrograph at 50X illustrating the distribution of graphite nodules in Sample S. Controlled nodules constitute 9 vol%.

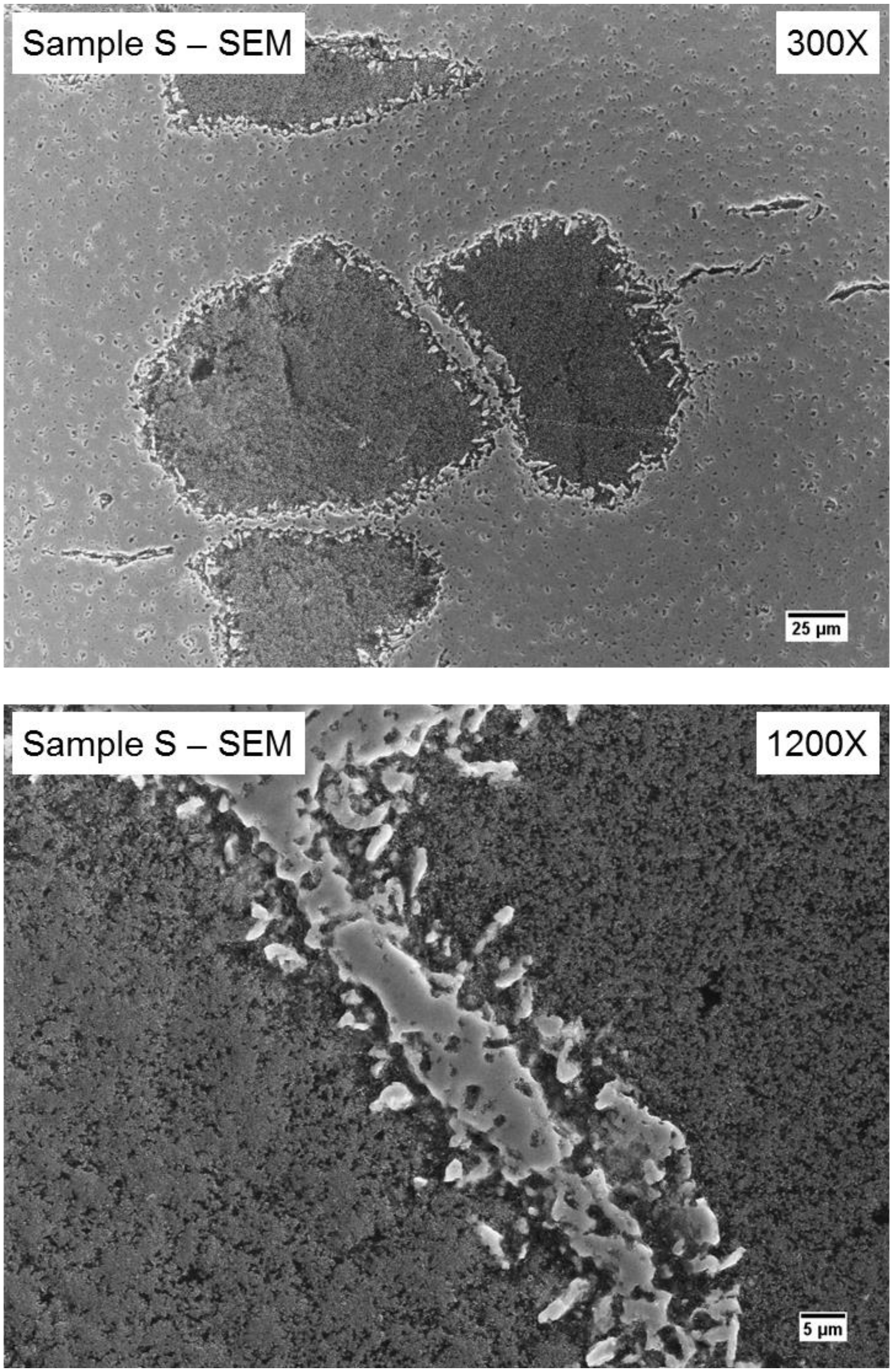

Figure 30: SEM micrographs at 300X (top) and 1200X (bottom) illustrating the morphological features of the as-polish ceramographic specimen from Sample S. Large graphite nodules (20 to 150 µm in diameter, average diameter of 57 µm) are distributed in the SiC matrix.

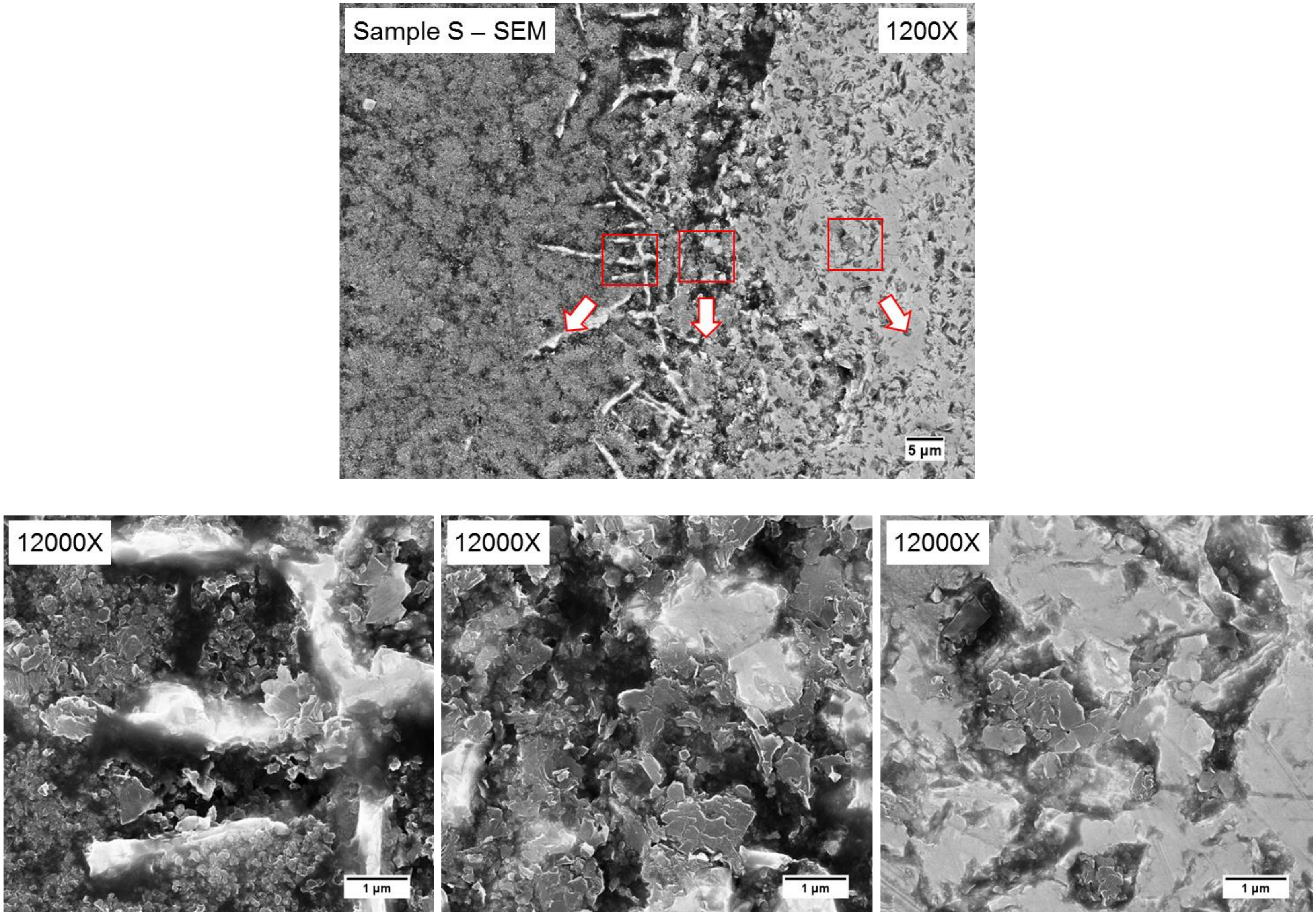

Figure 31: SEM micrographs at 1200X (top) and 12000X (bottom) illustrating the characteristics of the reaction zone at the edge of large graphite nodules. The bottom row of images was obtained at locations indicated by the red boxes in the top micrograph. Bottom row from left to right: SiC platelets in the graphite nodule, SiC particles and graphite, and graphite in the SiC matrix

This reaction zone forms during the high temperature (>2050 °C) pressureless sintering process. At this temperature, diffusive processes occur rapidly, even in a covalently bonded ceramic. It is hypothesized that silicon atoms diffused into the carbon agglomerates while carbon diffused from the large agglomerates into the surrounding SiC. Thus, the complex reaction zone illustrated in Figure 31 was formed. This reaction zone was observed in all of the GLSiC samples that were formed by sintering. Native nodules were also observed in Sample S in a volume fraction of 12% with an average diameter of 1.1 μm, which are illustrated in Figure 32. Therefore, Sample S was determined to have a total of 21 vol% graphite.

Sample FG was observed to have a microstructure that was qualitatively equivalent to that of Sample S, as illustrated by the micrographs shown in Figures 33-35. Controlled graphite is present in a volume fraction of 12% and has an average size of 58 μm; native graphite nodules have an average size of 0.8 μm. Therefore, it is concluded that the performance of Sample FG will be identical to that of Sample S.

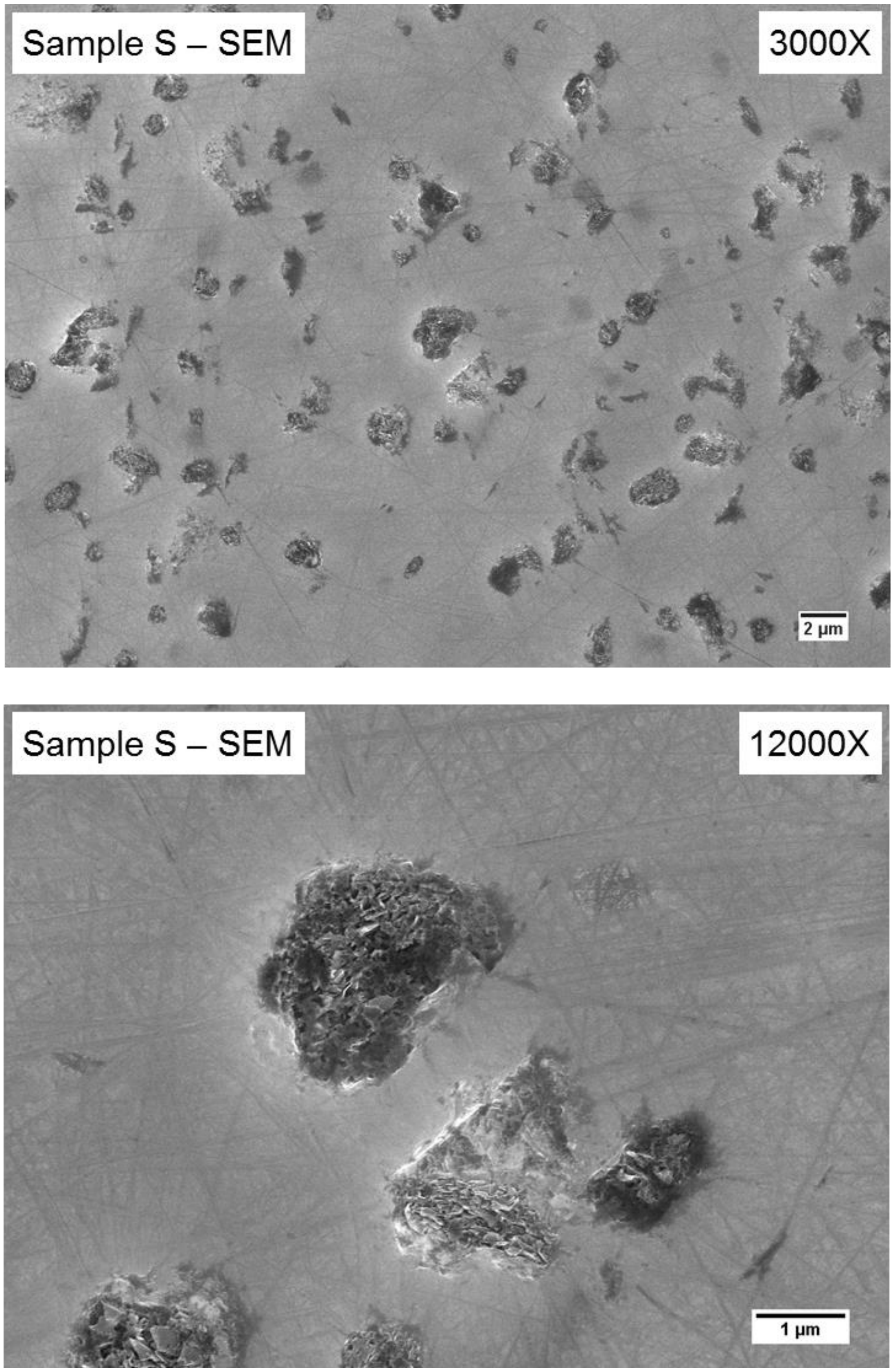

Figure 32: SEM micrographs at 3000X (top) and 12000X (bottom) illustrating small graphite nodules in the SiC matrix of the ceramographic specimen from Sample S in the as-polished condition. Small graphite nodules having a diameter of 1.1 µm are uniformly distributed throughout the SiC matrix in a volume fraction of 12%.

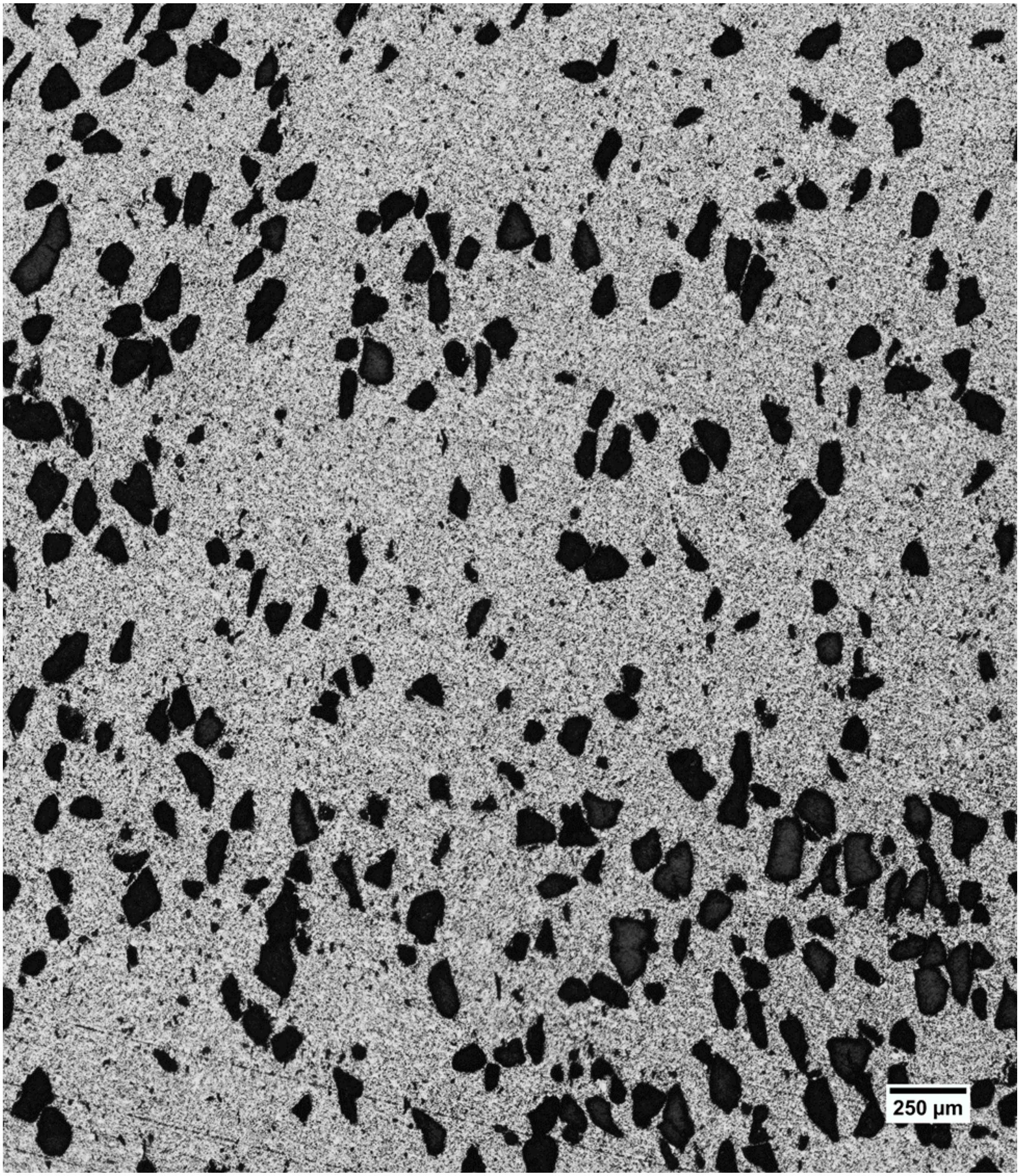

Figure 33: Optical micrograph at 50X illustrating the distribution of graphite nodules in Sample FG. Controlled nodules constitute 12 vol%.

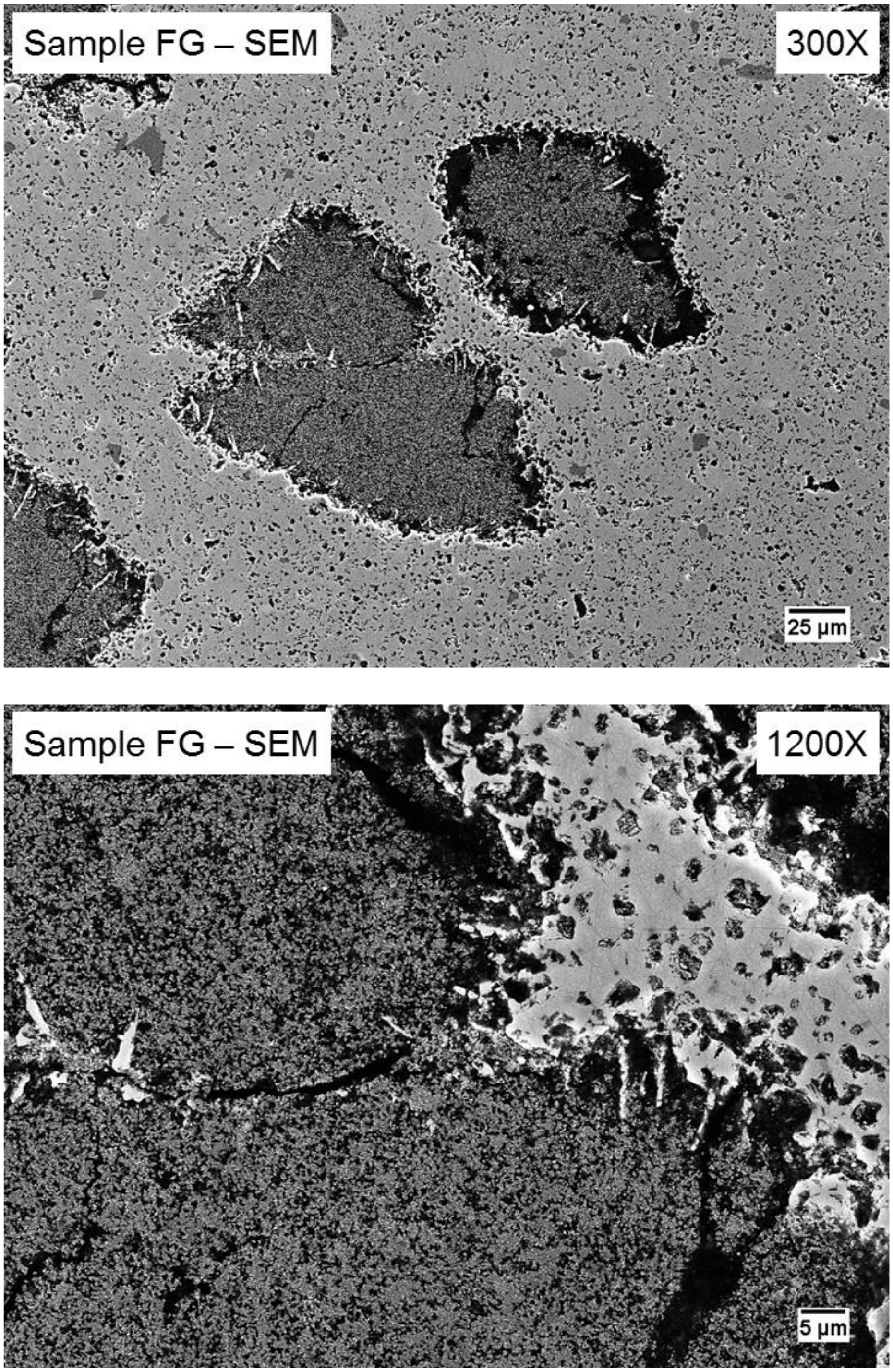

Figure 34: SEM micrographs at 300X (top) and 1200X (bottom) illustrating the morphological features of the as-polish ceramographic specimen from Sample FG. Large graphite nodules (20 to 150 µm in diameter, average size of 58 µm) are distributed in the SiC matrix.

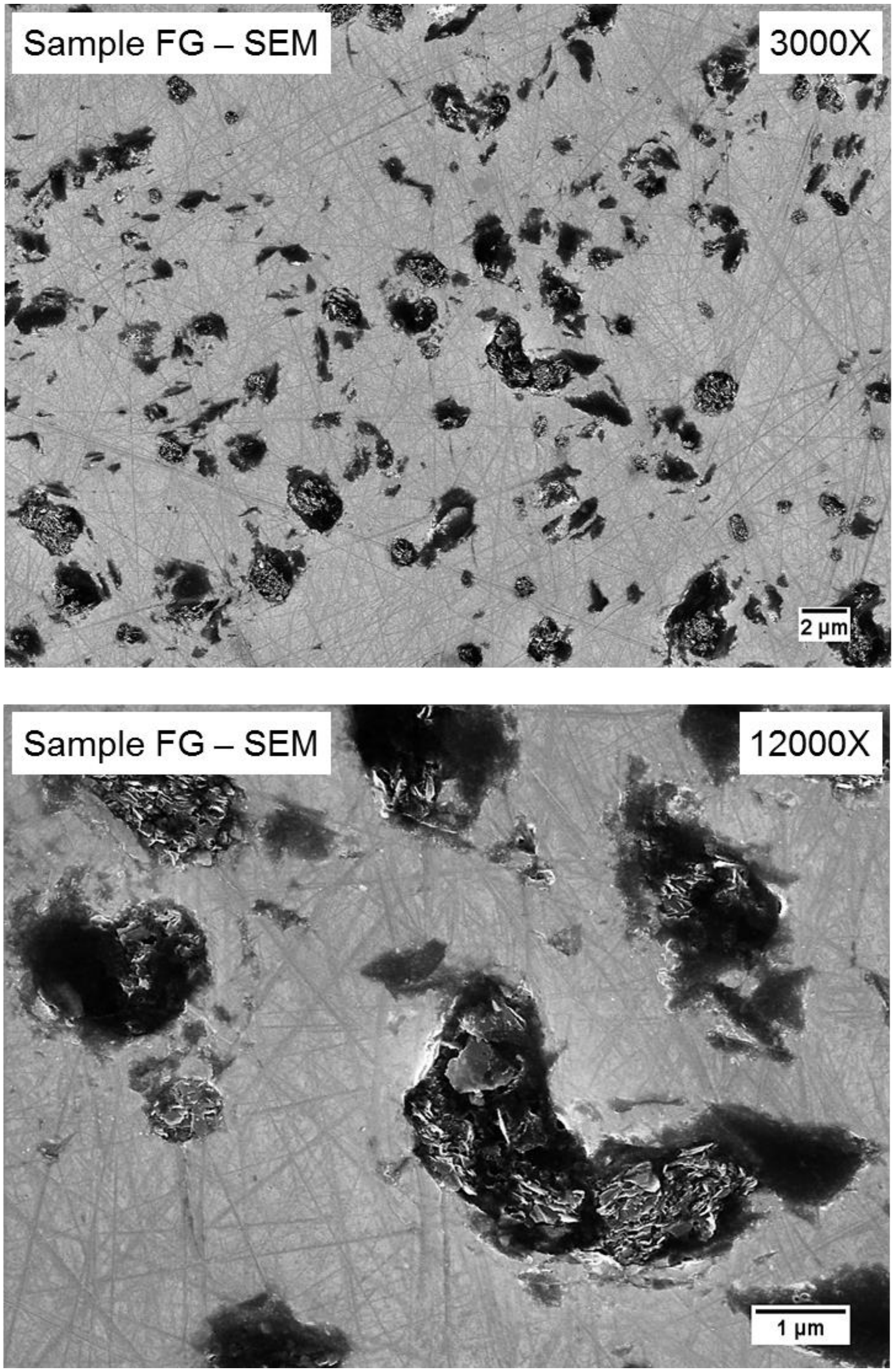

Figure 35: SEM micrographs at 3000X (top) and 12000X (bottom) illustrating small graphite nodules in the SiC matrix of the ceramographic specimen from Sample FG in the as-polished condition. Native nodules have an average diameter of 0.8 µm and are present in a volume fraction of 9%.

Sample MSG, produced by Morgan Advanced Materials, was claimed to significantly outperform other seal face materials [43]. However, there is little justification presented for this claim so it is unclear as to whether there is a scientific reason for this claim or if it is purely a simple marketing statement. Therefore, ceramographic analysis of Sample MSG (Grade PSG 100 per Morgan Advanced Materials), will elucidate whether there are microstructural features that justify this claim in comparison to the other graphite loaded samples that have been investigated. The microstructure of Sample MSG is illustrated by the micrographs shown in Figures 36-38. It is obvious that the controlled graphite nodules in this sample are, on average, smaller than those observed in Samples S and FG. The nodules are present in a volume fraction of 6% and have an average diameter of 24 μm. Native graphite nodules average 0.6 μm in diameter and account for 9 vol% of the cross-section that was analyzed. Since the distribution of the controlled graphite nodules is different from Samples S and FG, it is possible that the resulting tribological properties of Sample MSG seals are better than that of Samples S and FG. This determination cannot be made without tribological and in-service testing.

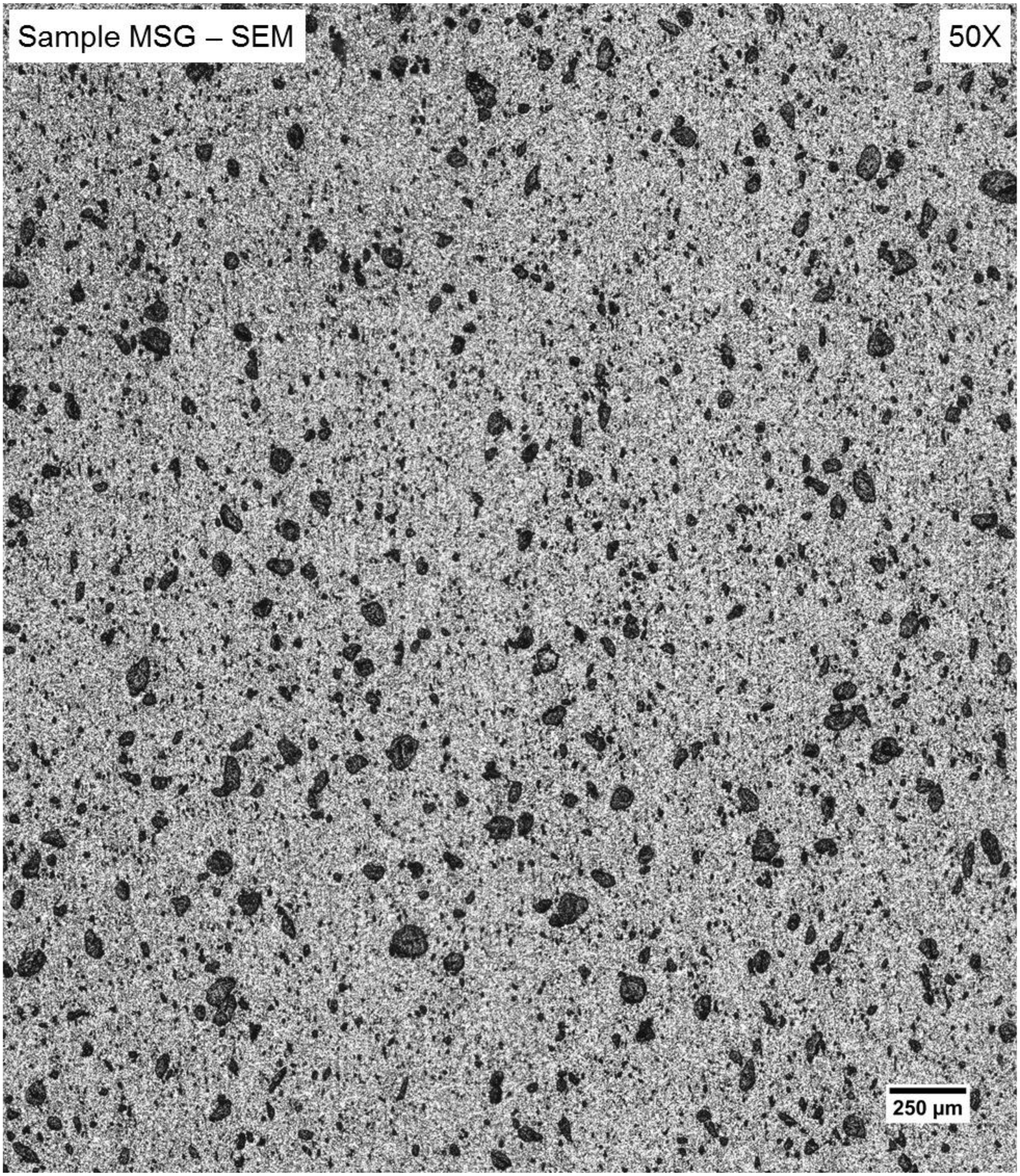

Figure 36: Optical micrograph at 50X illustrating the distribution of graphite nodules in Sample MSG. Controlled nodules constitute 6 vol%.

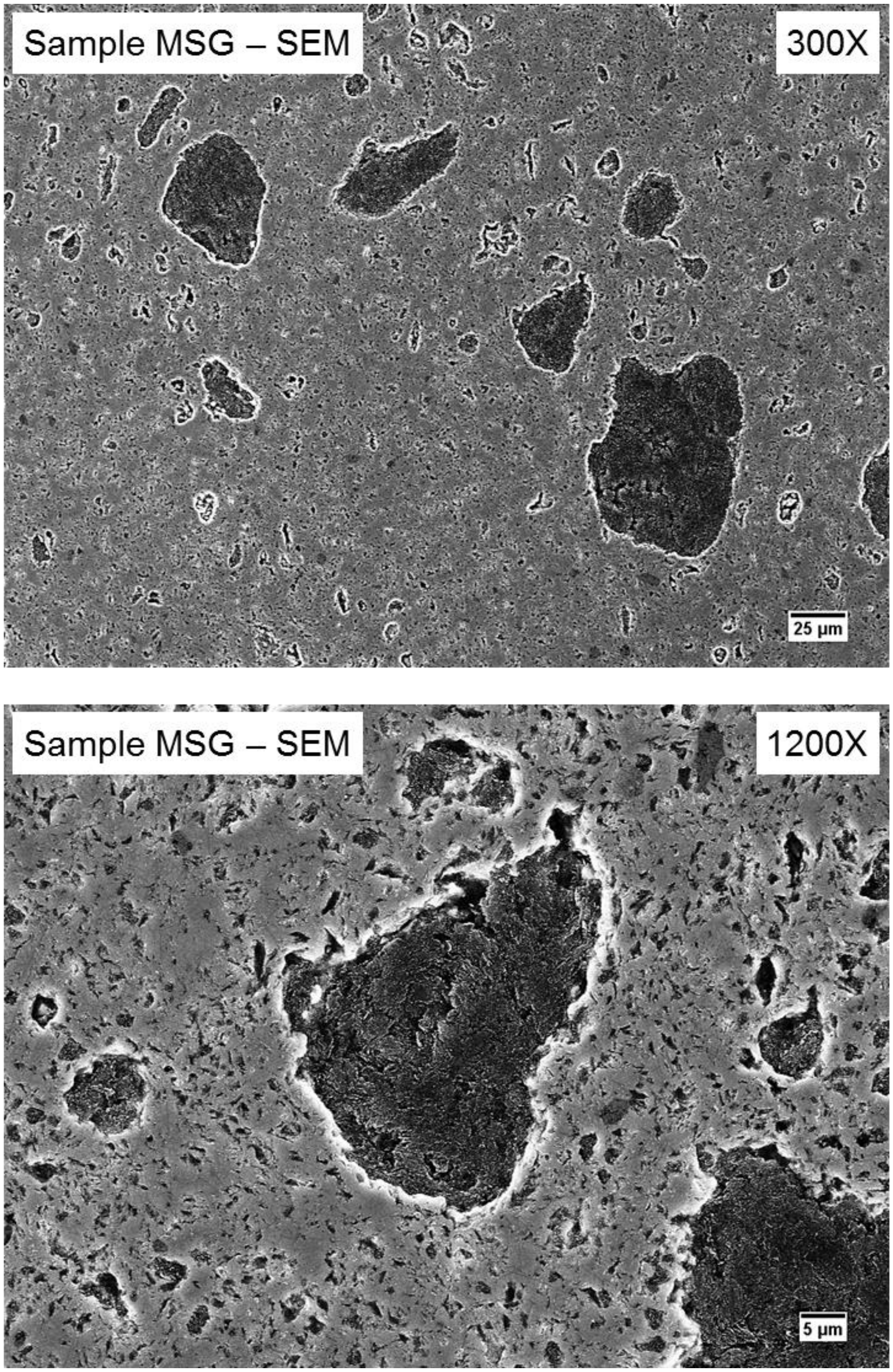

Figure 37: SEM micrographs at 300X (top) and 1200X (bottom) illustrating the morphological features of the as-polish ceramographic specimen from Sample MSG. Controlled nodules range in diameter from 15 to 75 µm, with an average diameter of 24 µm

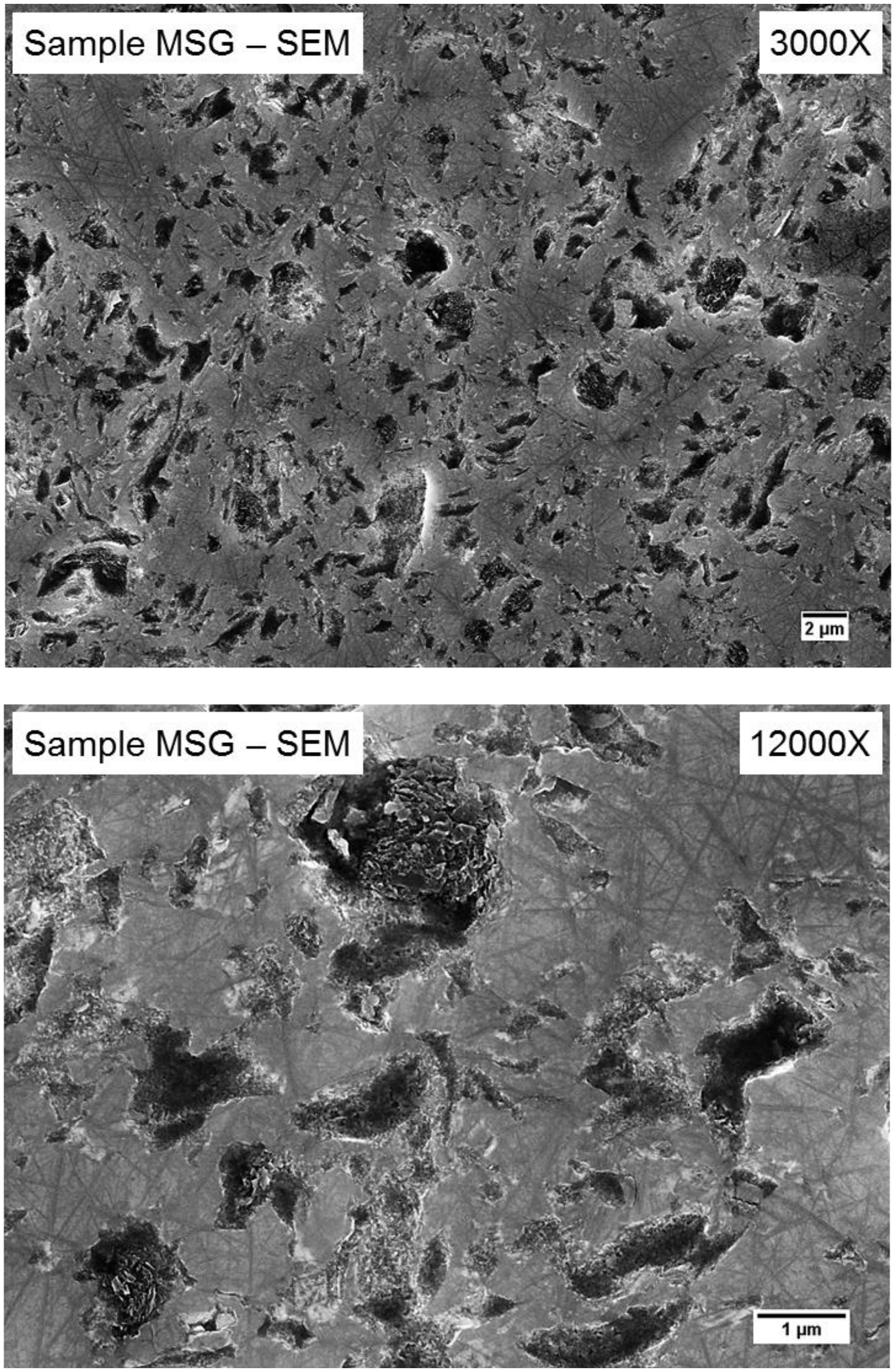

Figure 38: SEM micrographs at 3000X (top) and 12000X (bottom) illustrating small graphite nodules in the SiC matrix of the ceramographic specimen from Sample MSG in the as-polished condition. Native nodules are present in a volume fraction of 9% and have an average size of 0.6 µm.

Sample MRBG, also produced by Morgan Advanced Materials, is unique in comparison to the other GLSiC samples since it is produced by reaction-bonding rather than sintering. Figures 39-41 illustrate the microstructural characteristics of Sample MRBG. Figure 39 displays the diverse microstructure of Sample MRGB, consisting of 16 vol% controlled graphite and 20 vol% free silicon. The controlled graphite nodules have an average size of 50 μm. The OLM and SEM micrographs shown in Figure 40 clearly show the constituents present in Sample MRGB. Further, these micrographs provide insight into the reactions that occur during the reaction-bonding process (temperatures greater than 1410 °C). It is obvious that the liquid silicon reacts with the graphite agglomerates during the reaction-bonding thermal exposure, as graphite nodules are surrounded by SiC grains. This results in the jagged graphite-SiC boundary that will likely influence nodule pull-out and the resulting tribological properties. As seen in Figure 41, the sharp boundaries around SiC grains and the absence of a boundary in those grains that would indicate new SiC formation around already-present SiC suggest that the green compact consisted of only carbon prior to infiltration with liquid silicon. The average SiC grain size is between 5 and 25 μm.

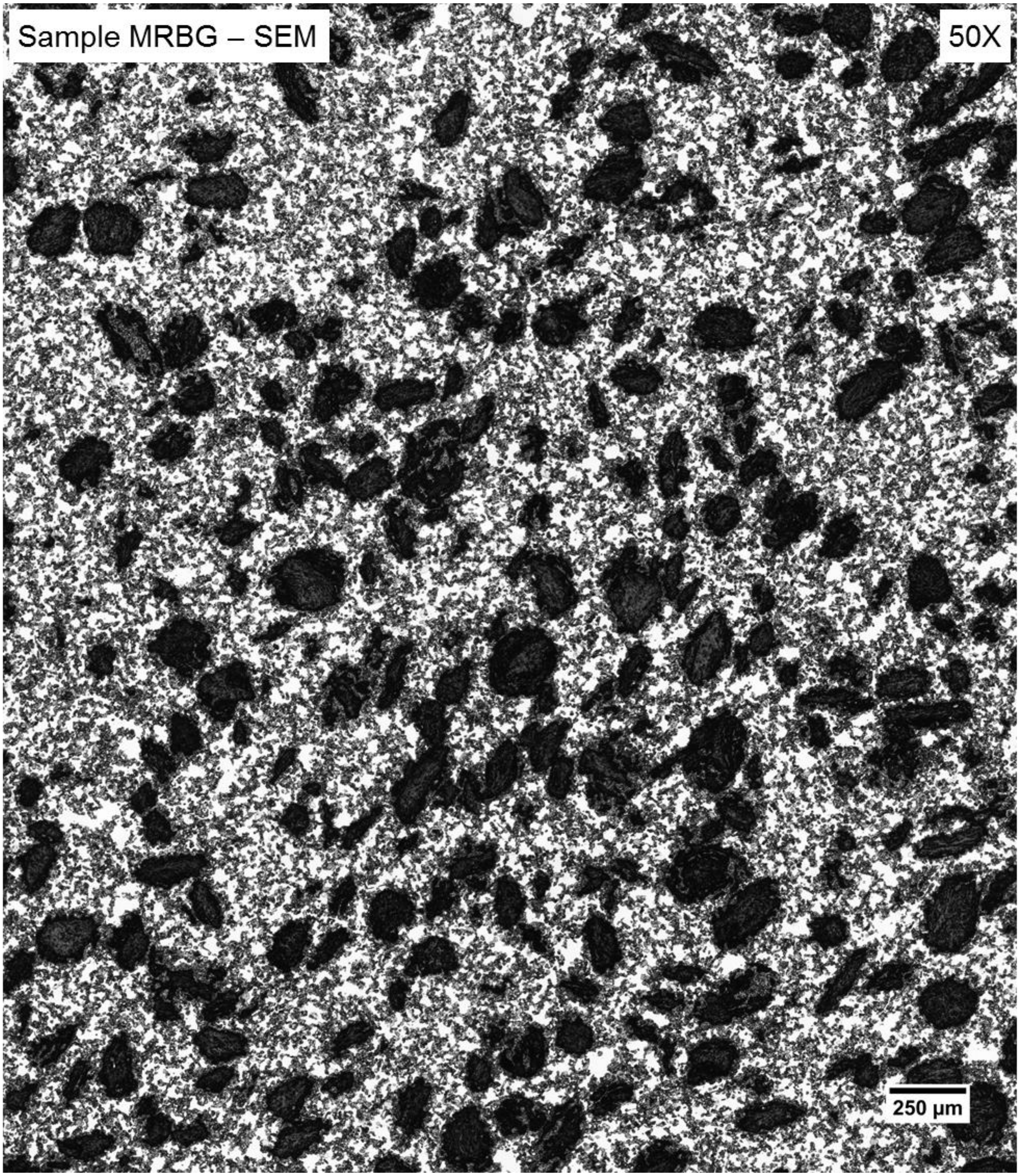

Figure 39: Optical micrograph at 50X illustrating the distribution of graphite nodules in Sample MRBG. Controlled nodules constitute 16 vol%.

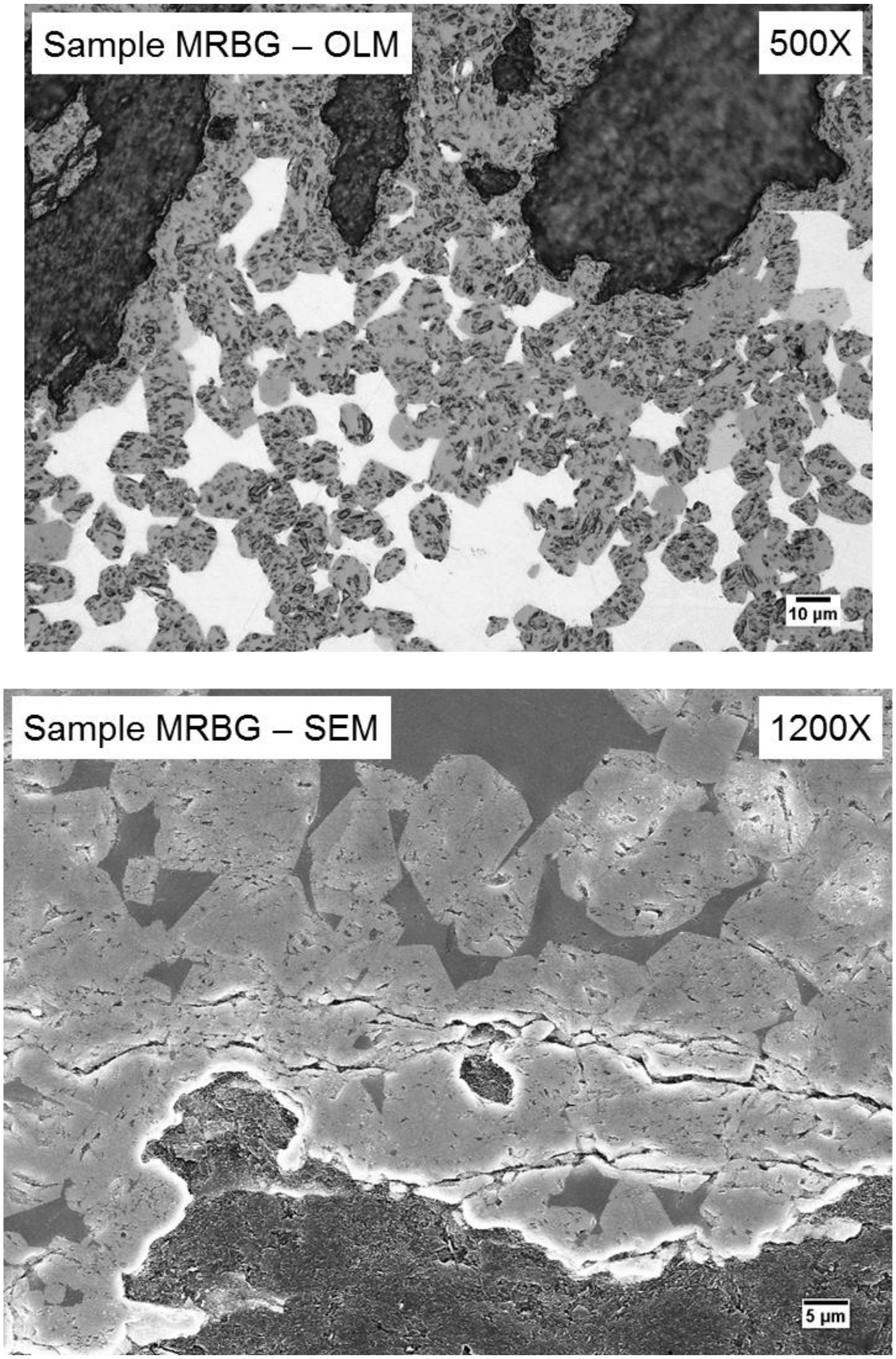

Figure 40: Optical micrographs at 500X (top) and SEM micrograph of the as-polished Sample MRBG ceramographic specimen. In the optical micrograph, free silicon is the reflective phase. In the SEM micrograph, free silicon is the darker gray phase. SiC particles with sharp edges are present around the periphery of the controlled graphite nodules in the micrographs.

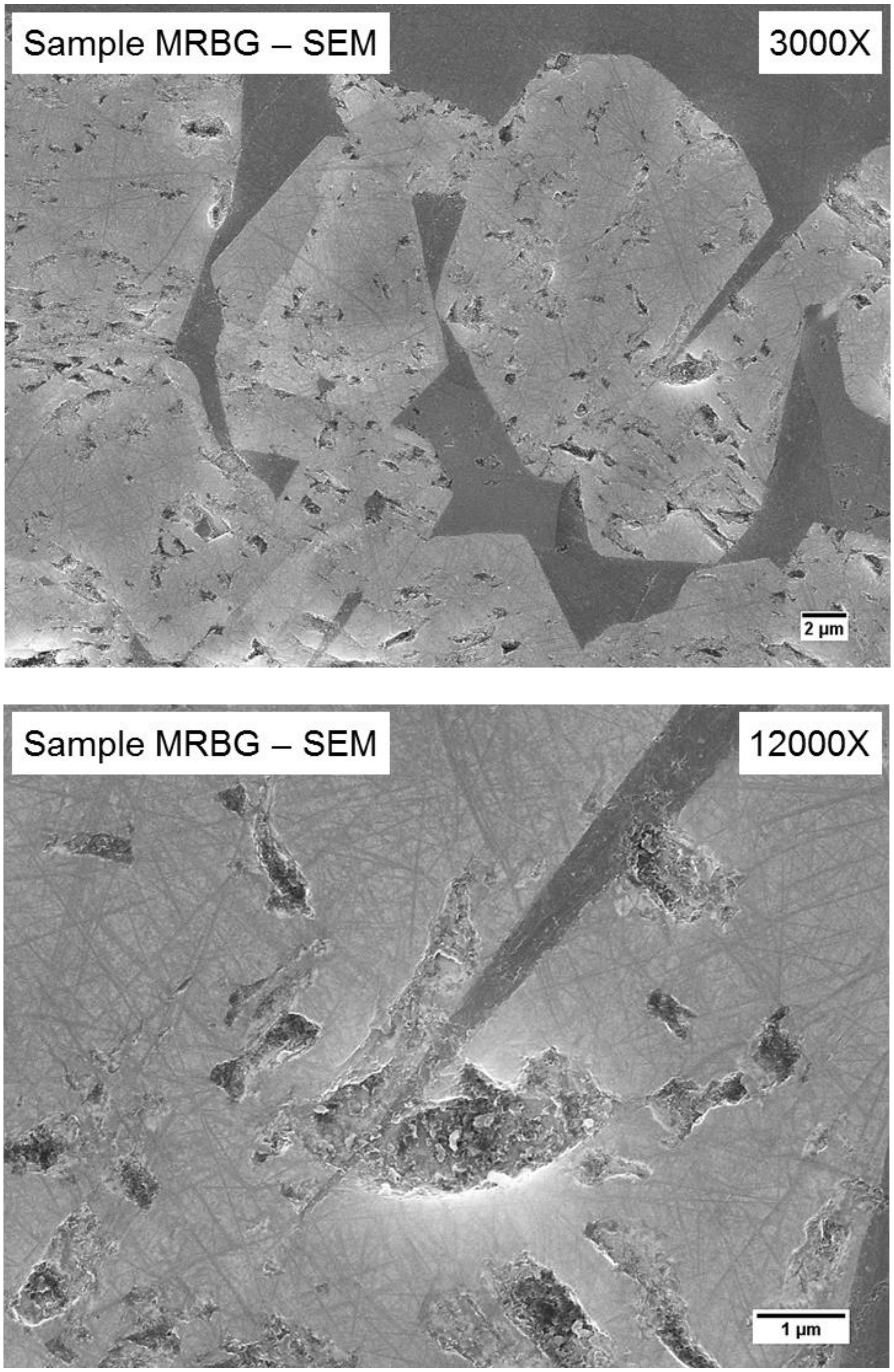

Figure 41: SEM micrographs at 3000X (top) and 12000X (bottom) illustrating small graphite nodules in the SiC matrix of the ceramographic specimen from Sample MRBG in the as-polished condition. In the high magnification micrograph, the sharp SiC boundaries and native graphite nodules are shown.

ImageJ Automated Image Analysis Software was employed to determine the distributions of native and controlled graphite in each of the GLSiC samples. Native nodules were analyzed using 2500X QBSD SEM micrographs that encompassed an area of more than 10000 μm^2, and the controlled nodules were analyzed using 40X QBSD SEM micrographs that included approximately 10 mm^2 (10,000,000 μm^2). It should also be noted that the cutoff diameter to be classified as a controlled nodule was 12 µm. Figure 42 provides a comparison of graphite distributions for the GLSiC samples as a double logarithmic histogram plot of areal density of nodules versus nodule diameter. It should be noted that the areal density of each bin was on the order 1000 mm^{-2} for the native graphite nodules, while the areal density for the controlled nodules for each bin was between 0.1 and 10 mm^{-2}. Therefore, the areal of native nodules is higher than that of controlled nodules. Further, differences in controlled graphite nodule distribution that were previously discussed in a qualitative manner are now presented in a quantitative context. Sample A is confirmed to be an improperly graphite-loaded SiC seal when compared to the other GLSiC samples. The controlled graphite nodule distributions of Samples S, FG, and MRBG were highly similar. Sample MSG, which was claimed to have improved performance by Morgan Advanced Materials, had a controlled nodule distribution that was skewed to the left in comparison to Samples S, FG, and MRBG. Therefore, it is possible that the distribution of graphite nodules observed in Sample MSG provides optimum tribological property improvements for GLSiC.

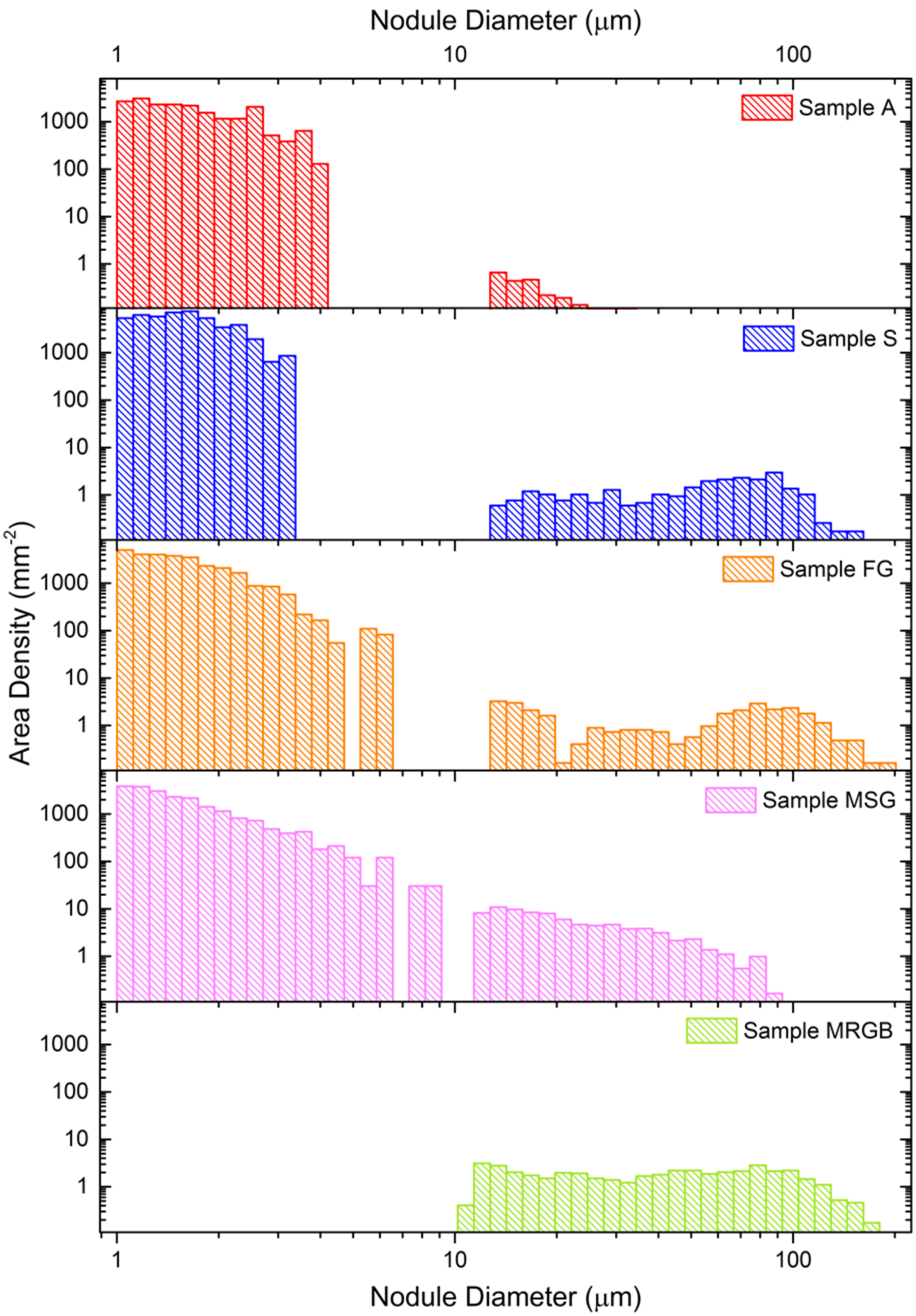

Figure 42: Plots of the density of native and controlled graphite nodules versus nodule diameter for the GLSiC Samples A, S, FG, MSG, and MRBG. The volume fractions of native nodules and their average sizes are provided in the plots. Note: Native nodules in Sample MRBG were not quantified.

To further investigate the constituents present in the GLSiC samples, XRD was performed on a specimen extracted from each of the GLSiC seal sets. The XRD data and fitted patterns are shown in Figure 43 for Samples A, S, FG, MSG, and MRBG. XRD results confirm the previously discussed phase distributions observed in ceramographic analysis. The intensity of the carbon doublet reflects the volume fraction of graphite present in each sample. The XRD pattern for Sample MRBG shows strong graphite and silicon peaks, which agrees with microstructural analysis (16 vol% graphite and 20 vol% silicon).

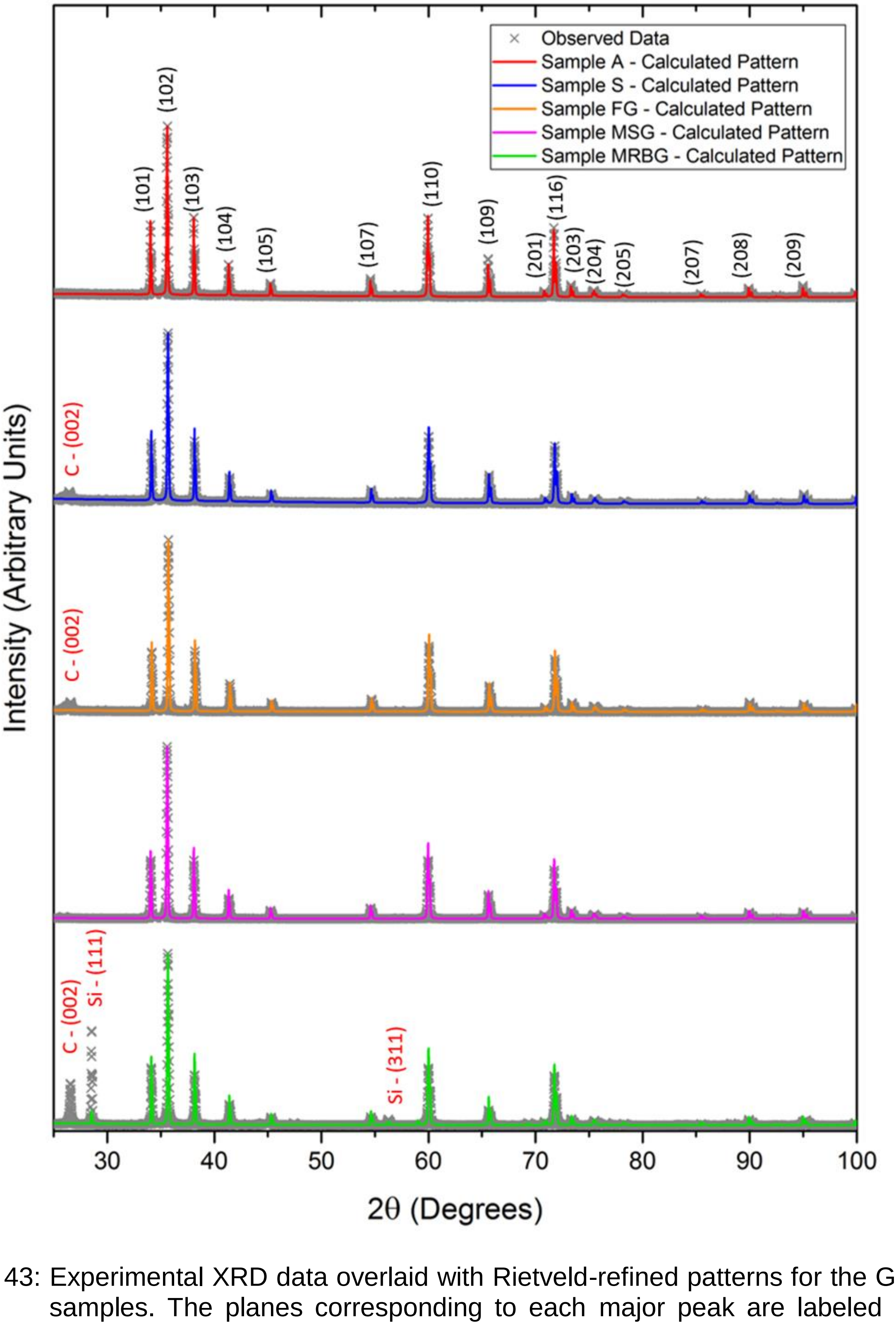

Figure 43: Experimental XRD data overlaid with Rietveld-refined patterns for the GLSiC samples. The planes corresponding to each major peak are labeled (SiC: black labels; graphite and silicon: red labels).

5.1.4 Analysis of As-Lapped Graphite-Loaded Mechanical Seals

It was mentioned in the *Tribological Considerations for Mechanical Seals (Section 3.4)* that controlled surface features (pores) have been fabricated on seal faces to improve tribological behavior. Graphite agglomerates in GLSiC are intended to be exposed to the surface upon wearing down (or lapping) of the seal face and pulled out to leave behind controlled surface porosity. The effectiveness of graphite in GLSiC is therefore highly dependent on how efficiently the agglomerates are extracted by the lapping procedure of mechanical seals. In order to quantify this efficiency, the as-lapped surface of Sample S (a GLSiC seal) has been analyzed to determine the extent of remaining graphite phase. Figure 44 displays a characteristic pore that remains after pull-out of the parent graphite nodule with a surface heat map to demonstrate depth. The size, geometry, and distribution of pores on the seal surface will be defined by the size, geometry, and distribution of parent graphite nodules in the matrix prior to lapping. The geometries of graphite nodules (and their resulting pores) are not consistently spherical, but range from triangular, cubic, pyramidal, or elongated, to disc-shaped and semi-spherical. Thus, the controlled surface porosity will not be as homogenous as the deterministic patterns produced by etching.

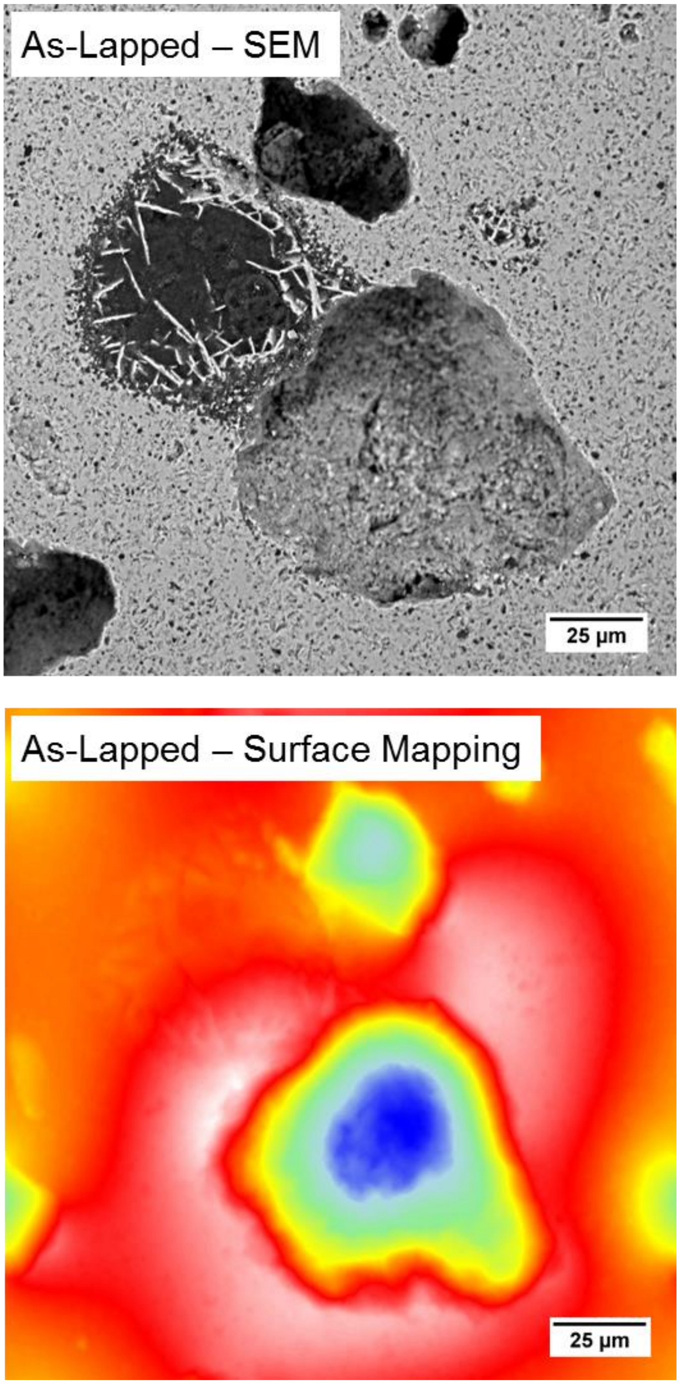

Figure 44: SEM micrograph and associated heat map displaying an intact nodule and several pulled-out nodules on the as-lapped surface of Sample S.

To determine the effectiveness of graphite nodule pull-out, SEM images were taken of the as-lapped surface of Sample S for analysis in ImageJ Automated Image Analysis Software [34]. ImageJ utilizes differences in contrast to isolate separate phases for size and volume percent analysis; in this case, the darker graphite phase will contrast with the lighter SiC matrix in SEM images obtained with a backscatter detector (enhanced Z contrast). The SEM micrograph of the as-lapped surface is shown in Figure 45. This image shows a considerable number of controlled graphite nodules remaining in the matrix after the lapping procedure performed by AESSEAL. To understand potential factors in pull-out effectiveness, we have generated distributions of produced pores separately from distributions for remaining graphite. Due to ImageJ limitations, the phases of interest required manual selection with a pure black fill to isolate object distributions; this process is illustrated in Figure 45 with remaining graphite highlighted in blue and pores in red.

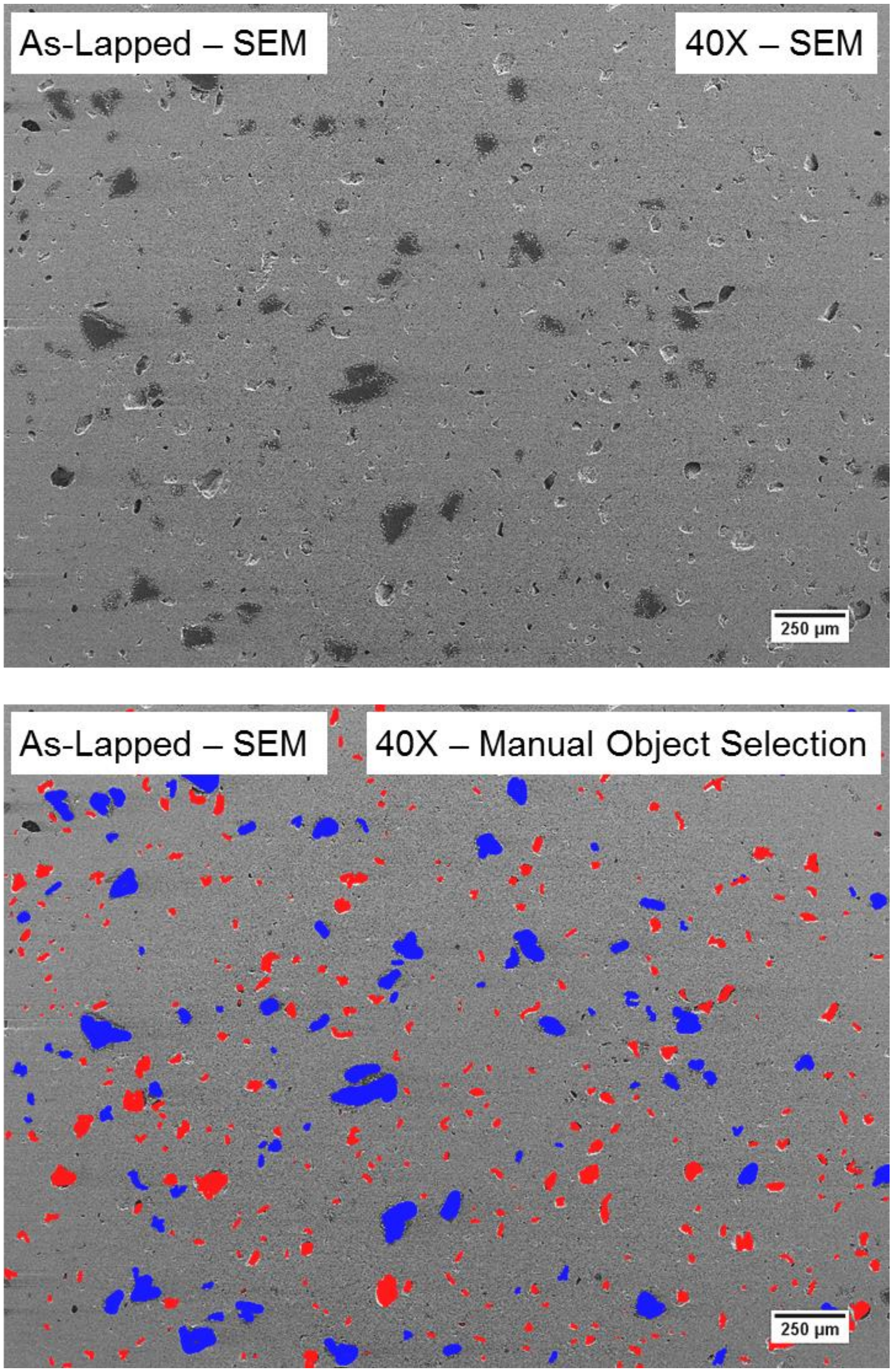

Figure 45: Demonstration of the manual object selection method in preparation for ImageJ analysis. Remaining graphite is highlighted in blue; pores resulting from the pulling out of graphite nodules during lapping are highlighted in red.

The distributions for pulled out nodules (red) and intact nodules (blue) are plotted in Figure 46. The plot presents the fraction of total nodules that were effectively pulled out or intact for a given nodule diameter. Presented in this way, the effectiveness of the lapping procedure to pull out graphite nodules is a function of particle diameter. In other words, comparatively small graphite nodules (10 to 50 μm in diameter) are highly likely to be pulled out during the lapping procedure while comparatively large graphite nodules (80 to 150 μm in diameter) are unlikely to be pulled out. Nodules in the size range of 25 to 80 μm in diameter were found in both the pulled out and intact condition. These results

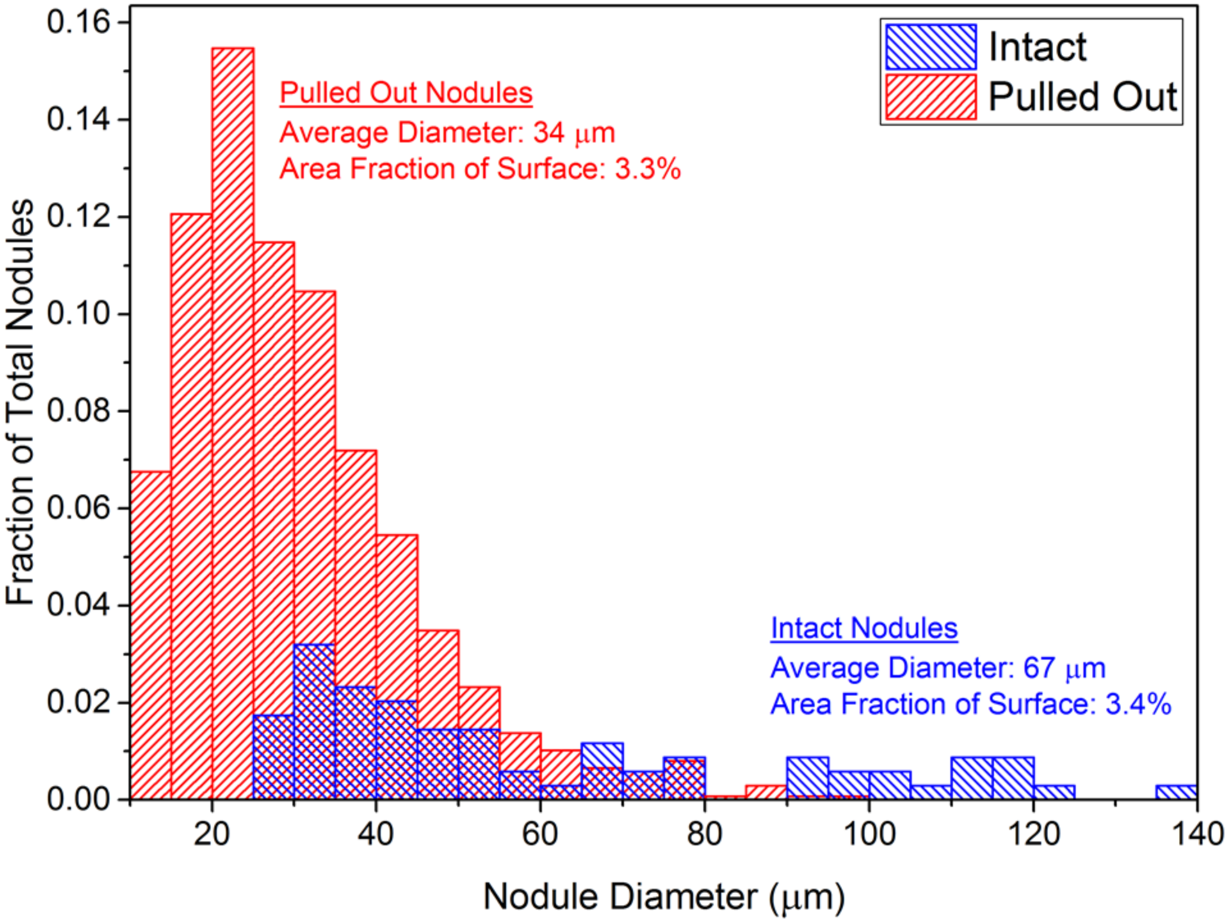

Figure 46: A histogram presenting the fractions of pores resulting from graphite pull out versus intact graphite particles for a given nodule diameter in Sample S. No pores larger than 100 μm or smaller than 30 μm were observed.

are unique to the lapping procedure time and grit selected for Sample S; it is likely that alterations in the lapping procedure will have an effect on pull-out efficiency. Graphite nodules that remain in the surface are detrimental to the seal material's mechanical properties without an offsetting tribological benefit. Figure 46 shows that only 3.3% of the surface area has distinct porosity that averages 34 μm in diameter while 3.4% of the surface is populated by intact nodules that average 67 μm.

The analysis of the as-lapped surface indicates that the ideal graphite nodule size is less than 80 μm for the current lapping procedure. To determine the quality of GLSiC one must compare their graphite nodule size distributions (provided in Figure. 42). Of these mechanical seals, Sample A possessed minimal controlled graphite and would not show a considerable tribological improvement over a sintered sample. Samples S, FG, and MRBG showed similar distributions of graphite nodules, with several nodules above 80 μm. These large nodules are less likely to be removed from the surface, as determined previously. Sample MSG shows an ideal distribution of graphite nodules, with minimal agglomerates above 80 μm. The sample with a distribution most similar to Sample MSG's is Sample S from an alternative supplier. An SEM micrograph and surface heat map in Figure 47 shows that these native nodules are effectively pulled out by lapping due to their small size. The pores left behind by pulled out native nodules will be on the order of 1 μm. Due to this, they will only be able to store minimal lubricant but are dispersed more homogeneously throughout the matrix. These native nodules will likely be effective at re-supplying lubricant in the case of local boundary lubrication, but controlled nodules will be more effective at trapping debris and generating hydrodynamic lift. For this reason, it is important to predominantly assess the distribution of controlled graphite nodules when selecting a GLSiC supplier.

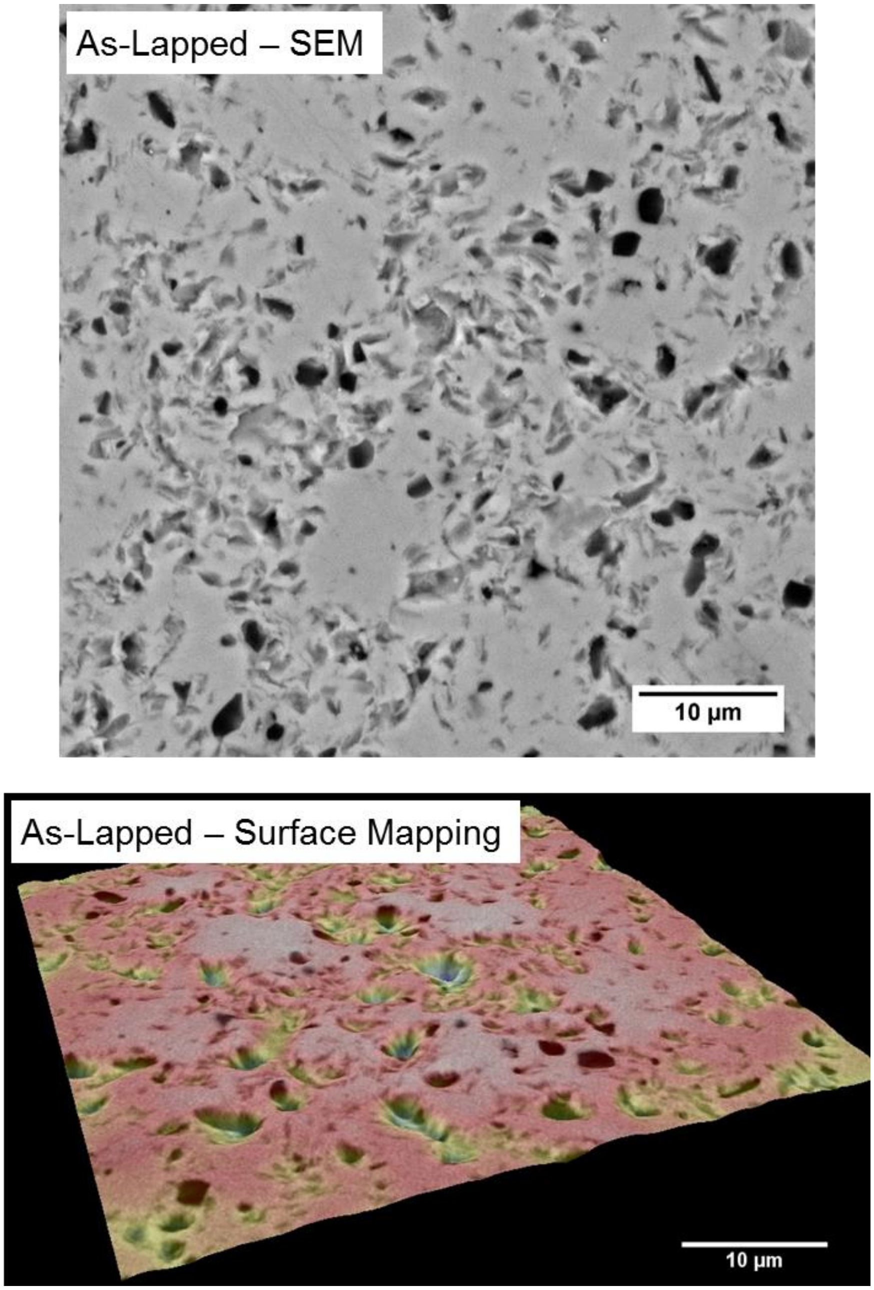

Figure 47: SEM micrograph and corresponding topographical surface reconstruction illustrating surface characteristics associated with native graphite in sintered samples (SSiC and GLSiC) in the as-lapped condition. Surface features range in depth from 1 to 3 µm.

5.2 PHYSICAL PROPERTY EVALUATION

The determination of the physical properties (density and elastic modulus) of each set of SiC mechanical seals was undertaken to supplement the microstructural understanding that was obtained through ceramography and XRD. Density determination through water pycnometry, utilizing the Archimedes Method, will depend on the microstructural constituents present and their volume fraction in each set of seals. *Section 5.2.1* will relate density to microstructure, a property easily determined by nondestructive means. It will be shown that density determination provides an informed guess of the fraction of constituents present. Presented in *Section 5.2.2* is elastic moduli determination through RUS, which will provide an additional evaluation for four sets of the SiC mechanical seals (Samples A, D, J, and S).

5.2.1 Density

The density of each set of SiC mechanical seals provides information about two primary material properties: percent densification and fractions of phases present. In ceramics, the degree of densification is a sign of material quality for structural parts, with densities close to the theoretical density corresponding to low pore volume and correlating to significant increases in mechanical and physical properties. Additionally, secondary phases will affect the density of the SiC mechanical seals and provide information regarding the presence of secondary phases. The density of a two-phase material may be related by the simple rule of mixtures. In the case of the addition of either silicon or graphite, a decrease in density is observed for SiC, as shown by the expected density ranges presented in Figure 48, which were obtained using the CES Materials Selector software [10]. Density is a good indicator of the amount of a secondary phase, however, it is not sufficient for precise quantitative determination due to the interdependence of both secondary phases and pore volume on measured density of SiC parts. Given that microstructural analysis shows that provided SiC mechanical seals have no detectable porosity, phase fractions estimates should be comparable to the results of other methods.

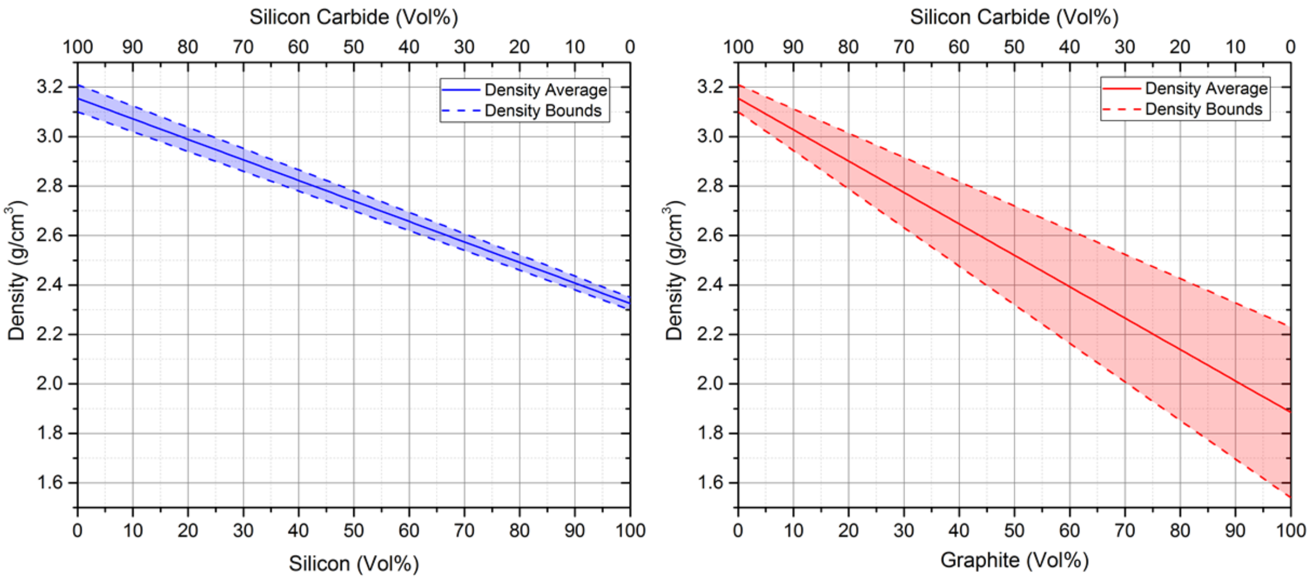

Figure 48: Relationship between phase fraction and density for silicon and graphite in SiC. Density ranges for pure SiC, silicon, and graphite were obtained from the CES Materials Selector software [10].

The results of the density measurements are presented in Figure 49. The color scheme categorizes the samples as SSiC, RBSiC, or GLSiC. The sintered Samples J and FS have similar densities at 3.15 and 3.13 g/cm^3, respectively. This is close to theoretical density, which agrees with the lack of porosity found in both samples' microstructures and indicates a sufficient sintering process. Samples D and FR have lower densities of 3.00 and 3.04 g/cm^3, which is expected due to the presence of free silicon in RBSiC. Once again, this agrees well with microstructure and the calculated free silicon volume fractions

(18% and 12% for D and FR, respectively), which fall within the bounded region on Figure 48. Finally, the GLSiC Samples A, S, FG, MSG, and MRBG have densities of 3.11, 2.93, 2.90, 3.02, and 2.76 g/cm^3, respectively. Immediately, Sample A draws attention by having a density comparable to the SSiC samples despite the expected presence of low-density graphite. This higher density supports the claim that this sample is improperly graphite-loaded SiC and confirms the results of microstructural analysis which show a lack of controlled graphite in Sample A. Samples S, FG, and MSG, however, do show a decrease in density in comparison to SSiC. Samples S and FG both have a total graphite fraction of 21 vol%, which accurately matches their densities to the average line in Figure 48. Sample MSG's graphite fraction of 15 vol% readily explains its relative increase in density compared to Samples S and FG while also matching the average line in Figure 48. The significantly lower density of Sample MRBG suggests copious quantities of secondary phases, which agrees with previous measurements. As such, density measurements support the earlier conclusions based on results of the ceramographic examination and XRD.

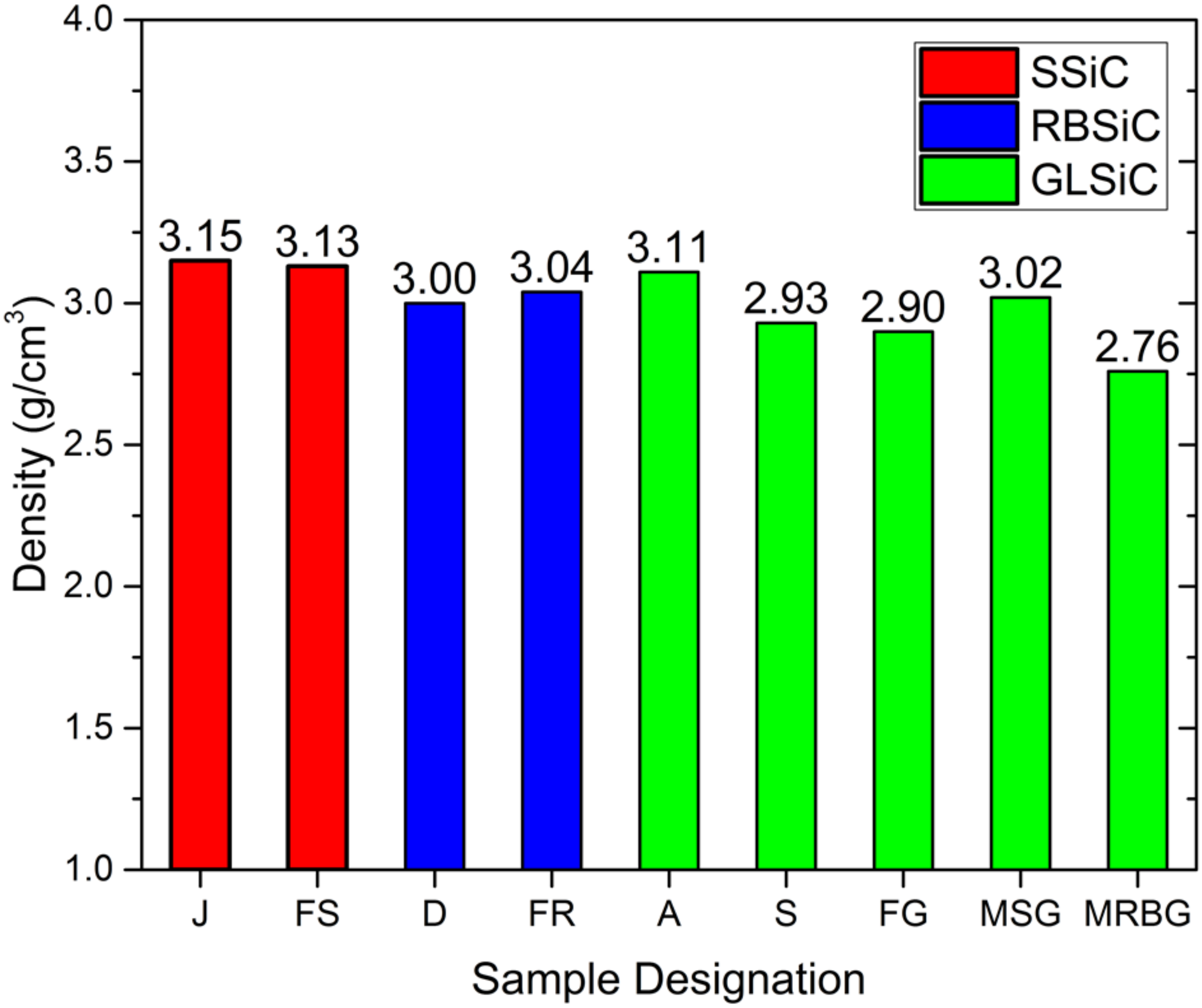

Figure 49: Densities of each of the sets of SiC mechanical seals measured by Archimedes' Method. The reported density of SiC is 3.15 g/cm^3; the density of samples with a significant fraction of a second phase is reduced because of the lower densities of silicon and graphite (2.32 g/cm^3 and 1.88 g/cm^3) [10].

5.2.2 Resonant Ultrasound Spectroscopy

Due to time constraints, RUS measurements could only be carried out on the first four samples received for the project (Samples A, S, D, and J). The results are shown in Figure 50. Young's modulus for Sample J (SSiC) is in agreement with literature values (390-410 GPa) as well as reported values from the supplier [10]. Sample D (RBSiC) had a much lower Young's modulus due to the presence of free silicon within the sample. Similarly, Sample S (GLSiC) also has a low Young's modulus due to the presence of graphite. Finally, Sample A (reportedly GLSiC) displays a Young's modulus similar to pure SiC, indicating that the presence of graphite within the matrix is minimal.

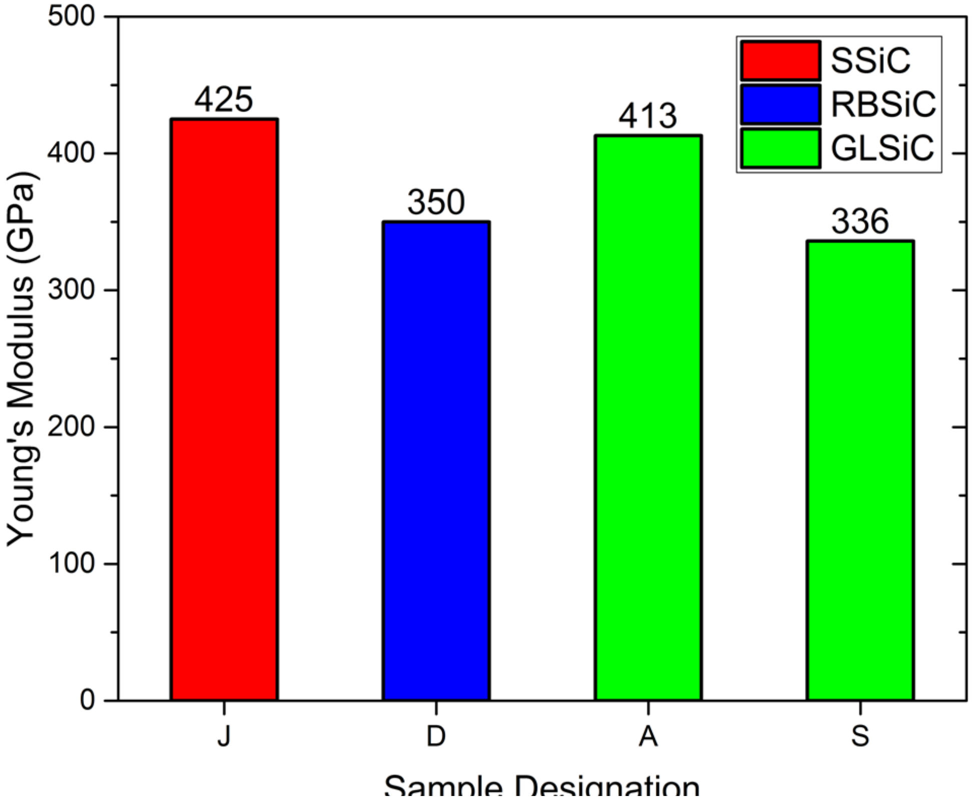

Figure 50: Young's Modulus for each of the first four sets of SiC mechanical seals calculated by analysis of RUS data. Moduli agree with reported values in literature (ESiC = 390-410 GPa); A lower modulus is observed in the RBSiC sample (ESilicon = 140-180 GPa) and Sample S (GLSiC) [10].

5.3 MECHANICAL PROPERTY EVALUATION

A knowledge of mechanical properties is crucial to understanding the quality of mechanical seals and its potential applications. Each SiC mechanical seal's performance will be influenced by its ability to resist both deformation and damage from abrasives. As such, microhardness testing provides information on the seals' wearing characteristics and their capability to withstand abrasive damage. Compression testing provides an idea of the ranges of forces in which the seals can operate effectively. Further, the response to deformation induced by microhardness and compression testing will shed light on the toughness and failure characteristics of the SiC mechanical seals. In the following sections, the results of microhardness (*Section 5.3.1*) and attempted compression testing (*Section 5.3.2*) are presented.

5.3.1 Microhardness

The hardness of mechanical seal face materials is a critical property that determines the in-service wear rate (component lifetime) and susceptibility to inhomogoneous seal face damage (wear track formation, damage by abrasive particles, etc.). For applications with harsh operating parameters or environments, the selection of hard seal face materials will improve component lifetime and thus system reliability. Soft face materials, however, reduce friction (minimizing heat at the interface that would otherwise disrupt the barrier fluid layer) when mated to hard face materials. It is therefore important to determine the hardness of SiC mechanical seals to assess their individual advantages in sealing applications. As detailed in the *Experimental* section, microhardness data were procured by measuring the diagonals of diamond-shaped indentations formed using a load of 1000 grams-force. Representative indentations are shown for sintered samples and reaction-bonded samples in Figure 51 and Figure 52, respectively. Indentations in the sintered samples were made on pure SiC with minimal contributions from native graphite; in reaction-bonded samples, indentations encompass both SiC and free silicon were performed. The Vickers microhardness measured for the provided samples is plotted in Figure 53, separated by manufacturing method (sintered versus reaction-bonded). The sintered samples provided for analysis exhibit consistent hardness values in the range of 2400-2700 HV; alternatively, the reaction-bonded samples were found to be softer, with hardness values on the order of 1600-2000 HV. This drop in hardness was expected due to the contributions of free silicon (with a hardness value of 1000 HV compared to SiC's reported hardness of 2500 HV) [10]. The effect of free silicon on hardness can be observed by comparing the reaction-bonded specimens in order of increasing free silicon volume percent: Sample FR (12% Si), Sample D (18% Si), and Sample MRBG (20% Si). These samples exhibit average hardness values of 2023 HV, 1742 HV, and 1591 HV, respectively. Thus, a negative correlation is observed between free silicon volume percent and hardness.

It should be noted, however, that the reaction-bonded samples experienced extensive chipping upon indentation (as evidenced by Figure 54). This chipping was more severe in regions containing higher fractions of free silicon. There are two potential reasons for this phenomenon. The first is that silicon exhibits a lower fracture toughness than SiC ($9x10^5$ Pa-$m^{0,5}$ compared to $2x10^6$ Pa-$m^{0.5}$). Another possible explanation of chipping is the residual stress that remains in the reaction-bonded matrix after fabrication. Upon cooling in the reaction-bonding process, thermal stresses are generated upon cooling due to coefficient of thermal expansion differences (CTE_{SiC} = 4.5x10^{-6} °C^{-1} and CTE_{Si} = 2.5x10^{-6} °C^{-1}) [10]. As a result of extensive chipping in silicon-rich regions, these regions yielded a larger fraction of immeasurable indentations; consequentially, the reported hardness is biased because more measurable indentations were present in regions with a locally high SiC fraction, as shown in Figure 54. This bias likely causes the reported hardness for reaction-bonded seals to be higher than their true values. However, the values in Figure 53 provide a reasonable estimation for seal performance. SSiC seals should be utilized in the harshest environments, such as for process fluids with abrasive particles or in intended boundary lubrication conditions. Reaction-bonded seals provide a low-cost alternative for use in milder applications; furthermore, reaction-bonded seals may be selected as a softer seal face material to be mated to harder SSiC seals.

While the observed chipping in reaction-bonded samples qualitatively suggests that they possess lower fracture toughness than sintered samples, a quantitative comparative method was attempted. As shown in Figures 51 and 52, cracks are produced at the microhardness indentations' vertices. The length of these cracks was expected to directly correlate to the sample's fracture toughness (longer cracks for lower fracture toughness specimens). A comparison of the average vertex crack length is displayed in Figure 55. Unlike the hardness measurements, the crack length values do not show conclusive trends. A few sintered samples (Samples J, A, and S) possess slightly lower crack length values, but the statistical variance within each sample's measurements was too considerable to draw meaningful conclusions. For this reason, crack lengths could not quantify the concerns of fracture toughness loss in reaction-bonded samples.

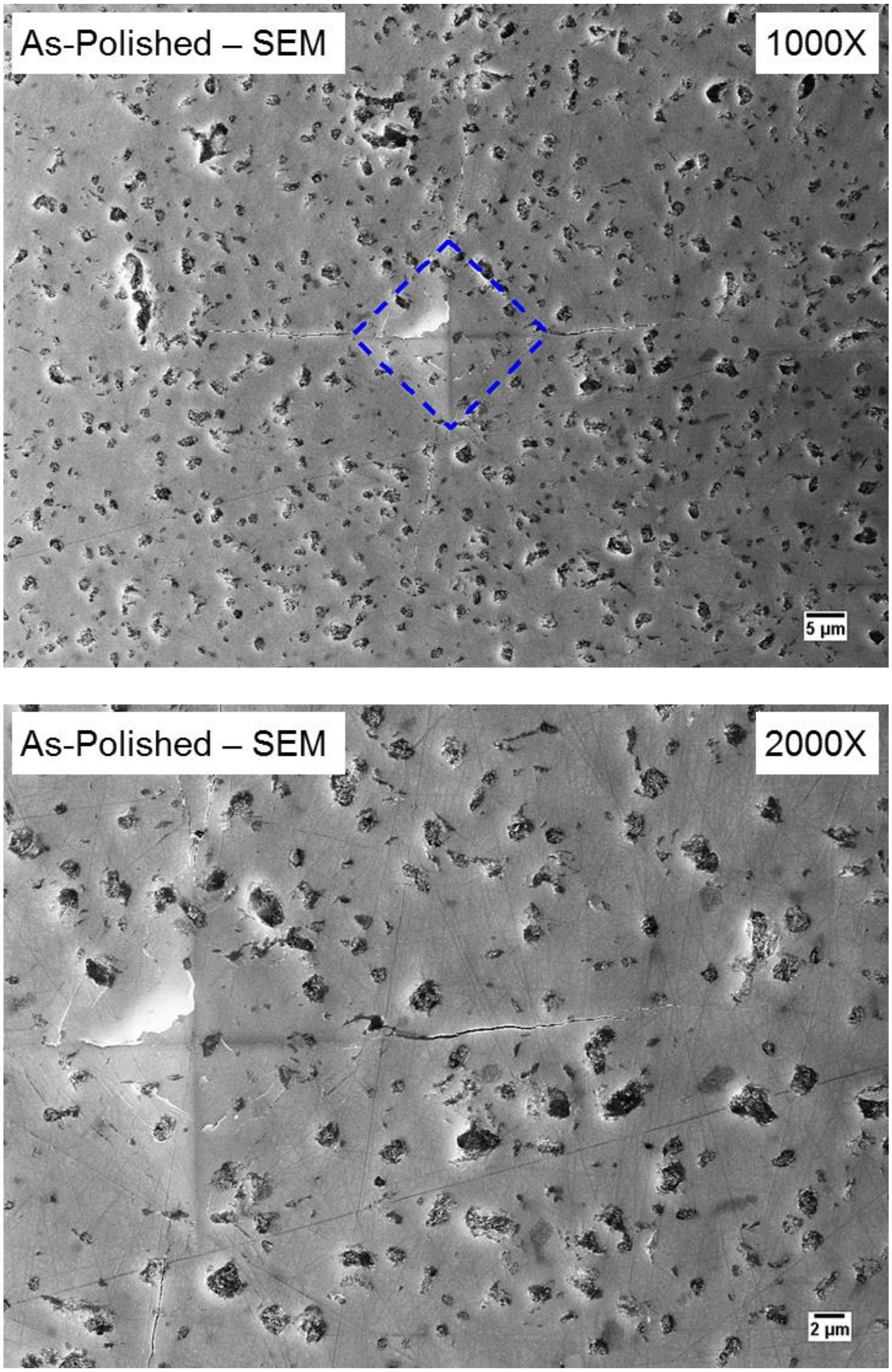

Figure 51: SEM micrographs at 1000X (top) and 2000X (bottom) of a representative 1000 gf Vicker's microhardness indentation in SSiC. The hardness indentation is outlined by the blue dashed line in the 1000X micrograph. Notice the native graphite nodules that are apparent in the 2000X micrograph.

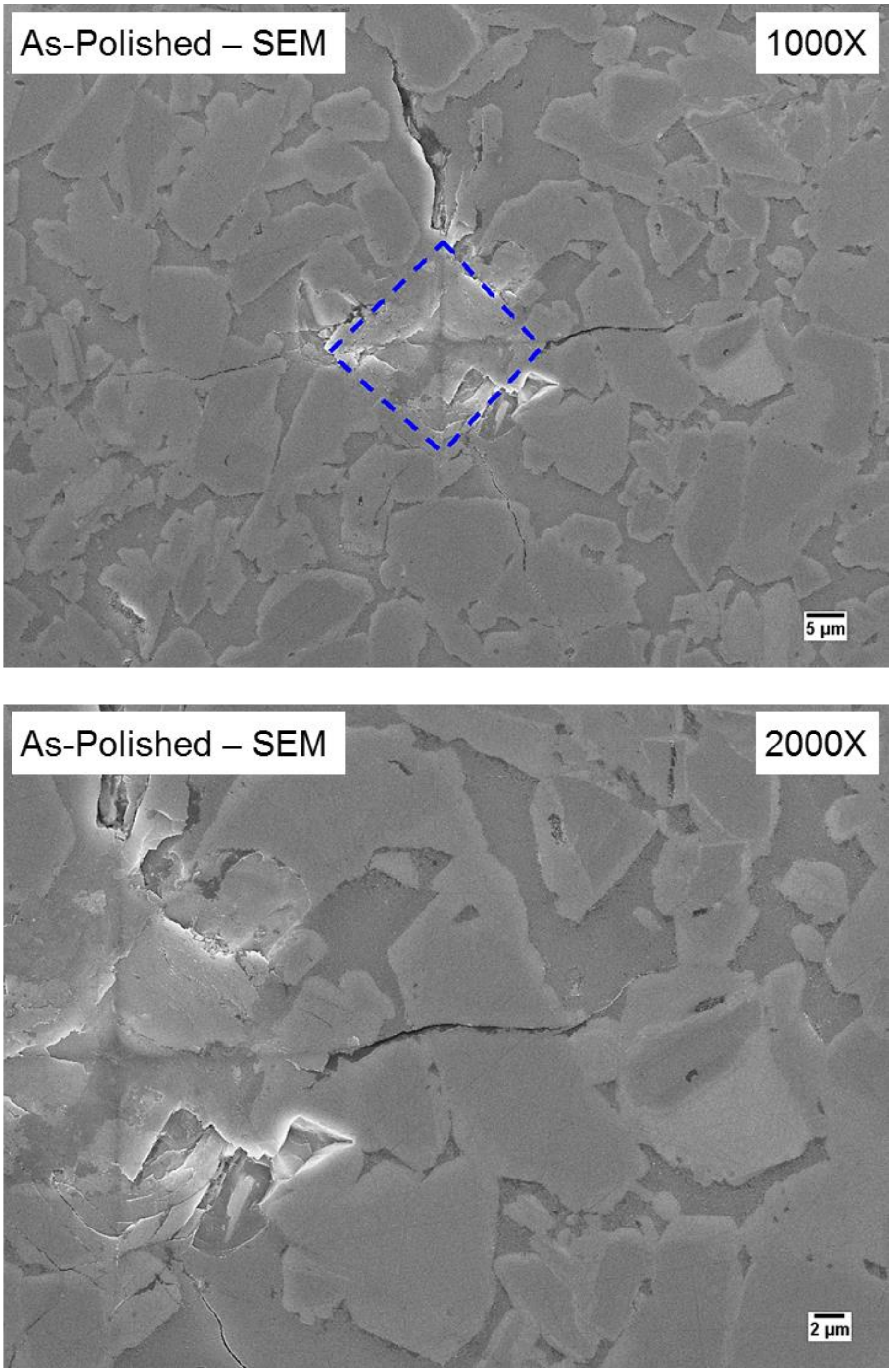

Figure 52: SEM micrographs at 1000X (top) and 2000X (bottom) of a representative 1000 gf Vicker's microhardness indentation in RBSiC. The hardness indentation is outlined by the blue dashed line in the 1000X micrograph. Cracks that propagated from the vertices of the indentations propagated indiscriminately through both free silicon and SiC.

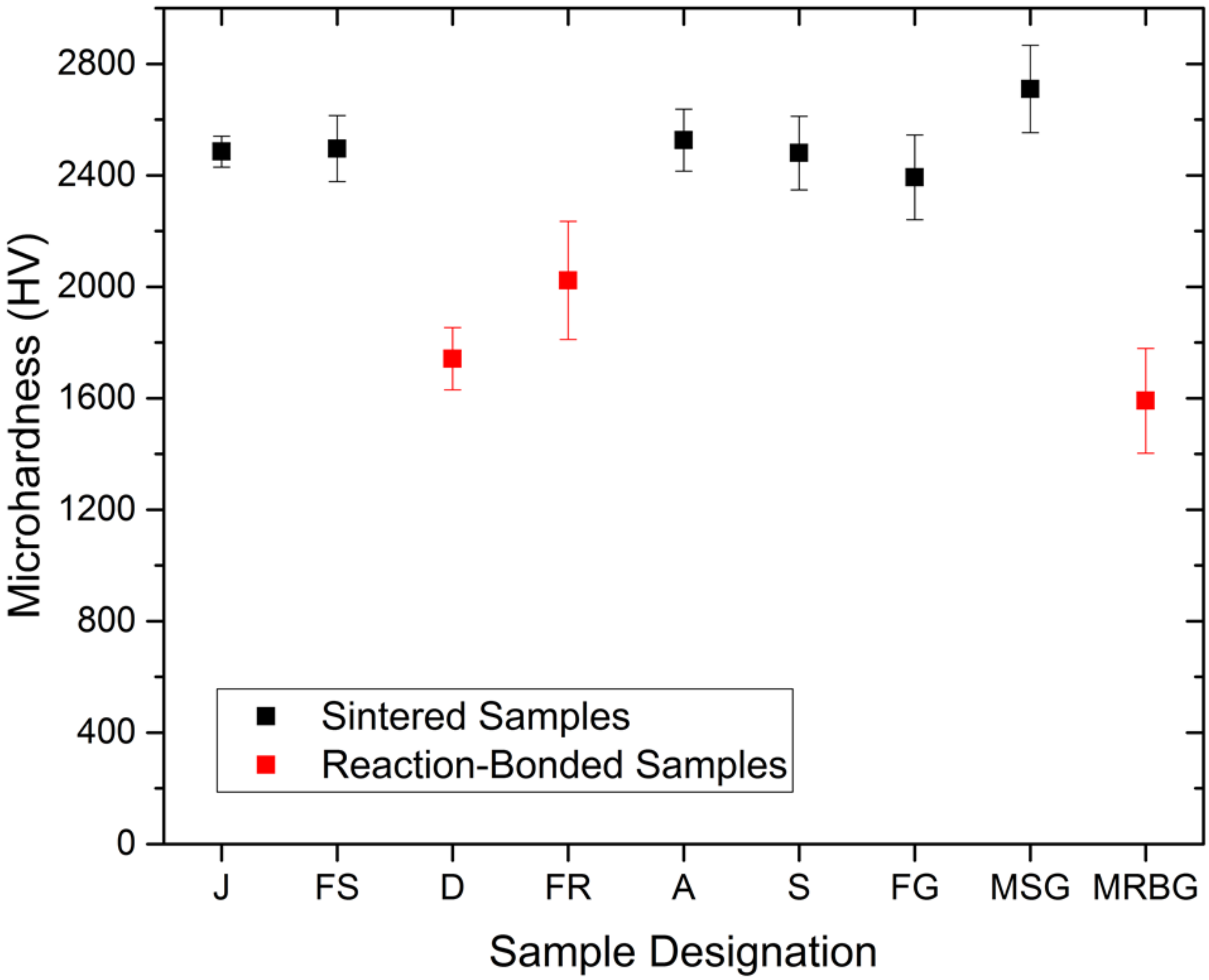

Figure 53: Vickers microhardness of each of the sets of SiC mechanical seals. The samples fabricated by sintering have hardness between 2450 and 2650 HV while the reaction-bonded samples display hardness between 1600 and 2000 HV. The hardness is inversely correlated with free silicon content.

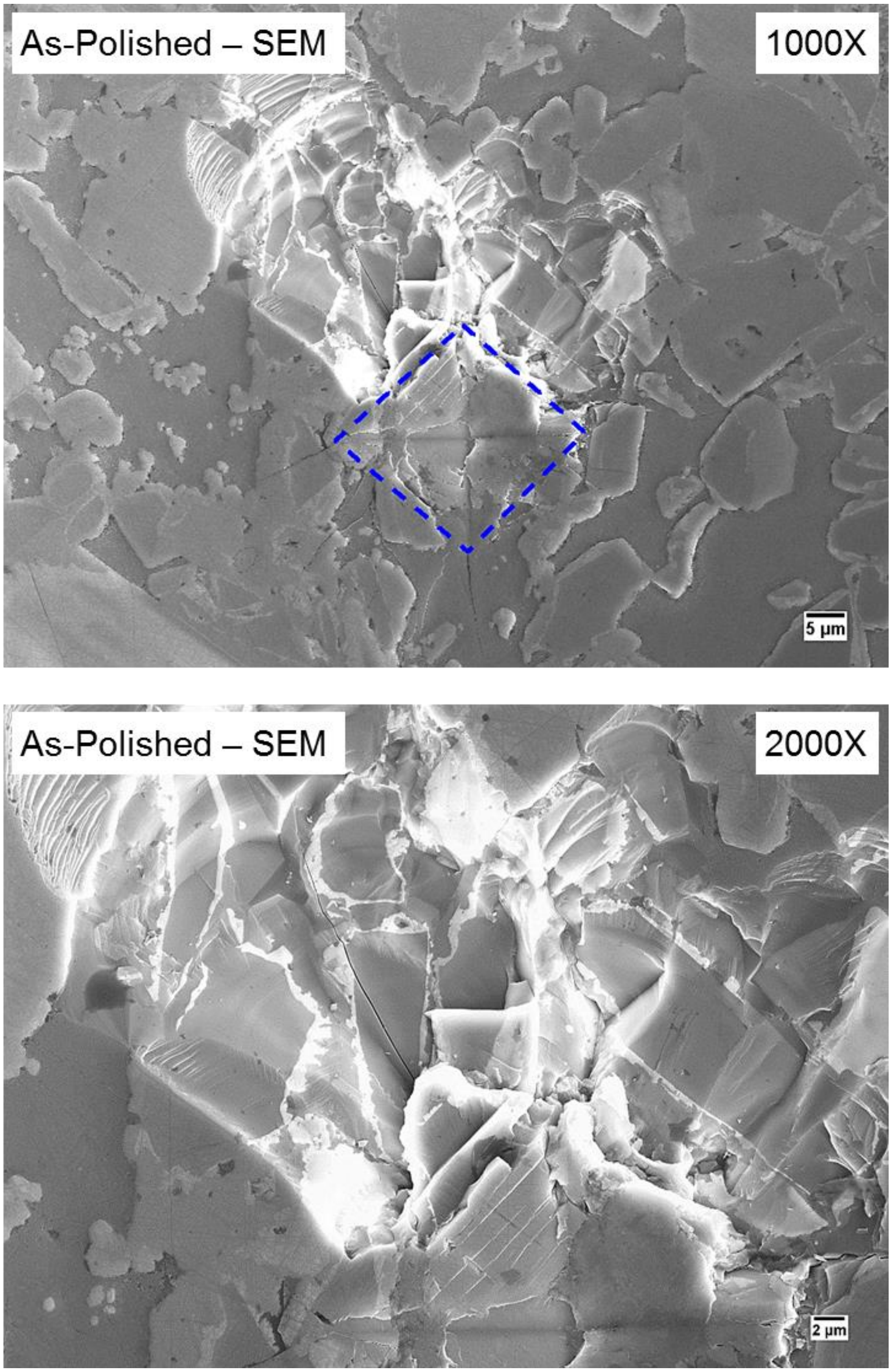

Figure 54: SEM micrographs at 1000X (top) and 2000X (bottom) of a representative 1000 gf Vicker’s microhardness indentation in reaction-bonded SiC. The hardness indentation is outlined by the blue dashed line in the 1000X micrograph. Rather than cracking, a majority of indentations in RBSiC chipped to accommodate the deformation induced by the hardness indentation, rendering the hardness indentation unmeasurable.

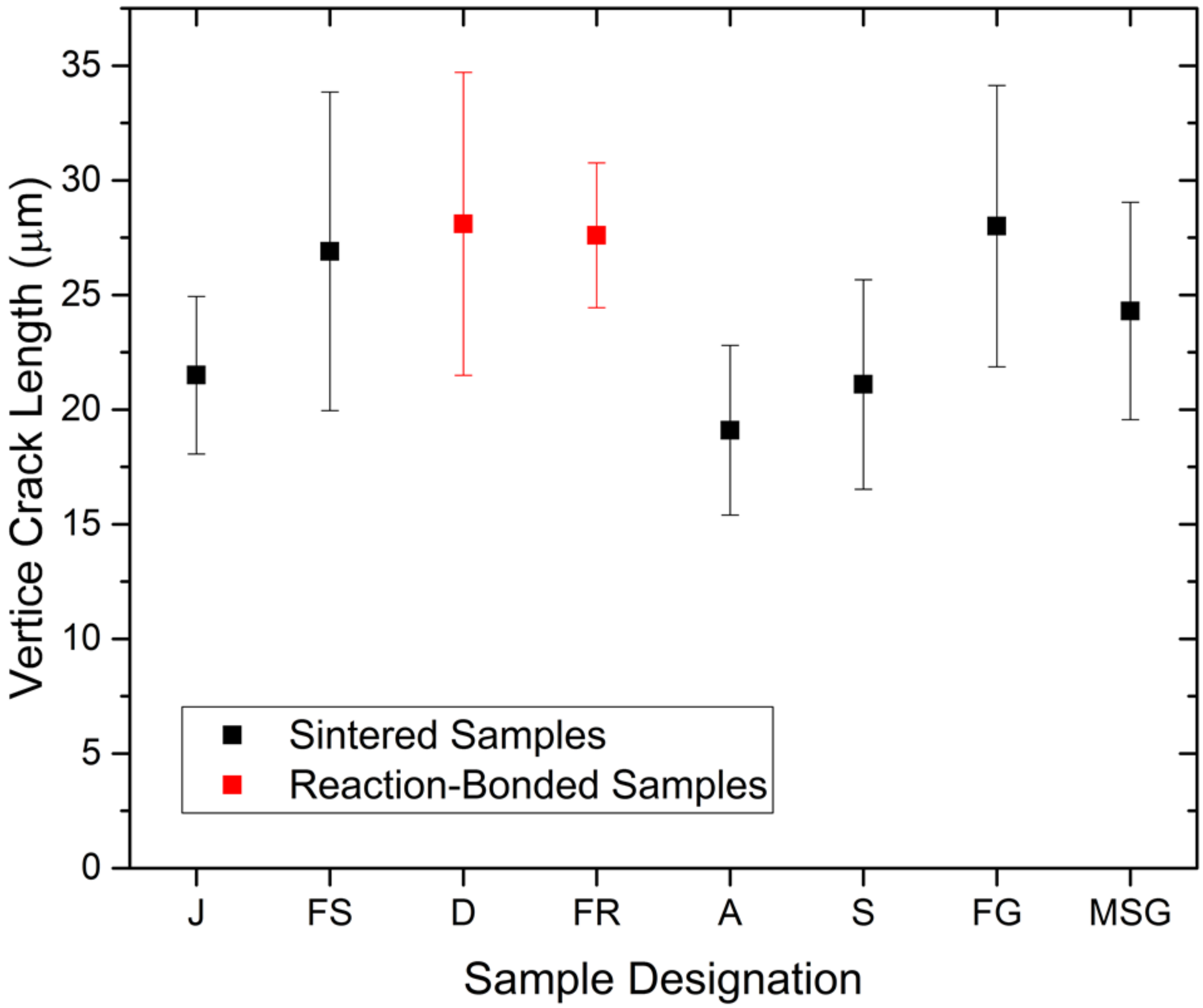

Figure 55: Average length of the crack at each vertex of the microhardness indentations. No discernable trend was observed between sample types. Data for Sample MRBG was not presented due to excessive chipping that occurred near hardness indentations.

5.3.2 Compression Testing

Due to the inherent difficulty of machining samples from a material as hard as silicon carbide, only a limited number of samples were obtained for compression testing. Several data sets were collected using these samples, however, not enough data was collected to be reasonably confident in the overall accuracy for each of the sample sets. As such, no quantitative results will be provided for compression testing.

The failure method of the tested samples was through brittle fracture. During testing, plastic deformation was not observed due to the absence of a deformation mechanism because of SiC’s strong covalent bonding. The only observable signs that failure was imminent was the presence of chipping as progressively more force was applied. Shortly after the onset of any major chipping, a major failure would occur where the sample would instantaneously release all stored energy as it exploded outwards. This brittle behavior inhibited the fabrication of samples as any large amount of force applied during machining would fracture the sample, rendering it unusable. Additionally, this behavior required more stringent conditions to be met for testing samples in general. The lack of ability to deform meant that sample ends must be perfectly flat and perpendicular to the longitudinal axis of the sample to ensure the collection of valid data.

6 SUMMARY

Mechanical seals are critical components in a wide range of industrial equipment such as pumps, agitators, and mixers. The design for a successful mechanical seal imposes strict thermal, mechanical, and chemical requirements on the selection of a high-performance and long-lasting seal face material. Silicon carbide (SiC) has garnered significant interest due to its superior hardness, thermal conductivity, relatively low cost, and good toughness. With the goal of providing superior customer service and product quality, AESSEAL Inc. has sponsored this senior design project in an effort to gauge and compare the characteristics of sintered SiC (SSiC), reaction-bonded SiC (RBSiC), and graphite-loaded SiC (GLSiC) for use as mechanical seal materials. To this aim, AESSEAL provided a total of nine sets of SiC mechanical seals, which included two sets of SSiC seals (Samples J and FS), two sets of RBSiC seals (Samples D and FR), and five sets of GLSiC seals (Samples A, S, FG, MSG, MRBG).

A three-step approach was employed for the analysis of these seals: phase identification (ceramography and x-ray diffraction (XRD)), phase quantification (ImageJ Automated Image Analysis Software), and property determination (density, elastic moduli through resonant ultrasound spectroscopy (RUS), microhardness, and compression testing). A summary of the results of this investigation are presented in the following list and are divided based upon SiC type:

1. <u>Sintered SiC:</u> SSiC mechanical seals are formed by pressureless sintering at temperatures between 2100 and 2300 ^{o}C and have superior mechanical properties (hardness, strength, and toughness), physical properties (elastic

modulus, thermal expansivity, thermal conductivity), and chemical properties (corrosion resistance) in comparison to SiC formed by reaction-bonding. The SSiC sets of mechanical seals (Samples J and FS) were observed to have the highest densities (3.15 and 3.13 g/cm^3, respectively). Native graphite, defined as graphite nodules introduced during SiC powder manufacturing or sintering having a diameter on the order of 1 μm in diameter, were observed in both samples at a volume fraction of 6%. XRD confirmed the presence of graphite in a matrix of α-SiC. The hardnesses were determined to be approximately 2500 HV (2485 HV for Sample J and 2496 HV for Sample FS). Through RUS, Young's modulus was found to be 425 GPa, which is comparable to the reported range of 390 GPa to 410 GPa [10].

2. Reaction-Bonded SiC: RBSiC mechanical seals are formed by the infiltration of a compact of SiC particles by liquid silicon at temperatures greater than the melting point of silicon (1410 ^{o}C). Free silicon remains after the completion of the reaction bonding process; optimum properties are obtained when free silicon volume fractions are between 5 and 12%. RBSiC mechanical seals are a less costly alternative to SSiC and can be employed as a mating face to a harder SSiC seal when selective wear is desired in the sealing system design. The RBSiC samples, Samples D and FR, were observed to have densities of 3.00 g/cm^3 and 3.04 g/cm^3. From XRD, the constituents present were determined to be α-SiC and silicon. Ceramographic examination revealed that Sample D had 18 vol% free silicon and that Sample FR had 12 vol%. Hardnesses were determined to be 1742 HV and 2023 HV for Samples D and FR, respectively. Young's modulus was

determined to be 350 GPa, which is significantly lower than the reported value for pure SiC due to the presence of a lower modulus phase (silicon).

3. Graphite-Loaded SiC: GLSiC mechanical seals have large graphite agglomerates that are introduced during the manufacturing process, which result in graphite nodules on the order of 100 μm in diameter. These nodules, referred to as controlled nodules, are pulled out during lapping and result in the improvement of tribological properties. GLSiC is primarily manufactured by sintering but may also be fabricated by reaction-bonding. GLSiC may consist of up to 20 vol% controlled graphite; therefore, the physical and mechanical properties are influenced significantly. Of the five GLSiC samples, four of them (Sample A, S, FG, and MSG) were manufactured by sintering. Sample A was determined to be improperly graphite-loaded SiC due to its high density (3.11 g/cm^3), high modulus (413 GPa), and absence of a significant volume fraction of nodules on the order of 100 μm (0.06 vol%). Samples S and FG were found to have densities of 2.93 and 2.90 g/cm^3 and 9 and 12 vol% of controlled graphite with an average diameter of 57 and 58 μm, respectively. Therefore, Samples S and FG were highly similar. Sample S was determined to have a Young's of 336 GPa by RUS. Sample MSG was determined to have a density of 3.02 g/cm^3 and 6 vol% of controlled graphite that has an average size of 24 μm. In comparison to Samples S and FG, Sample MSG has more nodules in the range of 20 to 100 μm and fewer nodules from 100 to 200 μm. Sample MSG was claimed to have superior performance in comparison to other SiC mechanical seals by Morgan Advanced Materials. This claim may be justified since AESSEAL's lapping procedure was determined to pull

out a more significant fraction of controlled nodules having diameters between 20 and 80 μm. Native graphite nodules were present in all sintered GLSiC samples. Sample MRBG is a reaction-bonded GLSiC specimen having the lowest density of any of the seal sets at (2.76 g/cm^3), having 16 vol% controlled graphite and 20 vol% free silicon. It is hypothesized that the mechanical, physical, and chemical properties of MRBG are limited by large volume fractions of detrimental constituents.

Extensive evaluation of microstructural, physical, and mechanical properties has been conducted on nine sets of SiC mechanical seals. Significant conclusions regarding the characteristics of each of these sets of SiC seals have been presented. Beyond these specific sets of mechanical seals, background information and interpretation have been provided that will aid in the future for making materials design, selection, and quality control decisions. With this knowledge, AESSEAL Inc.'s engineers should be able to ask suppliers simple questions such as "What is the density of seals in a batch of SiC mechanical seals?", "How much free silicon does this batch of seals contain?", or "What is the distribution of controlled graphite nodules in this set of GLSiC seals?". Further investigation into the tribological role of controlled graphite nodules in GLSiC seals and the determination of the most favorable lapping procedure for the pulling-out of graphite nodules to provide optimum tribological properties should be performed.

7 REFERENCES

[1] “Component Seals and Machine Specific Plug In Seals,” *Component Seals and Machine Specific Plug In Seals*. AESSEAL, Rotherham, UK, 2017.

[2] “Pump and Pump System Glossary,” *PUMPfundamentals*. [Online]. Available: http://www.pumpfundamentals.com/pump_glossary.htm. [Accessed: 26-Jan-2017.

[3] C. Rehmann, “Reduce the Red by Going Green,” *Uptime Magazine*, 2009.

[4] I. Peel, “Pumps: Mechanical Seal or Magnetic Drive?,” *Industrial Lubrication and Tribology*, vol. 48, no. 4, pp. 6–7, 1996.

[5] I. J. Karassik and T. McGuire, “Pump Types and Construction - Stuffing Boxes,” in *Centrifugal Pumps*, 2nd ed., London, England: Chapman & Hall, 1998, pp. 136–160.

[6] I. J. Karassik and T. McGuire, “Pump Types and Construction - Mechanical Seals,” in *Centrifugal Pumps*, 2nd ed., London, England: Chapman & Hall, 1998, pp. 161-194.

[7] I. J. Karassik, J. P. Messina, P. Cooper, and C. C. Heald, “Centrifugal Pump Mechanical Seals,” in *Pump Handbook*, 3rd ed., New York, NY: McGraw-Hill, 2001, pp. 197–239.

[8] “Back to Basics: Mechanical Seals Explained,” *Sailor's Diaries*, 30-Jun-2013. [Online]. Available: http://sailorsdiaries.blogspot.com/2013/06/back-to-basics-mechanical-seals.html. [Accessed: 27-Jan-2017].

[9] Huebner M., "Material Selection in Mechanical Seals", *Proceedings of the Twenty-Second International Pump Symposium*, 2005, p. 127 – 135.

[10] Granta Material Intelligence, “CES 2017 Materials Selector.” Licensed Through: *The University of Tennessee – Knoxville*.

[11] K. Yamada, M. Mohri. “Properties and Applications of Silicon Carbide Ceramics,” in *Silicon Carbide Ceramics - 1: Fundamentals and Solid Reaction.* New York, NY: Elsevier Science Publishers, 1991, pp. 13-44.

[12] Y. W. Kim, M. Mitomo, H. Emoto, and J. G. Lee, “Effect of Initial α-Phase Content on Microstructure and Mechanical Properties of Sintered Silicon Carbide,” *Journal of the American Ceramic Society*, vol. 81, no. 12, pp. 3136–3140, 1998.

[13] J. N. Ness and T. F. Page, “Microstructural Evolution in Reaction-Bonded Silicon Carbide,” *Journal of Materials Science*, vol. 21, no. 4, pp. 1377–1397, 1986.

[14] Fluid Sealing Association. *Sealing Sense*. Jan. 2006, pp. 64-66.

[15] P. J. Guichelaar, “Acheson Process,” in *Carbide, Nitride and Boride Materials Synthesis and Processing*, London: Chapman & Hall, 1997, pp. 115–129.

[16] H. N. Baumann, “The Relationship of Alpha and Beta Silicon Carbide,” *Journal of The Electrochemical Society*, vol. 99, no. 3, p. 109, 1952.

[17] N. H. Rahaman, “Synthesis of Powders,” in *Ceramic Processing and Sintering*, 2nd ed., New York, NY: Marcel Dekker, pp. 70–93.

[18] Y. M. Chiang, R. P. Messner, C. D. Terwilliger, and D. R. Behrendt, “Reaction-Formed Silicon Carbide,” *Materials Science and Engineering*, vol. 144, no. 1-2, pp. 63–74, 1991.

[19] L. G. Talbert and S. M. Brazil, “Graphite-Loaded Silicon Carbide,” 23-Jan-1996.

[20] E. G. Wilkins, “Graphite Loaded Silicon Carbide and Methods for Making,” 10-Aug-2004.

[21] H. Lubbinge, University of Twente, “Review on the Lubrication of Mechanical Face Seals”, in *On the Lubrication of Mechanical Face Seals*, Enschede, pp. 7-20, 1999.

[22] Y. Kondo, T. Koyama, S. Sasaki, “Tribological Properties of Ionic Liquids”, *Ionic Liquids - New Aspects for the Future*, Chapter 5, InTech, 2013.

[23] P. Blau, Oak Ridge National Laboratory, Materials Science and Technology Division, “Use of Textured Surfaces to Mitigate Sliding Friction and Wear of Lubricated and Non-Lubricated Contacts: An annotated literature review,” UT-Batelle for the Department of Energy, 2012.

[24] W. R. D. Wilson, Northwestern University “A Theoretical Model of Micro-Pool Lubrication in Metal Forming”, *Journal of Tribology*, Vol. 121, pp. 731 - 737, 1999.

[25] U. Pettersson, S. Jacobson, Uppsala University, “Friction and wear properties of micro textured DLC coated surfaces in boundary lubricated sliding”, *Tribology Letters*, Vol. 17, No. 3, 2004.

[26] M. Razzaque, T. R. Faisal, Bangladesh University of Engineering and Technology, “Performance of Mechanical Face Seals with Surface Micropores”, *Journal of Mechanical Engineering*, Vol. ME37, pp. 77-81, 2007.

[27] S. M. Hsu, Y. Jing, D. Hua, H. Zhang, George Washington University, “Friction reduction using discrete surface textures: principle and design,” *Journal of Physics D: Applied Physics*, Vol. 47, pp 1-7, 2014.

[28] X. Wang, K. Kato, K. Adachi, K. Aizawa, “The effect of laser texturing of SiC surface on the critical load for the transition of water lubrication mode from hydrodynamic to mixed”, *Tribology International*, Vol. 34, pp. 703-711, 2001.

[29] “Morgan Advanced Materials Offers PGS-100 Graphite-Loaded Silicon Carbon for Demanding Oil and Gas Sealing Applications,” *Morgan Advanced Materials*, 16-Jun-2015. [Online]. Available: http://www.morganadvancedmaterials.com/en-gb/media-centre/press-releases-morgan-issued/morgan-advanced-materials-offers-pgs-100-graphite-loaded-silicon-carbon-for-demanding-oil-and-gas-sealing-applications/. [Accessed: 24-Feb-2017].

[30] “Graphite Loaded Sintered SiC,” *MicroGrain General Seals Co., Ltd*. [Online]. Available: http://www.mggsseal.com/about3/i=8&comContentId=8.html. [Accessed: 24-Feb-2017].

[31] M. Huebner, Texas A&M University, “Material Selection for Mechanical Seals,” *Proceedings of the Twenty-Second International Pump Users Symposium*, pp. 127 - 132, 2005.

[32] “How Can Capabilities of Primary Seal Materials Be Improved?,” *Pump & Systems*. [Online]. Available: http://www.pumpsandsystems.com/topics/seals/how-can-capabilities-primary-seal-materials-be-improved. [Accessed: 24-Feb-2017].

[33] B.H. Toby, R.B. Von Dreele. "GSAS-II: The Genesis of a Modern Open-Source All Purpose Crystallography Software Package" *Journal of Applied Crystallography,* 46, 2013, p 544-549.

[34] Schindelin, J.; Rueden, C. T. and Hiner, M. C. et al. (2015), "The ImageJ Ecosystem: An Open Platform for Biomedical Image Analysis", *Molecular Reproduction and Development*, PMID 26153368 (on Google Scholar).

[35] W.H. Bragg. “The Structure of Some Crystals as Indicated by Their Diffraction of X-rays.” *Nature*, 91, 1913, p 248-277.
[36] B.H. Toby, R.B. Von Dreele. "GSAS-II: The Genesis of a Modern Open-Source All Purpose Crystallography Software Package" *Journal of Applied Crystallography,* 46, 2013, p 544-549.
[37] R.G. Leisure, F.A. Willis. “Resonant Ultrasound Spectroscopy.” *Journal of Physics: Condensed Matter*, 9, 1997, p 6001-6029.
[38] ASTM Standard C1327-15, 2015, "Standard Test Method for Vickers Indentation Hardness of Advanced Ceramics," ASTM International, West Conshohocken, PA, www.astm.org.
[39] J. Lankford, “Characterization of Compressive Damage Mechanisms in Ceramic and Polymeric Matrix Composite Materials ,” *Office of Naval Research Report*, Feb. 1995.
[40] G. C. Capitani, S. Di Pierro, G. Tempesta.” The 6H-(SiC) Structure Model: Further Refinement from SCXRD Data from a Terrestrial Moissanite,” *American Mineralogist.* 92, 2007, pp. 403-407.
[41] J. Y. Howe, C. J. Rawn, L. E. Jones, H. O. “Improved Crystallographic Data for Graphite,” *Powder Diffraction*. 18 (2), 2003, pp. 150-154.
[42] R. Hubbard, H. E. Swanson, F. A. Mauer. “A Silicon Powder diffraction Standard Reference Material,” *Journal of Applied Crystallography,* 8, 1975, pp. 45-48.
[43] Morgan Advanced Materials, “PGS 100 Graphite-Loaded SiC Seals”, Facebook, 13 June 2016, Accessed: 23 March 2017, URL: https://www.facebook.com/search/top/?q=Morgan%20Advanced%20Materials%20pgs%20100.

8 APPENDIX A – SAMPLE INVENTORY

Samples A1-A5: Five duplicate seals with a highly polished seal face (1X).

Seal Face Angled View Back Side

Sample D1: Single tall SiC seal with O-ring (1X).

Seal Face Angled View

Sample D2: Single parallel spring SiC seal with rubber body (1X).

Seal Face Angled View

Sample D3: Single parallel spring SiC seal with rubber body (1X).

Seal Face

Angled View

Sample D4: Single parallel spring SiC seal with rubber body (1X).

Seal Face

Angled View

Side View

Back Side

Sample D5: Single SiC seal with O-ring and locking grooves (1X).

Seal Face

Angled View

Sample D6: Single, large parallel spring SiC seal with rubber body (1X).

Seal Face

Angled View

Side View

Samples J1-J2: Two duplicate seals with rubber O-ring (1X).

S1 Seal Face

S1 Angled View

S1-S2 Assembly

Sample S1: Single, parallel spring, shrunk fit seal (1X). Mating seal: Sample S2

S2 Seal Face

S2 Angled View

S2 Side View

Sample S2: Single seal with O-ring (1X). Mating seal: Sample S1

S3 Seal Face

S3 Angled View

S3-S4 Assembly

Sample S3: Single, parallel spring, shrunk fit seal (1X). Mating seal: Sample S4

S4 Seal Face

S4 Angled View

S4 Side View

Sample S4: Single seal with O-ring (1X). Mating seal: Sample S3

FS Seal Face

FS Angled View

Sample FS: Single large seal with highly polished face (1X).

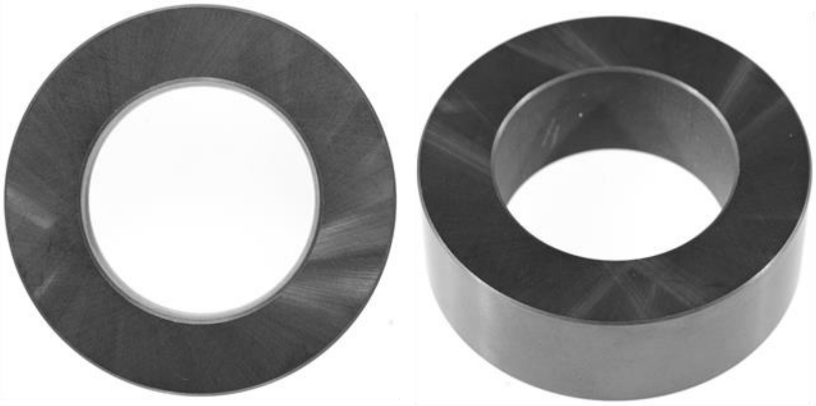

FR Seal Face FR Angled View

Sample FR: Single large seal with ground face having residual, radial grinding scratches (2X).

FG Seal Face FG Angled View

Sample FG: Single seal having a highly polished face (2X).

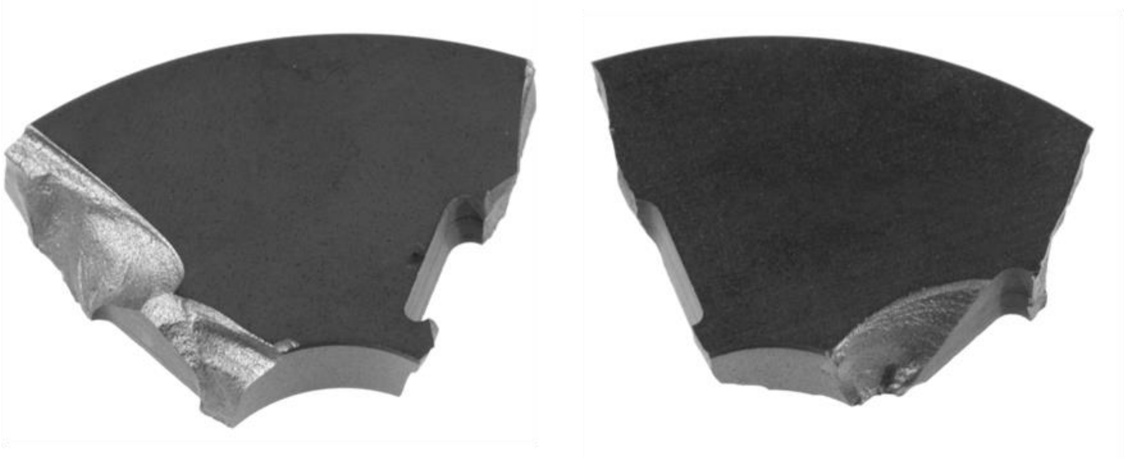

Sample MSG: Two pieces from a broken, unfinished seal from Morgan Advanced Materials (2X).

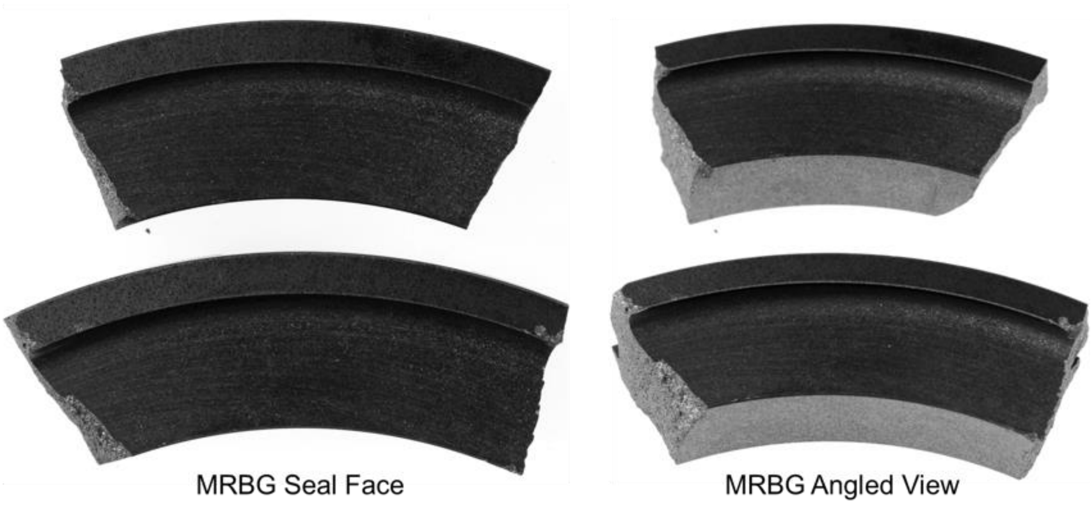

MRBG Seal Face

MRBG Angled View

Sample MRBG: Two pieces from a broken, unfinished seal from Morgan Advanced Materials (1X).

9 APPENDIX B – EVALUATION OF SILICON CARBIDE POWDER

Microstructural examination revealed the presence of graphite in all samples fabricated by sintering, termed *native graphite*. Native graphite is defined as graphite nodules introduced during SiC powder manufacturing or sintering; approximately 1 µm in diameter. To further elucidate the source of free carbon that resulted in the presence of graphite nodules, SiC powder was received from Penn United Technologies Ltd. Although Penn United Technologies was not a supplier of mechanical seals utilized in this investigation, they are a leading manufacturer of SiC components. Therefore, the provided powder will yield a representative example of SiC powder employed in sintered SiC component fabrication. The SiC powder was analyzed using scanning electron microscopy (SEM) and x-ray diffraction (XRD).

Microstructural information was revealed through SEM. The SiC powder consisted of spherical agglomerates ranging in size from 5 to 30 µm in diameter, as shown in Figure B1. The higher magnification SEM micrographs presented in Figure B2 reveal the substructure of the spherical agglomerates. The spherical agglomerates consist of two primary constituents: irregularly-shaped SiC particles and a carbon-rich binder. Suggested identities of the constituents present are proposed based on Z-contrast and the observed morphological features in the provided SEM micrographs. The micron- and submicron-sized irregularly-shaped, jagged SiC particles are formed by the crushing of bulk SiC manufactured by the Acheson Process. To aid green compact fabrication and sintering, the SiC particles were bound with a carbon-based polymeric binder. Therefore, the carbon-rich polymeric binder acts as a sintering aid and as the carbon source that leads native graphite nodules formation.

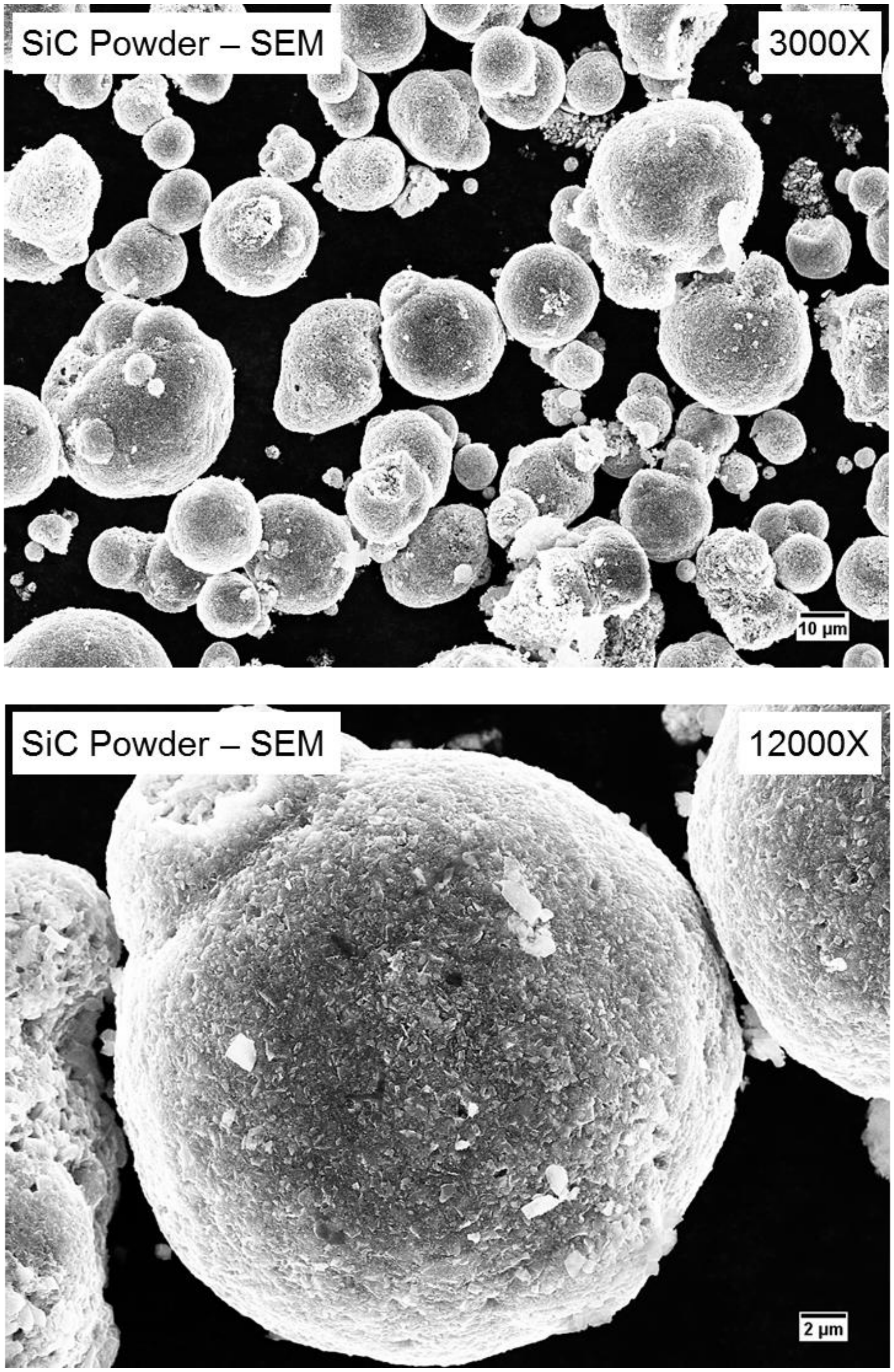

Figure B1: SEM micrographs at 600X (top) and 1200X (bottom) illustrating the SiC powder received from Penn United Technologies. The powder consisted of spherical agglomerates ranging in diameter from 5 to 30 µm.

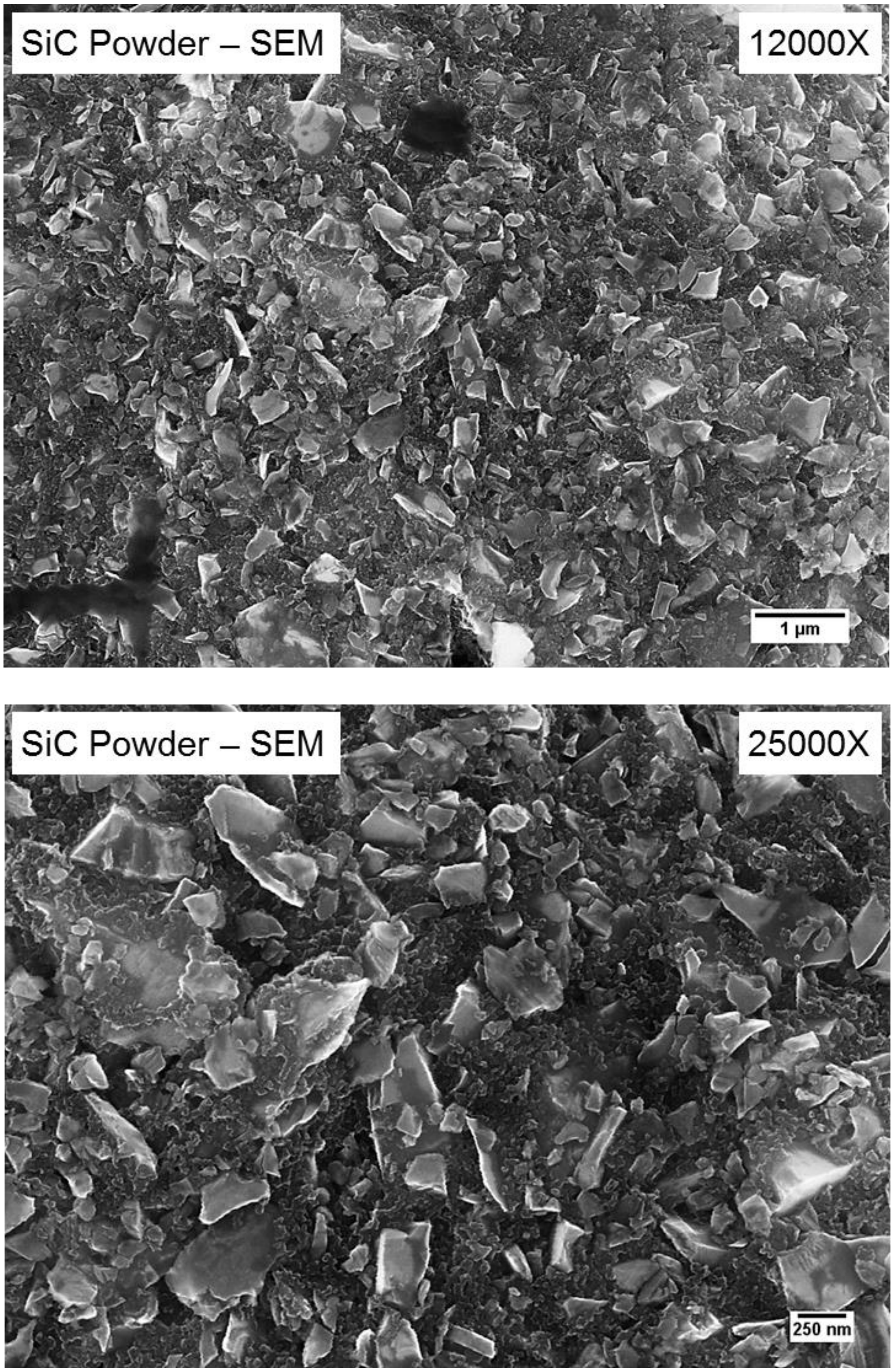

Figure B2: SEM micrographs at 12000X (top) and 25000X (bottom) displaying the fine scale morphology of the SiC powder received from Penn United Technologies. The spherical agglomerates consisted of micron- and submicron-sized irregularly-shaped, jagged SiC particles bound in a carbon-rich matrix.

To determine the presence of other constituents as well as the crystallographic characteristics of the SiC powder from Penn United Technologies Ltd, XRD data was collected and a calculated XRD profile was fitted to the XRD data, as shown in Figure B3. The XRD data and fitted pattern for the SiC powder suggest that α-SiC is the only crystalline phase present in a significant volume fraction. This implies that the polymeric binder does not contain a significant amount of crystalline graphite. Further, the width of the fitted peaks suggests a high degree of strain and/or crystallize size broadening because the peaks in the XRD pattern have a considerably greater width in comparison to previously presented XRD patterns for the SiC mechanical seals. This is a reasonable conclusion considering the SiC powder is formed by crushing at room temperature and the crystallite size ranges between a micron and tens of nanometers; both of these characteristics induce peak broadening.

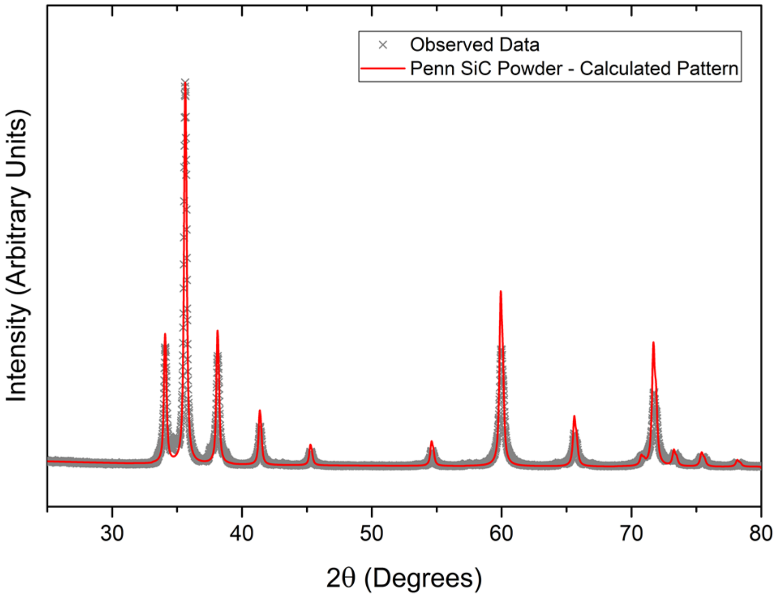

Figure B3: XRD data and fitted pattern for the SiC powder from Penn Technologies. The fitted pattern matched well with α-SiC (6H polytype). A combination of crystallite size broadening and strain broadening resulted in broad peaks. Carbon peaks were not observed suggesting that the carbon-rich binder was